



MCG 2018
Machine Control & Guidance



**6th International Conference on
Machine Control and Guidance**
1 - 2 Oct. 2018, Berlin



6th International Conference on Machine Control and Guidance


**1 – 2 October 2018
Berlin**

Bornimer Agrartechnische Berichte
Heft 101

Potsdam / Berlin 2018

Publisher:

Leibniz-Institut für Agrartechnik und Bioökonomie e.V.
Leibniz Institute for Agricultural Engineering and Bioeconomy (ATB)
Max-Eyth-Allee 100
14469 Potsdam-Bornim
Germany

 +49 (0) 331-5699-0
Fax.: +49 (0) 331-5699-849
E-mail: atb@atb-potsdam.de
Internet: <http://www.atb-potsdam.de>

September 2018

Editors:

Cornelia Weltzien
Jan Krüger
Henning Meyer

Cover Design:

Helene Foltan

Artwork:

Vanessa Karré

Layout:

Franziska Gleiniger

Published by the Leibniz Institute for Agricultural Engineering and Bioeconomy (ATB) with the support of the Federal Ministry of Food and Agriculture (BMEL) as well as of the Ministry of Science, Research and Culture of the State Brandenburg (MWFK).

Contents do not necessarily reflect the publisher's or editor's views in this area.

No part of the material may be reproduced or utilized in any form or by any means without permission from the publisher Leibniz Institute for Agricultural Engineering and Bioeconomy e.V.

ISSN 0947-7314

© Leibniz-Institut für Agrartechnik und Bioökonomie e.V., 2018

Table of Content

Acknowledgement.....	3
Automation and Assistance Systems	
Some challenges to address in order to target the second generation of agricultural robots <i>Michel Berducat</i>	5
Development of a learning tractor implements coupling application <i>Tobias Blume, Ilja Stasewitsch, Jan Schattenberg, Ludger Frerichs</i>	12
Automatic machine and implement identification of an agricultural process using machine learning to optimize farm management information systems <i>Thoralf Stein, Henning J. Meyer</i>	19
Autonomous phenotyping using a mobile manipulator <i>Camille Dubos, Roland Lenain, Michel Berducat, Frédéric Cointault</i>	27
Absolute and Relative Positioning	
Kinematic Positioning in a Real Time Robotic Total Station Network System <i>Gabriel Kerekes, Volker Schwieger</i>	35
In-field position accuracy at the millimetre level using a total station: Validation using an industrial robotic arm <i>Dimitris S. Paraforos, Marcus Reutemann, Galibjon Sharipov, Roland Werner, Hans W. Griepentrog</i>	44
Representation Learning for Segment Matching for Future Applications in Relative Positioning of Machinery <i>Julian Schmiemann, Jan Schattenberg, Ludger Frerichs</i>	52
Cooperative localization based on range-only measurements from robots and infrastructure <i>Cyrille Pierre, Roland Chapuis, Romuald Aufrère, Jean Laneurit, Christophe Debain</i>	62
Control and Guidance	
Comparison of controls for a stereo camera based reversing assistance system for vehicle trailer combinations <i>Ilja Stasewitsch, Tobias Blume, Jan Schattenberg, Ludger Frerichs</i>	74
Adaptive Control for Guidance of Tracked Vehicles <i>Otto Lerke, Volker Schwieger</i>	83
Towards motor control adjustment with inertial sensor measurements for small differential drive robots <i>David Reiser, Marvin Hubl, Hans W. Griepentrog</i>	95

Sensors in Plant Production

Concept and first results of a field-robot-based on-the-go assessment of soil nutrients with ion-sensitive field effect transistors <i>Vadim Tsukor, Stefan Hinck, Walter Niefeld, Frank Lorenz, Elena Nadjenko, Andreas Möller, Daniel Mentrup, Tino Mosler, Arno Ruckelshausen</i>	102
Leaf area estimation of reconstructed maize plants using a time-of-flight camera <i>Manuel Vázquez-Arellano, David Reiser, Dimitris S. Paraforos, Miguel Garrido-Izard, Hans W. Griepentrog</i>	110
Soil type recognition with artificial intelligence during compaction process <i>Ulrike Nohlen, Robin Popelka, Yann Berquin</i>	120
UAV-based Growth Rate Determination in Winter Wheat <i>Diana Becirevic, Lasse Klingbeil, Andreas Honecker, Henrik Schumann, Jens Léon, Heiner Kuhlmann</i>	128
Paper index.....	137
Volumes published in the series “Bornimer Agrartechnische Berichte”.....	139

We want to thank the following partners for supporting the conference:



JOHN DEERE



HAMM



VÖGELE

HYDAC SOFTWARE



AMAZONE



Making mobile machines perform
Efficient | Safe | Green ■ ■ ■



A Competence
Center of
osb
ENGINEERING & IT

Some challenges to address in order to target the second generation of agricultural robots

Michel Berducat

*Irstea, Technologies and Information Support System Research Unit, Aubière, France
E-mail: michel.berducat@irstea.fr*

Abstract: Beyond some scientific and technological challenges, this presentation will underline several other criteria to consider in order to give the key for a real market development of agricultural robots in close relationship with the operational needs and the constraints of farmer end-users.

Key words: Agricultural robotic, challenges, market access conditions, end users

1 Introduction

Digital farming will favour the increase of the productivity whilst in the same time the sustainable development of agriculture. In one of its synthesis document (CEMA, 2017) the European Agricultural Machinery Industry Association clearly defines the terms of “Digital Farming & Agriculture X.0”. The Agriculture 3.0 was in link with the 1990-2000 timing decade with early adopters of GPS guidance assistance systems, yield mapping on combine harvesters and first telematics technology used to monitor vehicle fleets. The 2000-2020 period corresponding to Agriculture 4.0 boosted the Precision Agriculture, thanks to the evolution of several technologies in terms for example of i/ some cheap sensors and actuators, ii/ low cost micro-processors, iii/ high bandwidth cellular communication. The next Agricultural 5.0 (with full expression from 2020 year) will be devoted on cloud and Big Data analytics. Autonomous decision systems given by Artificial Intelligence and unmaned operations given by robotic systems will be also resolutely parts of Agriculture 5.0.

Agricultural Robots are announced to play a key role in agriculture domain. Today effectively, farmer end users put more attention and interest to robotic solutions. If in livestock production area, robotic market already exists, robotic market for plant production is still in their early stages of development (“Research prototypes” level or in the best case “Early commercial” level). So one main question is: “What are challenges to address in order to favor “Market Penetration” of agricultural robots?”.

2 Still a lot of scientific and technologic issues to solve

Agricultural plant production presents a lot of complex and uncertainty environments. The **Fig. 1** below illustrates some specific bricks to reinforce in order to reach real operational agricultural robots.

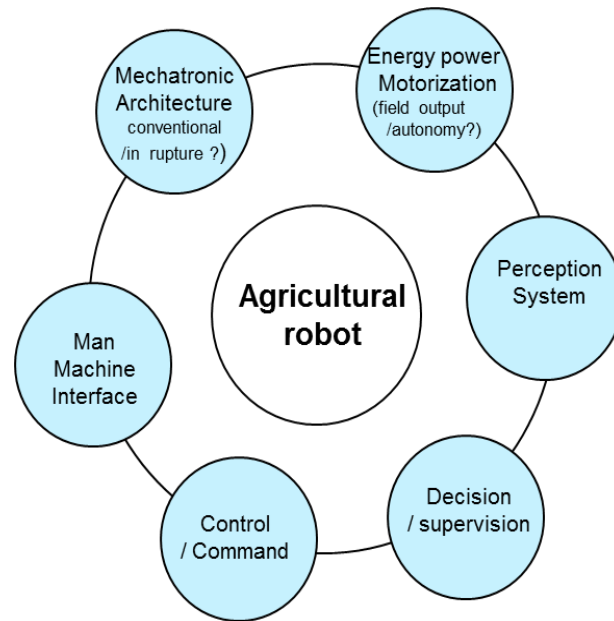


Figure 1: Robotic bricks

Some efforts in term of perception (ex: sensors fusion), decision (ex: AI) and control/command systems must be carried out by complementary actors (manufactures, components suppliers, integrators, researchers...). As example we can mention the case of early commercial sales for robotic weeding solutions. Currently, these last ones are moving at low speed on flat and well-structured open fields. High performances are absolutely necessary to evolve in more harsh conditions (presence of slope terrains, sliding disturbances, complex environments, high speed...).

Robotic offers also huge possibilities to reinvent agricultural machines in term of mechatronic architectures, energy power motorization, cooperation of several small, medium (or big!!) smart machines working together under the supervision of one remote human operator...A lot of scientific and technologic developments still must be done in order to increase the performances of all the bricks involved in the whole robotic systems.

Today we assist to an explosion of agricultural robot solutions coming from various part of the world. Presented results show in general a very good functioning of the solutions relayed directly by their own developers or / and by public or professional Medias (ex: video supports). These results which give the impression that "all is perfect and soon available" are generating growing interest among farmers and their representatives. Achieving the interest of End users which are the farmers, does not mean triggering the final purchase of the robotic solutions by these farmers. In the next chapter, some criteria (list not exhausted) must be taking into consideration in order to facilitate the acceptance by the end farmers of robotic solutions.

3 Some other important criteria to consider for the dissemination of agricultural robots

The Fig. 2 introduces a second constellation of satellites (in yellow colour) about criteria to take into account in order to satisfy the needs of End Users and thus to give some keys for a real market development of the agricultural robots.

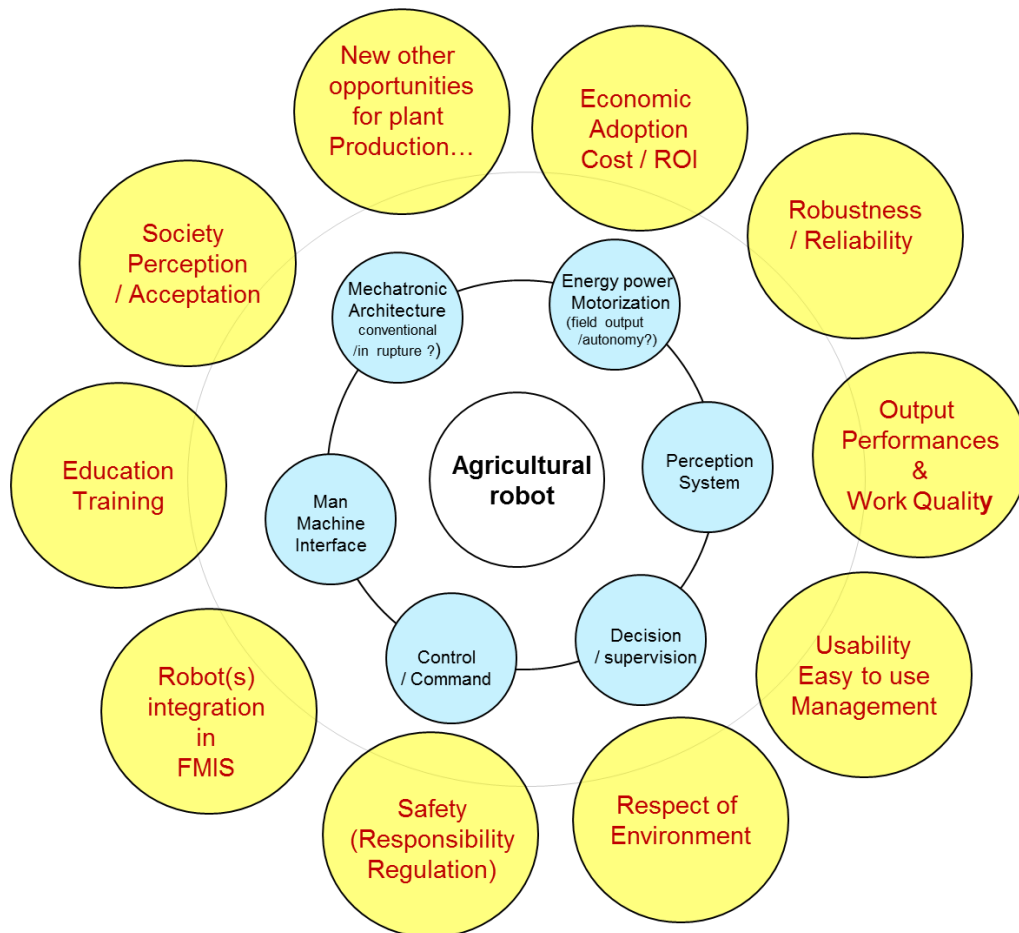


Figure 2: Other criteria to consider from End-User position

3.1 “Economic Adoption Cost” criterion

Never the final Customer (except exception!!) buys a machine for its high technology, but for its ability to provide added value in terms of Return On Investment. One possibility to optimize the ROI is to optimize the “Robot - Agro System” couple. As illustration, in the Figure 3, the author (DEGANI, 2015) compares by simulation the cost of different robot architectures (composed of 3 or 4 Degree Of Freedom) for picking fruits in three tree configurations (“Central leader”, “Tall Spindle”, “Y-Teillis” pruning modes). Resolutely the “Tall Spindle” training system with more compact and wall spatial disposition of the fruits on the tree can use the robot with lowest cost function.

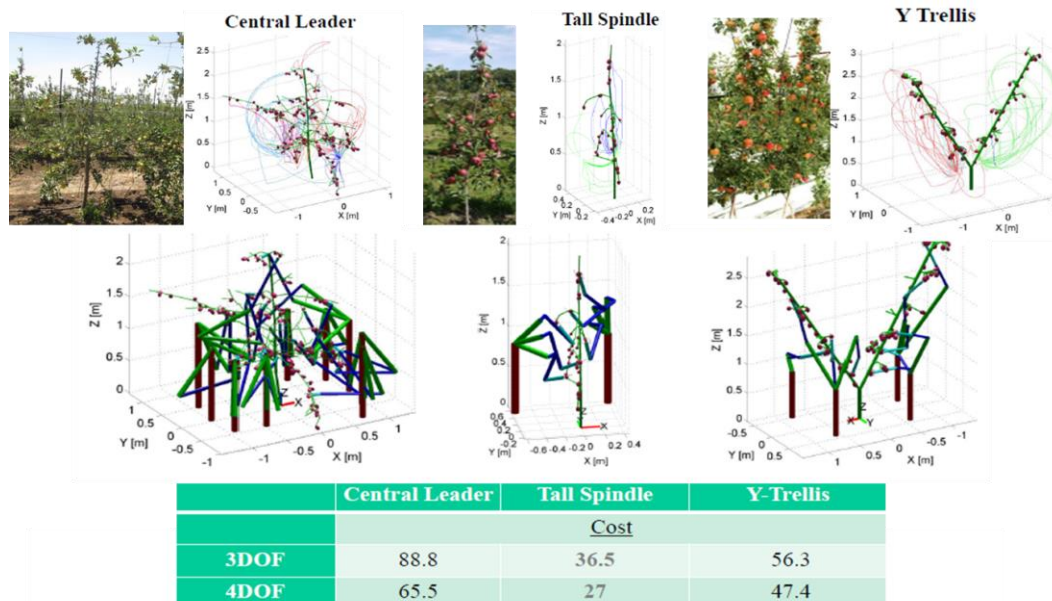


Figure 3: Example of the “Robot – Agro System“ optimization

So affordable cost robots could be more easily achieved by simultaneously adaptation of morphology of plants. Robot Technology and Agronomy communities are thus called to work together.

3.2 “Robustness” and “Output performances” *criteria*

Robustness and out-put performances of robotic solutions are also essential for the End-users. Staying always in the Fruit picking robots domain, a lot of developments show poor yield out-put with long execution cycle time (several seconds) to detect the fruit, launch the arm to fetch the fruit, collect the fruit and arrange it in the conditioning box before to restart a new cycle. Under the respect of previous criterion (“Robot - Agro System” optimization), we advance the hypothesis that “simple architecture robotic machine” gives additional asset to improve robustness and output performances. An example of “simple robotic machine” is the automatic apple picker developed by FFRobotics (GOODFRUITGROWER, 2017) with two main elementary linear mechanic devices to reach fruits in the vegetation wall.

3.3 “Easy to use” *criterion*

Demonstrations of agricultural robots are always showed in the field. In fact, “agricultural robotics doesn’t start in the field, but inside the yard of the farm!!!”. That means that End-users will be attentive to all the phases of the mission of the robot: Preparation, Execution, and Finalization, and not only during the execution work in the field. The phases of preparation and finalization of the mission integrate a lot of logistical operations, for example with the connexion of implements on the robotic platforms. Thus, one asked question is about the execution facility of manoeuvres for implement linking oper-

ation from remote screen tablets? In the case of deployment of several robots (swarm robots), the End users will be concern by accentuated logistical issues with a lot of fuel tank to fill-up each morning, or batteries to charge each morning and other time during the day !!. So for the development of agricultural robot market it is capital that developers bring suited solutions for all the phases of the mission in terms of Usability / Easy to use of the solutions in order to obtain complete satisfaction from End-users.

3.4 “Respect of environment” *critierion*

As introduce in chapter 2, Robotic offers huge possibilities to reinvent agriculture machinery with for example cooperation of small or medium size robots working together (BLACKMORE, 2008, BERDUCAT, 2007). Thanks to robotic technologies, this approach gives new alternatives to the single way evolution of agricultural machinery proposed during the last century: “always bigger, always powerful...but always heavier!!”. The opportunity to suppress the compaction of soil deep layers (30 cm to 1 m depth) by suppression of big machines paths is a real benefit for sustainable agriculture. In the case of small robots (working or not in cooperation), one question nevertheless must be put on the table: “With a footprint on 90% of the surface area (due to small track, repeated paths) what about superficial compaction generated by these machines in certain working conditions (type of soil, moisture)?”.

3.5 “Safety” *criteria*

The rise of robotic in general and agricultural robotic in particular is depending of safety guarantees which will be given by the manufactures. The mobility increasing of robots in their working environment in autonomous modes requires a special attention on safety associated devices. Safety devices for agricultural robots don't be limited to detection of obstacles (static or dynamic, positive or negative, known or unknown). The preservation of the robot integrity needs other security modules (hard and soft). For example, taking into consideration the presence of slope terrains and/or tanks or hoppers embedded on the mobile robotic platform that can fill-up or empties during the work execution, it is necessary to have safety devices able to anticipate dynamic instability or roll-over risks (Lenain,2013). Physical or virtual geo-fences are also an obligation in open field areas in order to guarantee that agricultural robots will stay in their dedicated work areas.

3.5 “Integration in FMIS” *critierion*

Concerning agricultural robots in plant production and open fields, we are just at the beginning of the history!!.. Currently, agricultural sites welcome only one or two robots in the same place under the close supervision of a human operator at proximity. For the real boom of the robotic in agriculture (in particular for big farms), it is absolutely necessary to go past the level of the lonely machine in its field. Robots must be full integrate

in the Farm Management System (FMS) able to plan, control and supervise all the fleet of robots working at the same time in several field areas of the farm.

Farm Management Systems (Digital Farming tools) exist today to share information in real time about exchange of spatio-temporal data in the frame of Precision Agriculture. These tools must progress and be adapted to the arrival of agricultural robots (which is not the case today). To facilitate this evolution, agricultural robot community must take benefit of developments done in industry sectors. The figure 4 (PUGLIESI, 2014) presents the five functional levels of a manufacturing control operation in industry sector. The two low levels standards (Level 0 and Level 1) correspond to levels embedded on the physical machine. Upper levels (2, 3 and 4) will respectively permit to supervise, control and schedule all the robots to the right stage has to be digging.

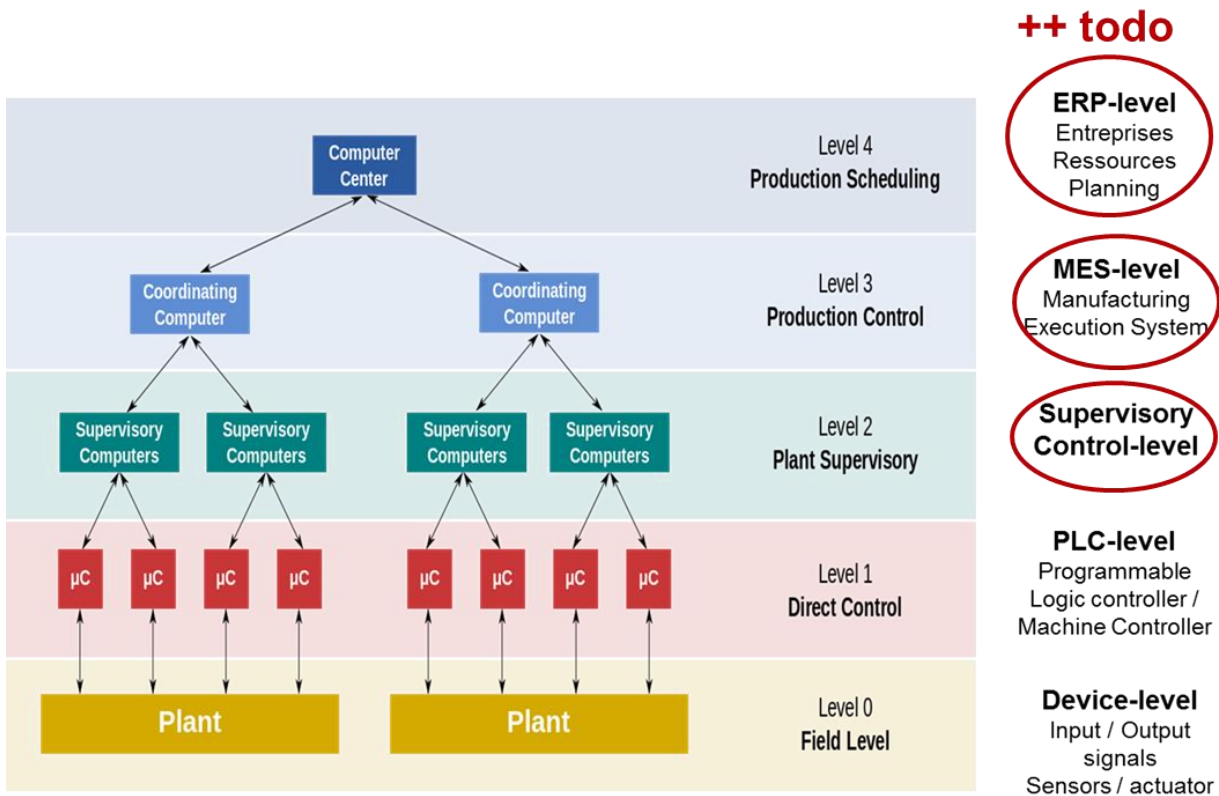


Figure 4: Integration of agricultural robots in FMS

3.7 “Education Training” and “Society acceptance” criteria

The introduction of robotic solutions in farms requires some precautions. Manufactures must take care to propose adapted training to their customers in order to educate them to these new advanced technologies. No saving can't be done in this domain, if the agricultural robotic community wants to success. In the same manner, transparent exchanges between all the actors of the Value Chain (researchers, manufactures, distributors, farmers) must be develop toward civil Society in order to explain and demystify the role of robotic in agriculture.

4 Conclusion

The aim of this paper was to underline huge challenges to solve for the development of agricultural robots. Challenges concern a lot of scientific and technology issues in order to reach performant robotic offers with appropriate associated solutions in terms of safety functions and target cost. To convince customers, developers must also take care to consider all the phases of the mission of the robots (and not only functioning inside the field). Logistical aspects in the farmyard, between farm yard and fields must be also proposed to end users to offer complete operational solutions. To increase the maturity level of robotic solutions for agriculture, it is also necessary to break up the current limiting approach, consisting to use robots as lone units. Tomorrow mobile robotic platform(s) must be fully integrated in the whole Farming Management System, one more, not only during mission execution inside the field, but also during the mission preparation from the farm yard (linkage of implements, full of energy...).

References

- BLACKMORE BS (2008):** A specification for an autonomous crop production mechanization system. University of Thessaly, Greece, ICPA, 9th Denver, July 2008: 16p.
- BERDUCAT M (2007):** Evolution of agricultural machinery: the third way. 7th European Conference on Precision Agriculture, Wageningen, NL: 363-369.
- CEMA (2017):** Digital Farming: What does it really mean? <http://www.cema-agri.org/page/digital-farming-what-does-it-really-mean>
- DENIS D (2016):** Online adaptive observer for rollover avoidance of reconfigurable agricultural vehicles. *Computers and Electronics in Agriculture* 126: 32-43.
- GOODFRUITGROWER (2017):** <https://www.youtube.com/watch?v=UaL3UxUclKY&t=22s>
- PUGLIESI D (2014):** <https://commons.wikimedia.org/w/index.php?curid=31527335>

Development of a learning tractor implements coupling application

Tobias Blume, Ilja Stasewitsch, Jan Schattenberg, Ludger Frerichs

Institute of Mobile Machines and Commercial Vehicles, TU Braunschweig, Germany

E-mail: t.blume@tu-bs.de, tel.: +49 531-391 7187

Abstract: This paper presents a developed, implemented and tested new assistance system for tractors and mobile machines based on a stereo camera. The focus is on the learning automated coupling process between tractor and implement.

Key words: deep learning, driver assistance system, object recognition, pose estimation, tractor/implement coupling

1 Introduction

In order to utilize the high performance of modern agricultural machinery by the operator side, an increasing number of driver assistance systems is necessary. Only this way the operator can be relieved of the monotonous and tiring work and is capable to control complex processes safely and at high efficiency.

The aim of this project at the Technische Universität Braunschweig was to develop, implement and test new assistance systems for tractors and mobile machines based on a 3D sensor. The investigation based on promising research experiences with 3D sensors in autonomous vehicle projects (BLUME *et al.*, 2015, ROBERT *et al.*, 2013). Therefore, the widest possible range of applications in the areas of efficiency, safety and comfort should be covered. The camera was attached on the rear part of the tractor in order to capture a three-dimensional image of the backward area. Based on this data, the following applications should be realized:

1. Optical implement recognition to parameterize the machine settings automatically for this device
2. Automate the tractor/implement coupling even under difficult viewing conditions
3. Increase the lane guidance accuracy of implements with orientation and position information of implements
4. Develop a trailer assistance system to simplify the reverse driving of a tractor-trailer combination
5. Collision avoidance to increase the safety of human and machine while driving backwards

The project was started at the middle of 2014 and ended at the end of 2017. The research work was possible due to funding by a BLE/Rentenbank program; associated partner was AGCO/FENDT. The focus on this paper is on the automated coupling process and describes a solution for a learning automated coupling assistant based on neural networks.

2 Material and methods

2.1 System description

The system consists of a stereo camera (S21 Multisense) mounted on a Fendt 724 (BLUME *et al.*, 2018). A laptop serves as a computing unit and processes the data from the stereo camera and calculates a steering angle and a speed for the tractor. Both data are written to the tractor's own CAN bus. On the software side, the system can be divided into three problems: computer vision part, path planning part and path tracking control part. BLUME *et al.* (2015) and BLUME *et al.* (2016) presented solutions for all three problems. Traditional algorithms were used for computer vision part. A five-dimensional spline was used for path planning and the path tracking control is based on a model predictive controller.

In a newer approach (BLUME *et al.*, 2018) the computer vision part (attachment detection and pose estimation) was determined using the neural network *yolo3*. This approach allows higher detection rates with a larger number of different implements. But this requires significantly more training data than traditional methods. For the training of a single implement a few hundred pictures were labeled by hand in different scenarios under different lighting conditions. A variety of different neural networks for object recognition, for 2D and 3D, with very high recognition rates are available online as open source. In contrast, the labels for localization are not available in most cases. Position labels are hard to get as they cannot be written manually without spending precious time doing very precise measurements for each sample (GUÉRIN *et al.*, 2017). In the following, we describe methods to obtain these labels.

2.2 Approach Overview

In the first approach we observe the operator during work and use the information from vehicle movement and sensor to automatically label the implements. Therefore we need to determine the point of coupling where the implement is in the correct position just behind the tractor. To determine this point we use three different information from the tractor. The speed of the vehicle, that must have been negative before, the hydraulic control, which have to be moved upwards, and the force on the lower links. To decide whether it is an already known implement or not we compare all known models of our implements with the current point cloud by calculating the Euclidian fitness score. If it is an unknown implement we are doing a segmentation to obtain the new model. The step is critical because the model will be used later on. Instead of using the point cloud of the

sensor data directly, it is recommended to use the map of a SLAM algorithm. This has the advantage that the model is not only modeled from one view and on the other hand the input data is much less noisy.

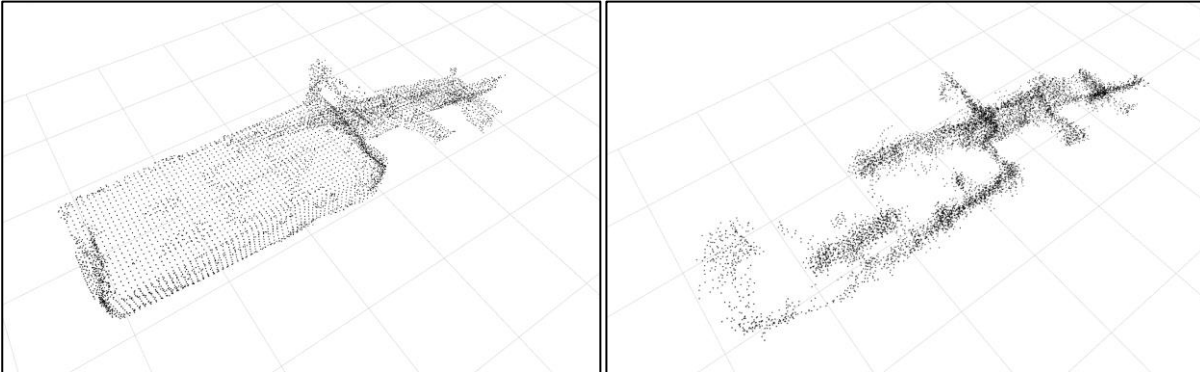


Figure 1: Model of a mowing unit. On the left side recorded with a SLAM-Algorithm, on the right side the model is created directly with the sensor data.

After that we can determine the relative position between tractor and implement over the last 10 meters that the tractor has travelled using a combination of odometry and stereo odometry. Depending on the neural network, the position data (X , Y , Z) can already be used as a label. For object recognition with a 2D convolutional neural network (CNN), the position data must be converted to pixel values. Therefore, the outermost points of the implement must be determined. The easiest way to do this is to transform a model of the implement to the calculated position and to determine the max and min points in x and y direction from the camera perspective. By multiplying the camera projection matrix with those points we obtain the bounding box of our implement. For a semantic segmentation using deep learning all points of the model are converted to pixel values.

In the second approach, we try to generate synthetic images in a simulation environment using Unity, a development environment for games. In this environment we can produce thousands of images in a few minutes under different lighting conditions. To create as realistic images as possible we do not use a CAD model of the implement in the simulation environment but have created the implement with the program Agisoft PhotoScan (AGISOFT, 2018). Agisoft PhotoScan is a software product that performs photogrammetric processing of digital images and generates 3D spatial data. The information required to label the synthetically generated images can be read directly from the simulation environment.

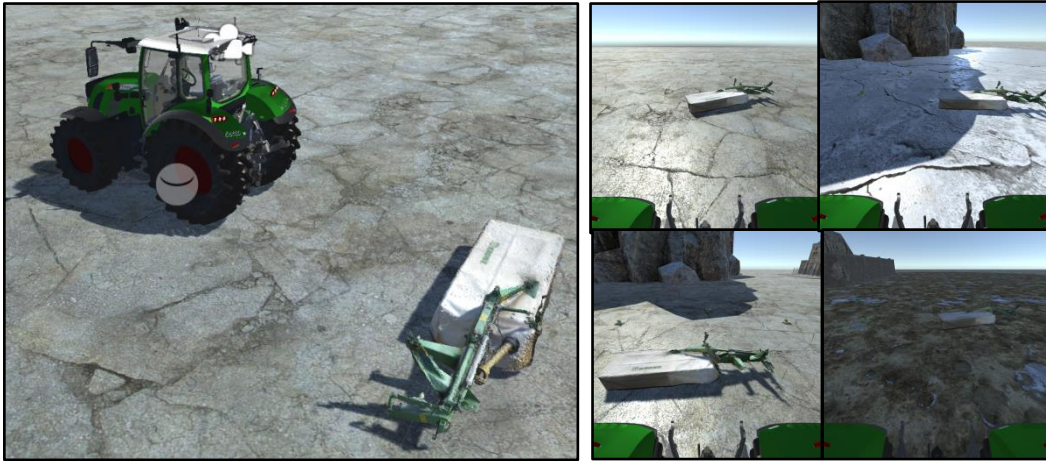


Figure 2: Tractor and implement in the used simulation environment Unit

In the last approach, we create images and labels by transforming the model of an implement previously created with PhotoScan into real images. The goal is to seamlessly blend the object from a source image into the target image. For this we use a technique called poisson blending. It is a gradient domain image processing method that tries to optimize the value in the unknown area between source and target image (GURRIN *et al.*, 2014).



Figure 3: Image blending with source, mask, target and result image

2.3 Dataset description

For the first approach we recorded the images of the stereo camera as well as the stereo odometry and the required tractor data while we coupled from 13 different positions at five different locations on our yard. An image was recorded after the position had changed by at least 10cm. During the tests we were able to collect 1093 images and labels.

For the second approach we created 3000 images and labels with five different types of ground textures and a random set of 10 different background objects.

For the last approach we recorded 240 background images and placed our implement in 12 different positions in each image.

For the validation we used a data set consisting of 556 images. These images were recorded with the same sensor as for training data. However, the position of the sensor was varied in height, a different location in the same area was used and the light conditions were changed.

3 Results

First, the automatic labels for 2D object detection are compared with the manually created labels for evaluation. The area of Intersection over Union is calculated and expressed as a percentage. This means that a value of 50% can be interpreted in such a way that the overlapping area is as large as the areas that do not overlap. **Fig. 4** shows the results for the accuracy of the automatic labeling. For over 60% of the data, the accuracy is over 90%. Furthermore, the accuracy of only one image is less than 70%. The accuracy depends essentially on the odometry, the driver and the shape of the implement. With an angular error of 2.5° , coupling to the mower unit shown in the image is still possible, but already leads to a loss of accuracy of up to 30% to an overlapping of 70%.

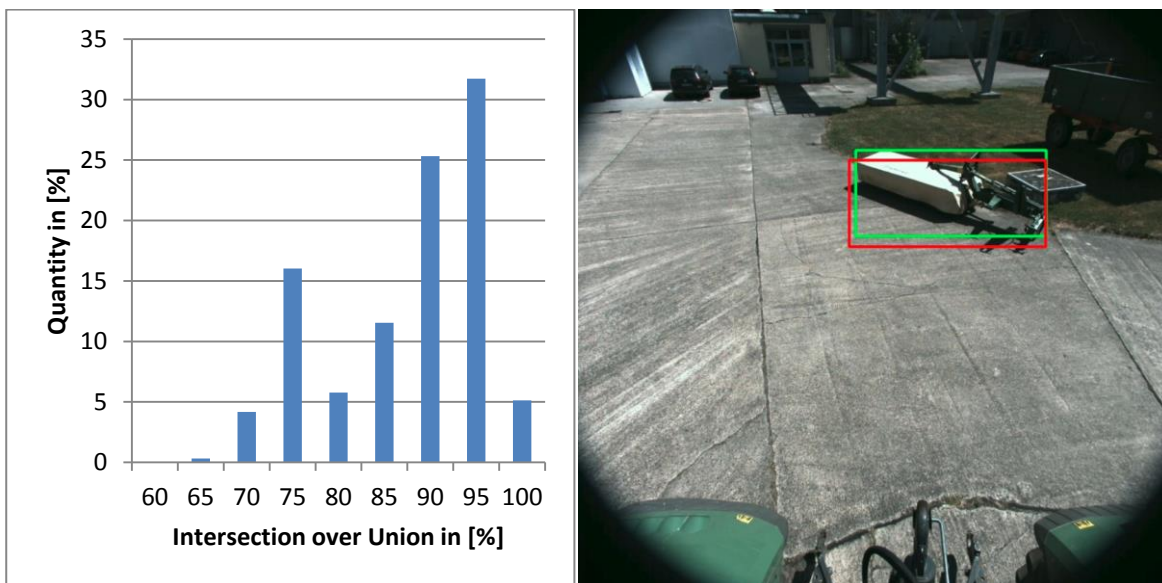


Figure 4: Intersection over Union for the automated label data (red Box) and the hand labeled data (green box)

After we showed that the automatically generated labels correspond to human made labels, we train the neuronal network yolov3 (REDMON & FARHADI, 2018), which we used for the implements coupling application presented in a former publication (BLUME *et al.*, 2018). We started to train the neural network with the data of one location up to five locations. For each training set we used the same hyperparameters and didn't apply any kind of data augmentation to our datasets. In the second chart we compare the results of our poisson blending dataset and the simulated dataset against a human labeled da-

taset. For each dataset we compute the precision (the fraction of relevant instances among the retrieved instances) and the recall (the fraction of relevant instances that have been retrieved over the total amount of relevant instances).

Precision and recall are slowly improving as the number of training data increases. Already the images obtained by coupling at one location are sufficient to determine the attachment and its 2D position in most cases. Despite the use of real textures, the generated data only partially correspond to reality. The data generated by poisson blending is particularly convincing in terms of accuracy. This is not surprising, as the labels are error-free.

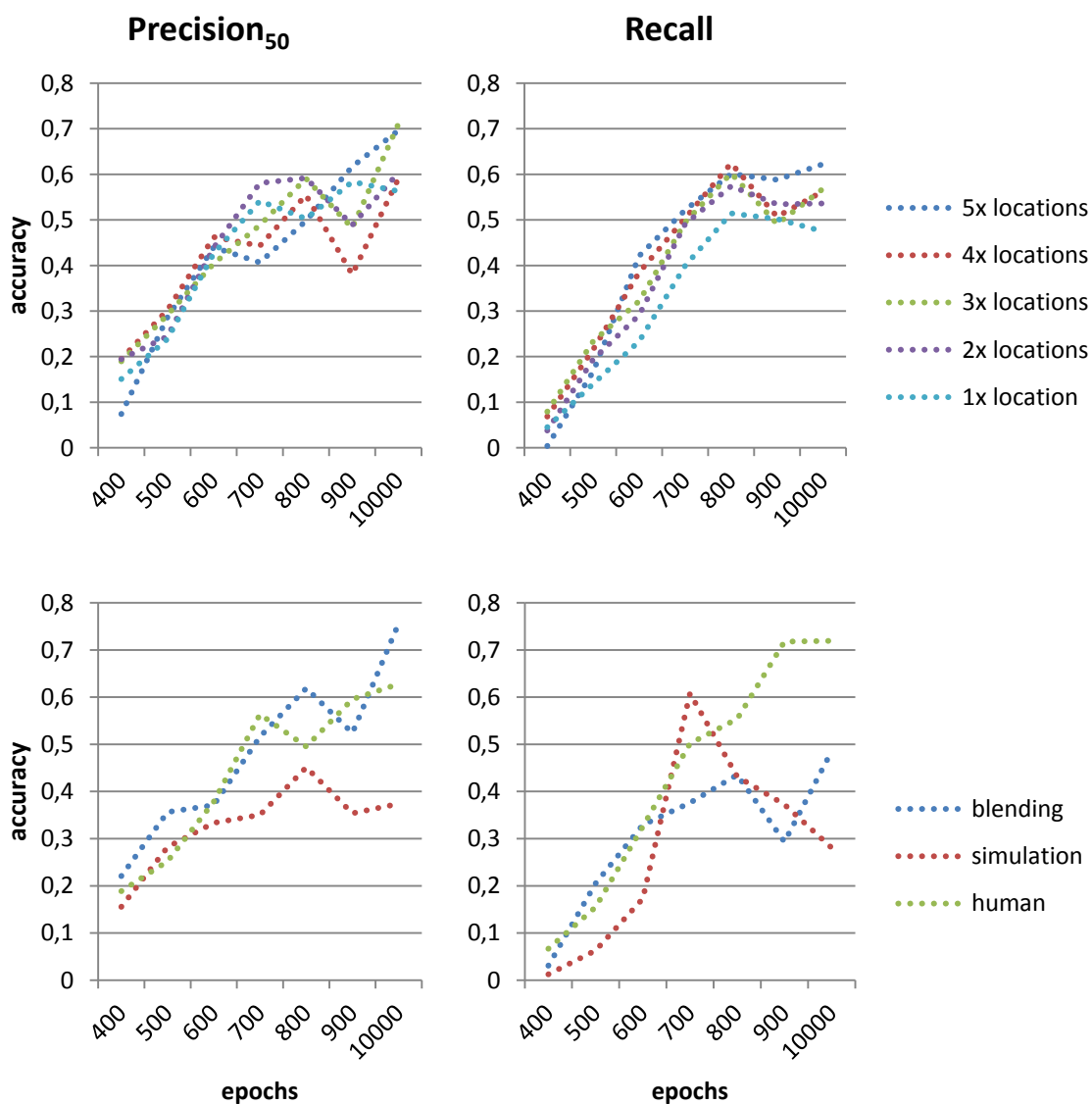


Figure 5: Precision and recall for the three different approaches compared to human labeled data over growing training epochs

4 Discussion

We presented three different approaches to generate data for a neuronal network and validated these data on the convolutional neuronal network for 2D object detection yolov3. Our simple simulation environment is not sufficient to create photorealistic images that represent the real world. Better results can be achieved by inserting models of attachments into real images, especially if the images were created in the working environment. Observing the operator at work has proven to be a very simple method to generate a lot of data and can be used in many applications where the position of an object at a certain time is known and can be tracked. If it is possible to increase the accuracy of the labels, the accuracy of data labeled by humans can be surpassed with this method.

References

- AGISOFT.** Agisoft PhotoScan, Accessed 20 June 2018. Available from: <http://www.agisoft.com/>.
- BLUME T, SCHATTENBERG J, FRERICHS L (2015):** Innovative Assistance Systems based on a Backward-Looking 3D-Time of Flight Camera. 73rd International Conference on Agricultural Engineering LAND. TECHNIK AgEng.
- BLUME T, STASEWITSCH I, SCHATTENBERG J, FRERICHS L (2016):** Automated tractor/implement coupling based on a backward-looking 3D-Time-of-Flight Camera. 5th International conference on Machine Control & Guidance.
- BLUME T, STASEWITSCH I, SCHATTENBERG J, FRERICHS L (2018):** Object recognition and position determination in agriculture using the example of a coupling assistant. *LANDTECHNIK – Agricultural Engineering* 73(1).
- GUERIN J, GIBARU O, NYIRI E, THIERY S (2017):** Automatic Construction of Real-World Datasets for 3D Object Localization using Two Cameras. Computing Research Repository, abs/1707.02978.
- GURRIN C, HOPFGARTNER F, HURST W, JOHANSEN H, LEE H, O’CONNOR NE (EDS.) (2014):** MultiMedia Modeling: 20th Anniversary International Conference, MMM 2014, Dublin, Ireland, January 6-10, 2014, Proceedings. Springer.
- ROBERT M, LANG T (2013):** Development of simulation based algorithms for livestock robots. *LANDTECHNIK – Agricultural Engineering* 68(4).
- REDMON J, FARHADI A (2018):** Yolov3: An incremental improvement. Computing Research Repository, abs/1804.02767.

Automatic machine and implement identification of an agricultural process using machine learning to optimize farm management information systems

Thoralf Stein, Henning J. Meyer

*Technische Universität Berlin, FG Konstruktion von Maschinensystemen, Straße des 17. Juni
144, 10623 Berlin, Germany*

E-mail: thoralf.stein@tu-berlin.de, tel.: 0049 30 314 22141

Abstract: In order to increase the usability and benefit of a farm management information system (FMIS), we propose an automatic assignment of the used machine and its implement for work processes. To accomplish this, we do segmentation and classification of the GPS tracks. The here presented algorithm cleans and sections the recorded work logs. This is followed by the extraction of various parameters, which are used for the classification. Herefor we examined different classification approaches and developed an algorithm, whose initial results are promising but need to be improved in the future.

Key words: machine learning, farm management information system, data mining, agricultural processes, automation.

1 Introduction

In today's agriculture, comprehensive documentation of the fieldwork plays an important role. It is needed for various reasons like managing, risk assessment, accounting and legal purposes. Data loggers or smart devices are used to record the work process of a farm machine. The recorded work logs are saved and processed in an FMIS. As stated by STREIMELWEGER (2018), the important tasks of a FMIS is the correct recording and an easy handling for the user. Although many FMIS already exist, nearly none of them meets the requirements. Many farmers are not capable of taking full advantage of those strong tools, because of their complexity and operating expense (NOVKOVIC *et al.*, 2015). Services like 365Farmnet or MyJohnDeere offer different support systems to facilitate the handling. For example, they offer an automatic assignment of the machine and implement to the work log (LÖBBECKE, 2018). However, there is a big disadvantage: The support services need additional recording hardware on the machines to provide ISOBUS-Data (BÖHRNSEN, 2012). This is an additional financial barrier apart from the complexity issues explained. The acceptance could be higher, if smartphones or cheap GPS-tracker could be used for recording. Therefore, the assignment algorithm has to supply correct results only by using GPS-tracks.

For companies with a small fleet of machines and implement, an algorithm based on analytical evaluation could be accurate. However, identifying the significant parameters

for the assignment in a larger company with a variety of machines and implements is not realizable. There are too many implements with similar working width and speed (FRISCH 2018). Here, modern tools from the field of machine learning can help. They can be used to identify significant parameters for classification as well as for assigning the work processes via classifying algorithms. Based on existing data, a classifier can be trained. This is also the disadvantage of those data driven algorithms: they need training data. However, as the FMIS provider has access to the data of several users, they can be used as database.

The classification algorithm described in this work is developed in the course of the project "Big Data im landwirtschaftlichen Prozess innovativ nutzen" (BiDa-LAP). The aim of the project BiDa-LAP is to develop an electronical system, consisting of a platform architecture and mobile data loggers with the possibility to interact with smart devices. The system will be available as an operational and strategic decision support system for farming and service companies. It is designed to assist the user in decision-making through various indicators (e.g. organizational, economical and sustainable).

The algorithm is developed by means of data of two agriculture farms in Saxony, Germany. The data is recorded with data loggers from Logicway, a member of the project consortium. The used database contains the GPS tracks of all machines and the field boundaries. There is CAN data, like percentage torque, for some machines as well, but as HEIZINGER (2014) stated, it is better to take the minimal data set. This is just the GPS position, which makes the classification more solid and there are less variables to monitor. Furthermore, this is also the aim of this work. In addition to the database, there is a daily work journal of one of the farms. The algorithm shall have the ability to classify the work process of the other farm, which has no daily work log. It also shall recognize transport processes.

2 Material and Methods

The general procedure for the classification can be divided into the following steps: (1) cleaning and segmenting the work log data, (2) extracting the predictors for the classification, (3) train and evaluate a classifier to group field or transport work days and (4) train and evaluate a classifier for each implement/work type.

The work logs used for training are recorded by five data loggers on a middle sized farm. The record frequency is 1Hz and the recording starts automatically when the engine starts. The data logger sends a data package to the server every 20 minutes.

The algorithm uses the data for accuracy of the GPS-signal, the horizontal dilution of position (HDOP) and the number of satellites, to clean the work log. Data points with insufficient values are therefore smoothed by the surrounding data points. However, this is only possible up to a certain number of points. Otherwise, it would falsify the data.

After this process, the work logs are segmented into days for the classification into field or transport work. For the classification of the fieldwork, the daily work log is also sepa-

rated into single operations. This separation step uses the field boundaries. All data points within and around a specific boundary are assigned to an operation.

The second step is to define the predictors. The selection of the predictors is the most determining factor for accuracy of the classification (BEIERLE & KERN-ISBERNER, 2014). The transformation of the time-dependent work logs into classifiable parameters is an important step in this approach. There are many variables, which are extractable from the GPS track, especially from the speed of the machine and the angle of the driving direction. Over 30 statistical parameters, like average, deviation, range, quantiles and furthermore are calculated from both time series.

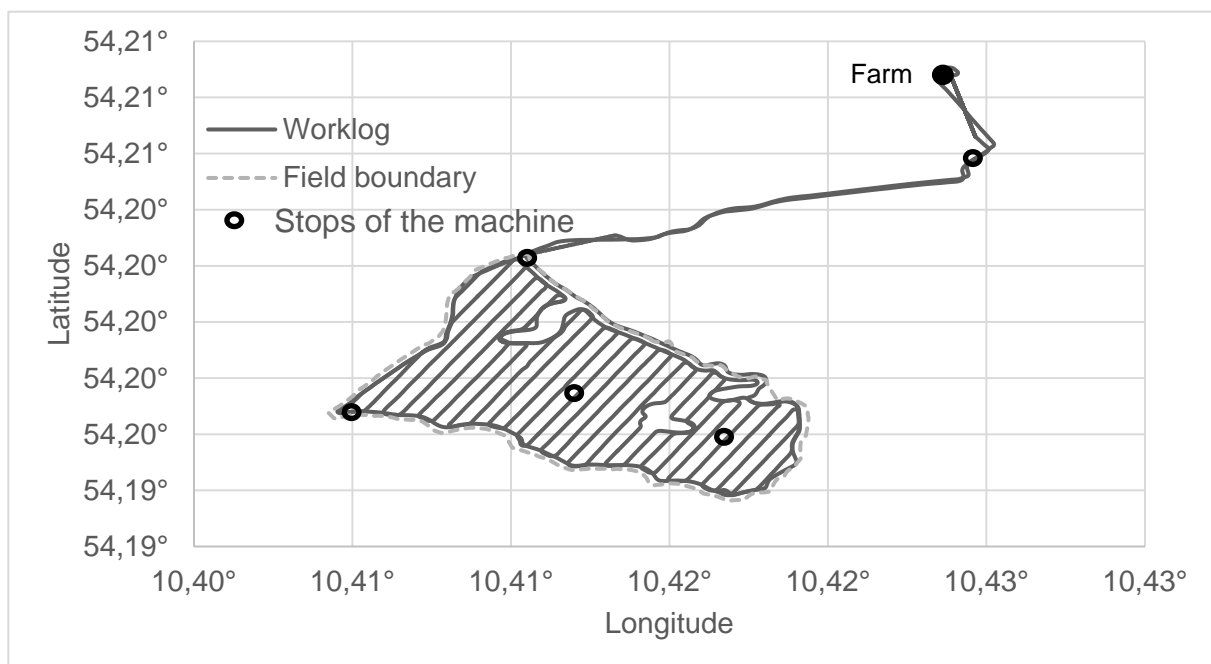


Figure 1: Work log of a single operation on a field recorded by a data logger

Moreover, there are many possibilities to calculate additional parameters. For example, the ratio of time spend on field/not on the field or the duration of a turn on a field. There are also many parameters extractable from the stops of the machine as seen in **fig. 1**. For example, the distance between the stops and the distance of the standing machine to the farm/loading station. It would go beyond the scope of this paper, to describe every calculation method. In total, 26 additional parameters have been determined for the classification.

There are several approaches of classification algorithms. To test as much algorithms as possible, the program Matlab R2016b from Mathworks with statistics and machine learning toolbox was used. It supplies various classification types and supports fast programming and testing. To maximize the feature space and to discover unknown relations between these parameters, the difference and the ratio between some of them are also taken into the consideration for the classification algorithm (HOLLSTEIN *et al.*,

2016). Different classification approaches were tested with the statistics toolbox. 25% of the data sets are used for validation.

For a more accurate result, the classification is done in two steps. At first, each workday is sorted in fieldwork or transport work. This step is possible because of the fact, that the investigated farms almost never switch the type of work during one workday.

On a fieldwork day, the data is separated into single operation to each field through the field boundaries. This is the second step of classification, in which the work logs are assigned to an implement. As a result, the drivings to and from a field do not falsify the characteristics of the work log. In addition, the width of the track can now be calculated and included into the algorithm.

3 Results

The results of this developed algorithm will be shown below. The cleaning and the segmentation of the work log will be inspected. After that, the processing of the work logs will be examined and the evaluation of the two steps of the classification algorithm will be assessed. In the end, all results and their validity are discussed.

3.1 Cleaning/segmenting and extraction of predictors

During the cleaning of the work logs, only a few time series had to be excluded from the training. After segmenting all work logs from the farm, for which the work journal is available, the database contains over 350 days and over 800 operations. For each day and operation, 127 predictors are calculated and used to train the classifiers.

3.2 Grouping of fieldwork and transport

Matlab statistics and machine learning toolbox supports different types of classifiers. It supplies simple ones using decision trees and linear regression. However, there are also complex ones like multiclass support vector machines and K-nearest neighbour. To get an overview, which one might be the best fitting algorithm, all quick to train classifiers tested. The general functionality of the classifying approaches will be not discussed here. Numerous references are given to detailed literature like (WEBB, 2004) and (LAMP- LAND & STAR, 2009). As seen in **table 1**, the different types of classifiers show diverse prediction accuracy values. The best outcomes tend to be achieved by the decision tree classifiers.

Table 1: Accuracy of the prediction for different classifiers

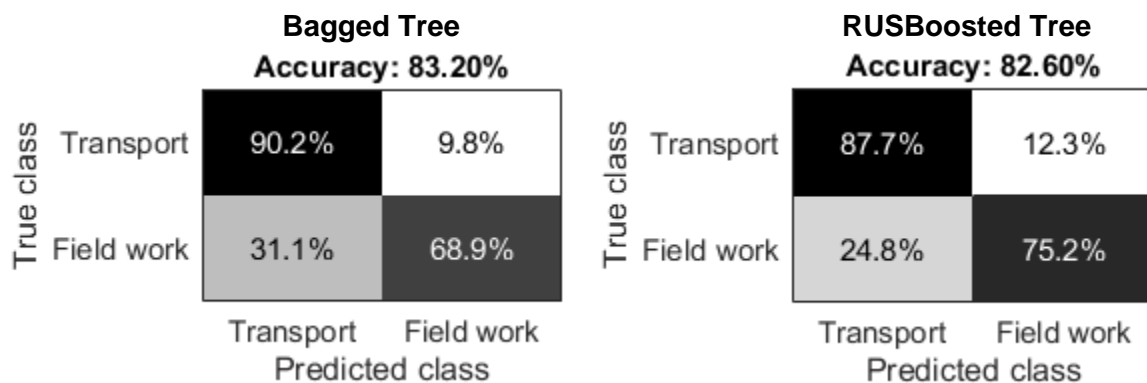
Type	Accuracy
Decision tree	82,50%
K-nearest neighbour	64,20%
Logistic regression	45,80%
Support vector machine	75,80%

There are several options to modify this algorithm and gain even better results. The number of splits can be altered and subtypes like RUSBoosted tree or bagged tree can be used. The results after the modification of the different tree types are shown in **table 2**.

Table 2: Accuracy of the prediction for different decision tree classifiers

Type	Accuracy
Bagged Tree - 20 splits	83,20%
RUSBoosted Tree - 50 splits	82,60%
RUSBoosted Tree - 20 splits	81,30%
Tree - 50 splits	81,30%
Tree - 100 splits	80,60%
Tree - 20 splits	74,20%

A confusion matrix plot is used to assess the results in detail. It shows the true positive and the false negative results for each class predicted with the algorithm. As seen in **fig. 2**, not all trained trees show a balanced proportion in the correct class detection. The RUSBoosted (SEIFERT *et al.*, 2010) decision tree with a maximum split number of 50 provides the best results.

**Figure 2:** Confusion plot of two different classifiers for the prediction accuracy of each trained class

The advantage of the type of decision tree is based on the fact that this approach considers diverging numbers of samples of each class. The smallest accuracy is 75% of the class 2, which in this case is the fieldwork. This is acceptable for the cause of this algorithm. The next step is the validation with the data from the second farm. The result of the validation is an accuracy of 70%. This is not as good as the results from the training data. The diverse quality of the data can lead to different classification parameters. In addition, the approach of organization and execution of the fieldwork can differ.

3.3 Classification of the fieldwork

The second step of the algorithm is the classification of the fieldwork. For better results the calculated width of the tracks and the month are also taken into the classification. The procedure is very similar to the procedure of 3.2. The difference between them is the number of classes. There are mainly four classes of processes in agriculture (TOLL, 2013). In addition, there are several operations, which are not falling into those classes, like swathing. These operations are included in a fifth class. Again, a decision tree is trained by the means of the described variables. As seen in **fig. 3**, the accuracy results for all classes are sufficient. A RUSBoosted decision tree was also used for this classification step, because of the equally accuracies for each class. When the class of the fieldwork is identified, an implement fitting to this class and track width is assigned. After that, the matching machine is added to this implement.

The validation for the first step of the algorithm was possible because the difference between the two classes is obviously visible in the plots. Nevertheless, this approach does not work for the second step of classification. Visual inspection of the accuracy is possible, but not fully reliable. This full validation has to be done via the users feedback.

Accuracy: 81.52%

True class	Cultivation	85.2%	0.0%	7.4%	0.0%	7.4%
	Harvest	0.0%	75.1%	11.9%	8.1%	4.9%
	Other	5.3%	4.3%	85.3%	4.1%	0.0%
	Seeding	2.1%	5.8%	2.1%	87.8%	2.2%
	Tillage	9.8%	6.2%	8.7%	2.1%	74.2%
		Cultivation	Harvest	Other	Seeding	Tillage
		Predicted class				

Figure 3: Confusion Plot of a RUSBoosted tree classifier showing the prediction accuracy for each trained class

4 Discussion

The algorithm developed is basically able to classify the work processes of a farm. The approach is capable of assigning different types of fieldwork. The accuracy of a correct result is at least 75% for a process from the farm, from which the training data comes from. The classifying approach can be transferred to other farm businesses but does not provide the same good results yet. A reason can be the choice of the parameters or the fact, that not every possible variable is yet discovered or used. Additionally, a higher number of observation used for the training could help to raise the accuracy. **Fig. 4** illustrates the correlation between the number of observation used for training and the accuracy of the training result.

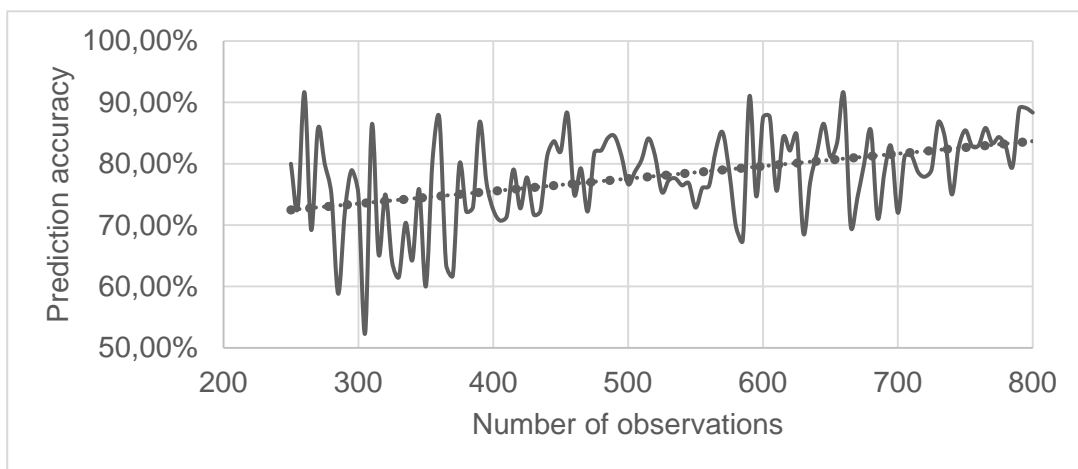


Figure 4: Correlation between the number of observations and prediction accuracy of the RUSboosted tree of classification step 1

In addition, a safeguard could help to make the approach more robust. A possible concept would be to analyse if the assigned work type and implement fits to the crop and the actual month. The crop sequence and the course of action for a specific crop is needed.

Acknowledgement

The project BiDaLAP is fully supported by the Bundesanstalt für Landwirtschaft und Ernährung.

References

- BEIERLE C, KERN-ISBERNER G (2014):** Methoden wissensbasierter Systeme. Grundlagen, Algorithmen, Anwendungen. 5., überarb. und erw. Aufl. Wiesbaden: Springer Vieweg (Computational Intelligence). Available online at <http://dx.doi.org/10.1007/978-3-8348-2300-7>.
- BÖHRNSEN A (2012):** Noch mehr Intelligenz ab Werk. JDLink von John Deere. Edited by profi. Münster. Available online at http://www.fischer-landmaschinen.de/fileadmin/download/testberichte_2012/2012.05%20profi%20-%20Noch%20mehr%20Intelligenz%20ab%20Werk%20-%20JDLink%20von%20John%20Deere.pdf, checked on 9/4/2018.
- FRISCH J (2018):** KTBL-Feldarbeitsrechner. Edited by Kuratorium für Technik und Bauwesen in der Landwirtschaft e. V. Darmstadt. Available online at <https://daten.ktbl.de/feldarbeit/entry.html#0>, checked on 9/5/2018.
- HEIZINGER VJ (2014):** Algorithmische Analyse von Prozessketten in der Agrarlogistik. Dissertation. Technische Universität München, München. Lehrstuhl für Agrarsystemtechnik.
- HOLLSTEIN A, SEGL K, GUANTER L, BRELL M, ENESCO M (2016):** Ready-to-Use Methods for the Detection of Clouds, Cirrus, Snow, Shadow, Water and Clear Sky Pixels in Sentinel-2 MSI Images. *Remote Sensing* 8(8): 666. DOI: 10.3390/rs8080666.
- LAMPLAND M, STAR SL (Eds.) (2009):** Standards and their stories. How quantifying, classifying, and formalizing practices shape everyday life. Ithaca, NY: Cornell University Press (Cornell paperbacks).
- LÖBBECKE M (2018):** Optimale Übersicht und komfortable Dokumentation. 365Active System. Edited by 365FarmNet GmbH. Berlin. Available online at <https://www.365farmnet.com/produkt/365active-system/>, checked on 9/6/2018.
- NOVKOVIC N, HUSEMAN C, ZORANOVIC T, MUTAVDZIC B (2015):** Farm Management Information Systems. Edited by HAICTA 2015. University of Novi Sad, PhD, Professor, Faculty of Agriculture, Trg Dositeja Obradovica 8. Available online at http://ceur-ws.org/Vol-1498/HAICTA_2015_paper80.pdf, checked on 9/4/2018.
- SEIFFERT C, KHOSHGOFTAAR TM, VAN HULSE J, NAPOLITANO A (2010):** RUSBoost: A Hybrid Approach to Alleviating Class Imbalance. *IEEE Trans. Syst., Man, Cybern. A* 40(1): 185–197. DOI: 10.1109/TSMCA.2009.2029559.
- STREIMELWEGER R (2018):** Welchen Beitrag leistet ein FMIS für ein modernes Betriebsmanagement? VDI (Ed.): Herausforderungen und Architekturen für Datenintegration in der Landwirtschaft. 21. Arbeitswissenschaftliches Kolloquium, 13./14. März 2018: 169 - 182.
- TOLL C (2013):** Energieorientierte Analyse der Landmaschinenteknik. Untersuchung zur maschinenrelevanten Energiebilanzierung in der Getreideproduktion mit Erfassung von CO₂-Einsparpotenzialen. Dissertation. Technische Universität Berlin, Berlin.
- WEBB AR (2004):** Statistical pattern recognition. 2. ed., reprint. Chichester: Wiley.

Autonomous phenotyping using a mobile manipulator

Camille Dubos¹, Roland Lenain¹, Michel Berducat¹, Frédéric Cointault²

¹*Irstea, Technologies and Information Support System Research Unit, Aubière, France*

²*AgroSup Dijon, UMR Agroecology, Dijon, France*

E-mail: camille.dubos@irstea.fr

Abstract: This paper presents the use of a mobile manipulator, a robotic arm translating on a guide, to achieve autonomous data acquisition on crops in a field. The redundancy imposed by this platform is managed using a collection of concurrent control laws, weighted in real time to increase the end-effector workspace, and optimize the point of view for data acquisition. This opens the way to full mobile manipulation using an autonomous robot holding the system.

Key words: advanced control, mobile manipulator, phenotyping, motion coordination, agriculture robot.

1 Introduction

In order to improve crops yield and reduce the environmental impact of agriculture, phenotyping, and more generally plant monitoring, appears to be a major challenge. Indeed, thanks to regular data acquisition (e.g. pictures of plants), information such as disease detection or growth monitoring can be retrieved (MAHLEIN, 2016). This information can help observing the resistance of different varieties of a plant to a same disease, or it can also help reducing the area where a treatment against a disease needs to be used. However, the study of phenotype implies to frequently acquire data in the field, which is a repetitive and onerous task. An interesting way to collect data appears to be the use of robots, such as aerial drones (LIEBISCH *et al.*, 2015) or mobile robots. The latter can act closely to crops and autonomously in the field, and make Precision Agriculture arises as a new agriculture standard (BLACKMORE, 2016).

As working in the fields involves covering large area, redundant robots seem to be a suitable solution since kinematic redundancies allow their workspace to be extended (MADSEN *et al.*, 2015). Moreover, improvements achieved in the area of off-road robotics are paving the way to the use of robot manipulators for plant treatment (MANN *et al.*, 2014). The gathering of mobile robots and manipulators allows not only extending the workspace of the robot, but also increasing tasks variability and reducing execution time. Then, the coordination between mobile robot control and arm servoing is a matter of great concern (BROCK *et al.*, 2016). This paper proposes a control framework for the use of this kind of robot in an agricultural context.

Dealing with redundancy issues can be achieved in different ways. Indeed, the system can first be seen as one redundant system or two coupled sub-systems and the redun-

dancy can be managed by adding extra tasks to be achieved, or criteria optimisation. In (FRUCHARD *et al.*, 2006), an approach based on adding an extra task for omnidirectional and non-holonomic platform is developed. The idea is to execute a manipulation task, and at the same time, if it is compatible, ensure the avoidance of the arm joints limits. Criteria optimisation can be found in (YAMAMOTO & YUN, 1994), where the manipulability measure (YOSHIKAWA, 1985) is applied to the robotic arm to find a preferred configuration in which the arm must remain as long as possible, while the system is following a trajectory. Similarly, in (BAYLE *et al.*, 2003), the measure of manipulability has been adapted to a non-holonomic mobile manipulator, and directly applied to the system control to solve the operational motion planning problem. In (EGERSTEDT & HU, 2000), two coordination terms, based on the distance between the end-effector and the centre of the mobile base, are implemented in the curvilinear abscissa of the trajectory following formulation. All those aforementioned approaches are applied to motion planning, but in (OGREN *et al.*, 2000), a reactive control is implemented. The coordination of both parts of the mobile manipulator is achieved by means of a coordination factor, applied on the trajectory following of the end-effector, and through the mobile base velocity profile, defined in relation to the distance between the end-effector and the mobile base. The approach proposed here is similar to the latter, but with only one coefficient for both parts, and decoupled redundancies along the different axis.

In our work, the objective is to achieve phenotyping in an open field, using a vision sensor attached to the end-effector of a robot manipulator, mounted on a motorized linear axis (see **Fig. 1**). The main aim is to detect several diseases on beet leaves. For this purpose, the same plant must be observed from different points of view, in order to find the best one to retrieve relevant plant features. Given this statement, the idea is to maximize the arm workspace to enable the change of position and orientation of the sensor around a plant. Also, it is sometimes more convenient not to move the mobile platform if the goal can be reached by the arm alone, to avoid disturbances, such as vibrations, which will impact the vision. The approach presented here then views the system as a combination of two subsystems, namely the robotic arm and the mobile platform. The controls of both parts are coordinated by means of a weighting law that distributes the motion between both parts of the mobile manipulator, so as to optimize the workspace of the robotic arm as it is centred above the plant.

2 Materials and Methods

2.1 Robotic system overview

The system used in this project to phenotype plants has been developed by Robotnik. It is composed of a 6-dof robotic arm (UR5, Universal Robots, Denmark), mounted on a translating platform, which can be seen as a half-gantry (see **Fig. 1**). To acquire images of the crops, a vision sensor is attached to the end-effector of the robotic arm manipulator. In our case, we use a color camera (VLG-40C, Baumer Optronic, Germany). The control of the robot is made with Ubuntu 14.04 and uses the Robot Operating System

(ROS-Indigo) middleware. All the algorithms used were programmed in a combination of Python and C++ programming languages. The acquisition frame rate of the camera is set on 18 fps.



Figure 1: Robotic platform for phenotyping

2.2 Modelling and notations

First, the following notations will be used throughout the paper. We denote then:

- q – the vector of the joint-space coordinates of the robotic arm,
- r_0 – the joint variable of the mobile platform, corresponding to the position of the mobile support on the linear axis,
- $X = \begin{bmatrix} R_{3 \times 3} & P_{3 \times 1} \\ 0_{1 \times 3} & 1 \end{bmatrix}$ – the transformation matrix representing the pose of a point in the global frame, composed of a rotation matrix $R_{3 \times 3}$ and a position vector $P_{3 \times 1}$.

We then use superscripts to define the state of the variables, \cdot^d for desired value and \cdot^{act} for actual, and subscripts to specify the element the variable refers to. For example, X_{EE}^d stands for the desired pose of the end-effector.

A modelling of the robotic arm has been defined using the Denavit-Hartenberg modified convention presented in (KHALIL & DOMBRE, 1999), from which the two following models can be extracted:

- k_f – the forward kinematics model, s.t. $X_{EE} = k_f(q)$,
- k_i – the inverse kinematics model, s.t. $q = k_i(X_{EE})$.

This last model allows finding the desired joint coordinates q^d from the desired end-effector pose X_{EE}^d .

2.3 Motion coordination

In this section, motions of both parts are calculated. Since the system is redundant, extra constraints are needed in order to generate control. A weighting law has been developed in order to assign a motion to the arm, the platform or both, depending on the position to reach.

In the first place, the desired motion is computed from the data sensor, as being proportional to the error between the barycentre and the centre of the image. That desired motion is only a translation along the three axis x , y and z , noted ΔT . From there, the desired position can be easily expressed as the sum of the actual position of the end effector and the desired translation $P_{EE}^d = P_{EE}^{act} + \Delta T = (x_{EE}^d, y_{EE}^d, z_{EE}^d)^T$. Then, we have the desired pose of the end-effector, noted as:

$$X_{EE}^d = \begin{bmatrix} R_{EE}^d & P_{EE}^d \\ 0_{1 \times 3} & 1 \end{bmatrix}, \quad (1)$$

With R_{EE}^d the desired orientation of the end-effector expressed as a rotation matrix, and P_{EE}^d the desired position of the end-effector computed earlier, in the global frame R_0 .

From this position P_{EE}^d , limits of the arm workspace can be retrieved (**Fig. 2**). All that must be known is the radius of the workspace R_{ws} , which can be expressed as a function of the arm features and the desired height of the end-effector z_{EE}^d . As long as the end-effector desired position is within its workspace, the limits are expressed as:

$$Y_{lim,1/2} = \pm \sqrt{R_{ws}^2 - x_{EE}^d{}^2}. \quad (2)$$

If the values Y_{lim} are not null, a representation of the distance between the desired position of the end-effector and the closest limit can be computed by:

$$e_y = \frac{2y_{EE}^d}{|Y_{lim,2} - Y_{lim,1}|}. \quad (3)$$

This equation represents the distance between the desired position and the workspace of the arm along the y -axis within $[-1; 1]$. The sign of e_y provides an indication of the direction in which the mobile platform has to move in order to centre the arm workspace above the plant. Based on that value, a coefficient λ can be computed in order to manage the redundancy along the y -axis. It is expressed as:

$$\lambda(e_y) = \begin{cases} 0.5 \left(\tanh(\mu \pi (e_y - \eta)) + 1 \right) & \text{if } e_y \geq 0, \\ 0.5 \left(\tanh(\mu \pi (e_y + \eta)) - 1 \right) & \text{else.} \end{cases} \quad (4)$$

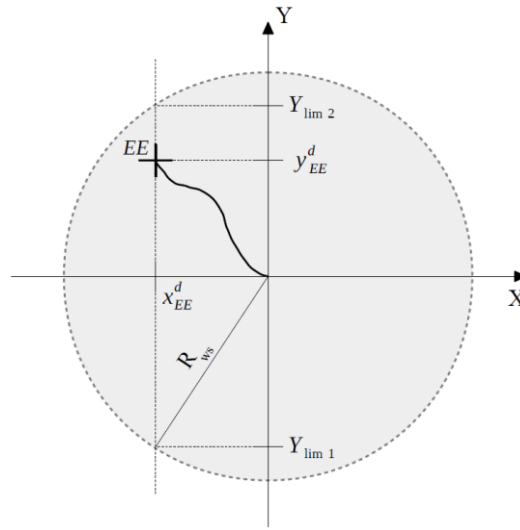


Figure 2: Top view of the workspace of the robotic arm (grey area) at a desired elevation z_{EE}^d

Where μ and η are two parameters that change the behaviour of the function. The first one represents the absolute value of the threshold at which the value of λ changes, so $\eta \in]0; 1[$, and the second one affects the slope of the hyperbolic tangent in such a way that the higher the value, the more abrupt the transition. To guarantee continuity in the vicinity of 0, the condition $\mu \eta > 1$ must be satisfied.

The wanted behaviour here is to move only the arm when λ is null and move only the axis when $\lambda = \pm 1$. Then, the motion of the platform must be proportionate to λ , while the motion of the arm to $1 - |\lambda|$. The coordinates of the platform can be easily expressed as Cartesian coordinates, so the coefficient λ can directly be applied to the element of the coordinates on y-axis, such that $r_0^d = r_0^{act} + \lambda \Delta T_y$. Regarding the arm, the control has been chosen to be made in the joint-space, so the aim here is to find the desired joint values. Once the coefficient to weight the motion along the y-axis has been computed, a coefficient matrix can be defined, such that:

$$\Lambda = \begin{bmatrix} \lambda_x & 0 & 0 \\ 0 & \lambda_y & 0 \\ 0 & 0 & \lambda_z \end{bmatrix}, \quad (5)$$

Where λ_i with $i = x, y$ or z , represents the weighting coefficient for the i -axis. Since the next step is to compute the inverse kinematics model of the arm regarding the desired pose, the coefficient in the matrix must be chosen from the point of view of the arm motion. So basically, $\lambda_y = 1 - |\lambda|$. Then, the desired position can be re-evaluated taken into account those coefficients, in such a way that:

$$P_{EE}^{nd} = \Lambda P_{EE}^d. \quad (6)$$

With this new desired position, the joint-space coordinates of the robotic arm can be computed using the inverse kinematics model:

$$q^d = k_i(X_{EE}^{nd}). \quad (7)$$

Finally, the desired position of the mobile support r_0^d and the desired joint coordinates of the arm q^d being known, the control can be computed and sent to the system (KHALIL & DOMBRE, 1999).

3 Results and discussion

The tests have been conducted on the system shown in **Fig. 1**. They consist in moving the system according to the detection of a plant, so that the camera is centred above its barycentre. The orientation of the camera is constrained such that the camera is facing the ground and that the wrist of the arm is directed outward. In our case, where there is only one redundancy along the y-axis, the different coefficients of the Λ matrix and the parameters of the function $\lambda(e_y)$ are defined such that $\lambda_x = 1, \lambda_y = 1 - |\lambda|, \lambda_z = 1, \mu = 4.0, \eta = 0.5$.

An image processing is implemented to provide the plant barycentre and also the radius of its circumscribed circle, by the use of thresholding. Assumptions made at that point are that there is only one plant to be detected in the camera field, and that the ground is not green.

Fig. 3 to 5 correspond to a test where the system is firstly set in an initial position, and the plant is positioned outside the arm workspace. They show the Cartesian velocities of the end-effector in the arm base frame (**Fig. 3**), the velocity of the axis (**Fig. 4**) and the value of λ (**Fig. 5**). As it can be seen in the latter, the motion can be divided into three parts: the first one between 5 and 10 s., where λ is almost equals to 1, then between 10 and 15 s. is the transition of the value of λ , and last, after 15 s., where λ is almost 0.

During the first part, **Fig. 3** shows that there is almost no motion of the end-effector along the y-axis, its velocity along that axis is represented by the black solid line, and at the same time, the linear axis moves at its maximum speed. That behaviour is consistent with λ being equal to 1. Also, the motion along the x-axis, whose velocity is represented by the black dotted line, is not impacted by the coefficient reducing the motion on the y-axis. Through the transition period, the axis speed decreases as the value of λ (**Fig. 4 & 5**). On the contrary, the linear velocity of the end-effector on the y-axis is increasing. Finally, as λ is null, only the arm is moving, and its speed slowly decreases until the arm stands still above the plant.

Results presented above shows that this weighting coefficient matrix permits the distribution of the motion onto both parts of the system, depending on the position of the goal to reach. It also allows avoiding disturbances caused by the motion of the mobile base on the gantry, by limiting its motion only if necessary. At the end of this movement, the arm is centred above the plant and in its workspace along the y-axis. An execution of a trajectory changing the orientation of the camera is then allowed, to observe the plant from different points of view.

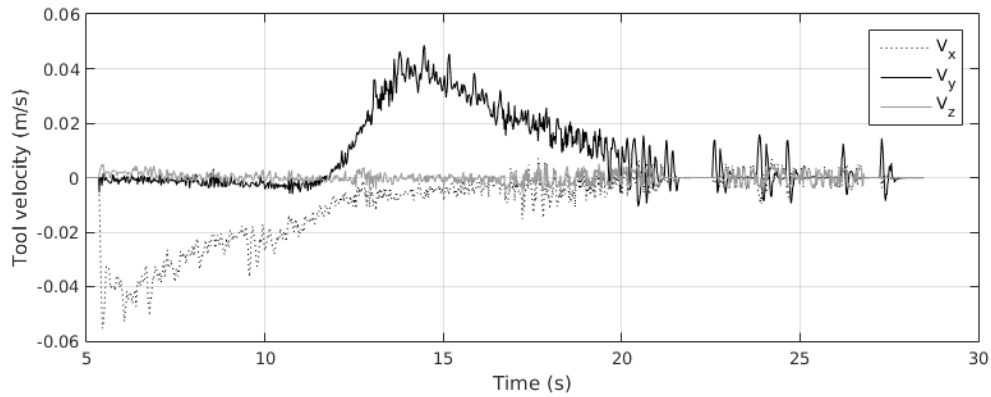


Figure 3: End-effector velocity

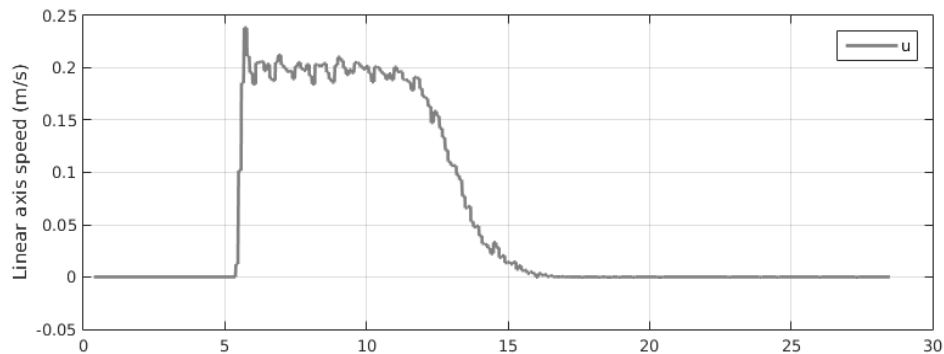


Figure 4: Linear axis velocity

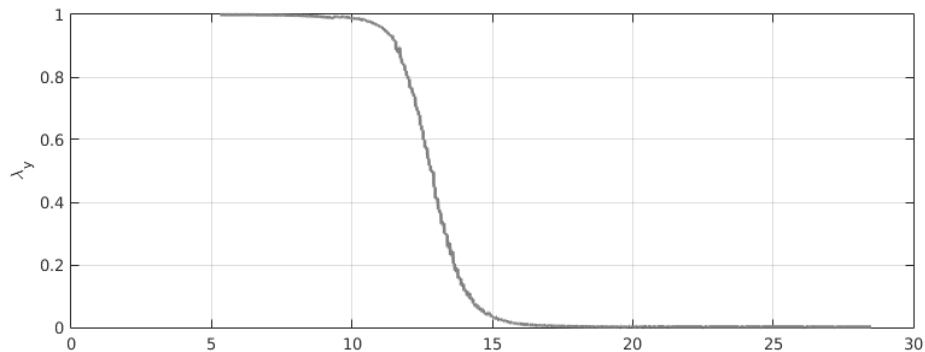


Figure 5: Lambda value

Moreover, this method does not impact the motion along the other axis and can be adapted to systems with higher redundancy degrees.

4 Conclusion

The work presented in this paper allows controlling a mobile manipulator to acquire data in open field to analyse the plants and detect potential anomalies, by providing a way to manage redundancies. Our contribution was experimented on a system composed of a 6-dof robotic arm and a gantry, but the method presented here can be adapted to a system with additional redundancies, since coefficients on x and z-axis can be added. For further works, experiments in actual conditions have to be conducted. Also, an image

quality assessment can be added to the image processing to find the best view to retrieve relevant information.

Acknowledgement

The authors acknowledge the support received from the French Ministry of Agriculture through the program CASDAR in the framework of Phénaufol project. This research is also supported by the Region Auvergne-Rhône-Alpes.

References

- BAYLE B, FOURQUET JY, RENAUD M (2003):** Manipulability of wheeled mobile manipulators: Application to motion generation. *The International Journal of Robotics Research* 22(7-8): 565-581.
- BLACKMORE S (2016):** Towards robotic agriculture. *Autonomous Air and Ground Sensing Systems for Agricultural Optimization and Phenotyping* 9866: 986603.
- BROCK O, PARK J, TOUSSAINT M (2016):** Mobility and Manipulation. *Springer Handbook of Robotics*. s.l.:Springer: 1007-1036.
- EGERSTEDT M, HU X (2000):** Coordinated trajectory following for mobile manipulation. *Proceedings IEEE International Conference on Robotics and Automation 2000/ICRA'00, Volume 4: 3479-3484.*
- FRUCHARD M, MORIN P, SAMSON C (2006):** A framework for the control of nonholonomic mobile manipulators. *The International Journal of Robotics Research* 25(8): 745-780.
- KHALIL W, DOMBRE E (1999):** Modélisation, identification et commande des robots. s.l.:Hermès.
- LIEBISCH F, KIRCHGESSNER N, SCHNEIDER D, WALTER A, HUND A (2015):** Remote, aerial phenotyping of maize traits with a mobile multi-sensor approach. *Plant methods* 11(1): 9.
- MADSEN O, BOGH S, SCHOU C, ANDERSEN RS, DAMGAARD JS, PDERSEN MR, KRÜGER V (2015):** Integration of mobile manipulators in an industrial production. *Industrial Robot: An International Journal* 42(1): 11-18.
- MAHLEIN AK (2016):** Plant disease detection by imaging sensors-parallels and specific demands for precision agriculture and plant phenotyping. *Plant Disease* 100(2): 241-251.
- MANN MP, ZION B, RUBINSTEIN D, LINKER R, SHMULEVICH I (2014):** Minimum time kinematic motions of a cartesian mobile manipulator for a fruit harvesting robot. *Journal of Dynamic Systems, Measurement, and Control* 136(5): 051009.
- OGREN P, PETERSSON L, EGERSTEDT M, HU X (2000):** Reactive mobile manipulation using dynamic trajectory tracking: design and implementation. *Proceedings of the 39th IEEE Conference on Decision and Control, 2000, Volume 3: 3001-3006.*
- YAMAMOTO Y, YUN X (1994):** Coordinating locomotion and manipulation of a mobile manipulator. *IEEE Transactions on Automatic Control* 39(6): 1326-1332.
- YOSHIKAWA T (1985):** Manipulability of robotic mechanisms. *The international journal of Robotics Research* 4(2): 3-9.

Kinematic Positioning in a Real Time Robotic Total Station Network System

Gabriel Kerekes, Volker Schwieger

*Institute of Engineering Geodesy, University of Stuttgart, Geschwister-Scholl-Str. 24D, Germany
E-mail: gabriel.kerekes@iigs.uni-stuttgart.de*

Abstract: A network comprised of Robotic Total Stations allows the continuous tracking of a moving reflector even if obstructions interfere with the line-of-sight. The following paper presents a real time network system that connects two instruments, the Leica TS30 and TS16, which communicate with a central computer while tracking a moving 360° reflector. These are positioned in the same coordinate frame and track the reflector in a synchronized manner. If the line-of-sight of one instrument is interrupted, the total station switches into a passive state and will continue to “blindly” track the reflector until a new line-of-sight is reestablished. To verify the system’s performance, two different scenarios are shown. In the first case, a reflector is fixed on a calibration rail and is travelling with constant speed. The second case analyzes an irregular movement described by a moving person. In each scenario, obstacles interrupt the line-of-sight in a controlled or random manner. The outcomes put a light on the achieved positioning quality and the tracking process while obstructions occur.

Key words: Robotic total station network, synchronized measurement, target tracking

1 Introduction

Robotic Total Stations (RTS) are used for a wide range of tracking, positioning and classical surveying applications due to their capability of precisely measuring angles and distances. The most important prerequisite is a continuous line-of-sight between reflector and instrument that is not allowed to be interrupted during the tracking processes. Since continuity rarely occurs on fast changing environments like construction sites, the alternative of a RTS network system can overcome these drawbacks.

For more than 25 years RTS have been available on the market and for about 20 years they have been used for kinematic applications like machine control and guidance (STEMPFHUBER & INGENSAND, 2008). Recently developed instruments overcome many issues regarding tracking speed with the help of hardware improvements like piezo or magnetic motors (MÖSER *et al.*, 2012). Other problems like the internal synchronization of the measurement data (SCHWIEGER *et al.*, 2010) are reduced to negligible dimensions. Aside from the reachable high positioning accuracy, these are some of the reasons why processes that demand such accuracies in real time use RTS, a fact that has also been proven by BEETZ (2012) in simulations.

According to the European GNSS Agency Marketing Report (GSA, 2017), GNSS based guiding systems have a high quota of implementation in machine guidance, but for many purposes the accuracy is still not sufficient and the use of RTS remains the only solution. Experiments like those from SAMA & STOMBAUGH (2014) successfully made use of RTS to assess the accuracy of GNSS positioning systems in kinematic applications.

The idea of connecting and synchronizing total stations is not new, but currently there are only a few publications that handle this subject and the benefits of such systems remain on a theoretical level. MAO *et al.* (2013) developed a similar system, but there are no conclusions about system accuracy, reliability or its limitations.

Trying to fill this gap, the current paper briefly presents the RTS network system, illustrating the main concept of the system's architecture, determining and evaluating the position using adjustment theory and demonstrating its capabilities through two laboratory tests. Results show that even if one line-of-sight is interrupted, the kinematic measurement may continue, given that at least one RTS tracks the reflector.

2 System description

2.1 Concept

Having one RTS in a guidance system limits the positioning accuracy to the instrument's technical specifications and leads to a limited area of use. Multiple networked RTS (**Fig. 1**), on the other side, can enhance the accuracy through an optimal measurement configuration and assure a non-interrupted tracking process.

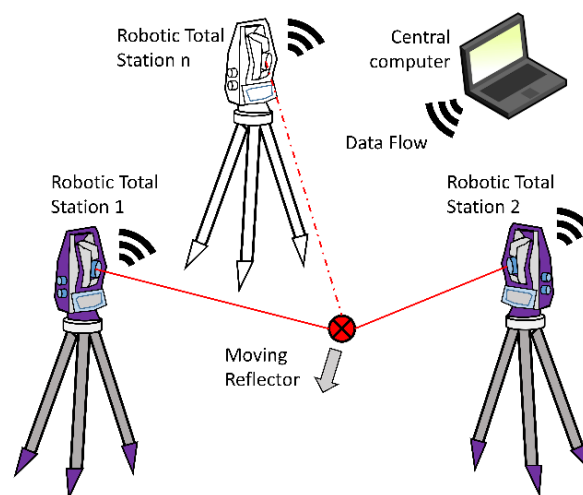


Figure 1: Robotic Total Station Network

A central computer, further referred to as server, facilitates the multidirectional data flow between each client (RTS) and itself. During the active tracking phase, the calculated position is stored and simultaneously made available for the other RTS. The two Leica RTS are connected with the server through a serial cable connection and use the Leica GeoCOM interface to communicate with the later described LabView software.

2.2 Software

The functional model can be summarised through the flowchart shown in **Fig. 2** and is implemented in the graphical programming software LabVIEW from National Instruments.

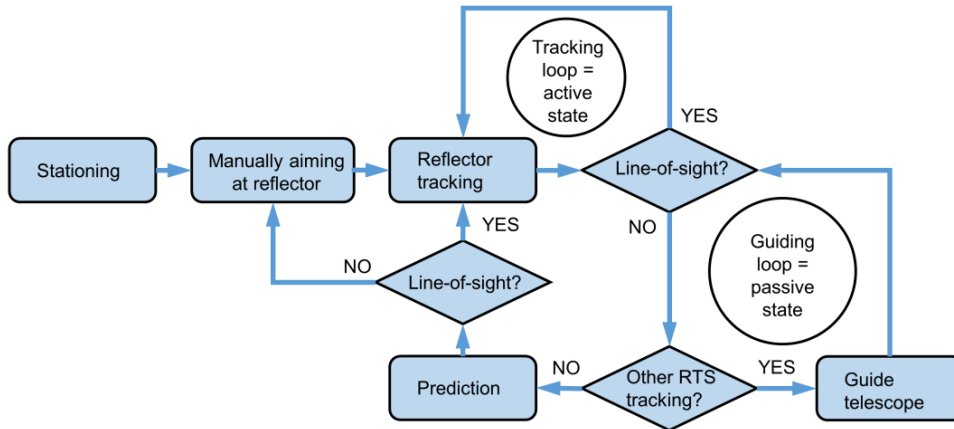


Figure 2: Flowchart of the real time robotic total station network software

After introducing the number of RTS or clients, the program will launch a control panel for each instrument with individual functions such as connection check, automatic free stationing, current reflector position and state of system. Although only two RTS were used for testing the system, an extension to more total stations is possible (LAATSCH, 2015).

In a first stage, a common coordinate reference network of points (local or global) must exist for the free stationing. Afterwards, the user has to manually aim at the later moving target. Instrument functions such as ATR (KLEEMAIER *et al.*, 2016) help to find the reflector and are further used during the tracking loop. The reflector positions are measured at a rate of 10 Hz and transferred into a depository based on the first in-first out principle (GEORGI & METIN, 2014). As a common reference for each position, a timestamp is allocated to the measured values. During the uninterrupted tracking process, the RTS is in the active state. If the line-of-sight is interrupted, the tracking stops and in that moment the program changes the RTS status to passive and checks the depository for a current available reflector position provided by another RTS. If this is available, the program transforms the absolute coordinates in polar coordinates and uses these angles to guide the RTS telescope towards the moving reflector until the obstruction does not interfere with the line-of-sight. In case that no position is available, prediction algorithms based on the reflector's last known positions and travelling speed are used to guide the telescope and search for the target. If one of these operations is successful and the reflector has been relocated, the active tracking loop is restarted. In case of failure, the user must manually aim at the reflector once more.

2.3 Scenario Tests

Basically, once the target has been locked, it can be fixed on any moving object. To restrict the possible spectrum of tests, two that resemble many applications have been chosen. The first one uses a carriage on which a reflector is fixed while moving on a rail. **Fig. 3** gives an overview of the conducted experiment and shows areas of the trajectory where both or only one RTS were in active or passive state respectively. Two reflectors, the Leica GRZ101 and GRZ4 360° prisms, were used in consecutive measurements to test the system's performance. For specific details about reflector properties and its influence on position, see LACKNER & LIENHART (2016). Measurements were also taken without obstructions and are used to illustrate the improved accuracy of this configuration. Any real construction machine describes a similar movement, namely travelling at low speeds and without sudden direction changes.

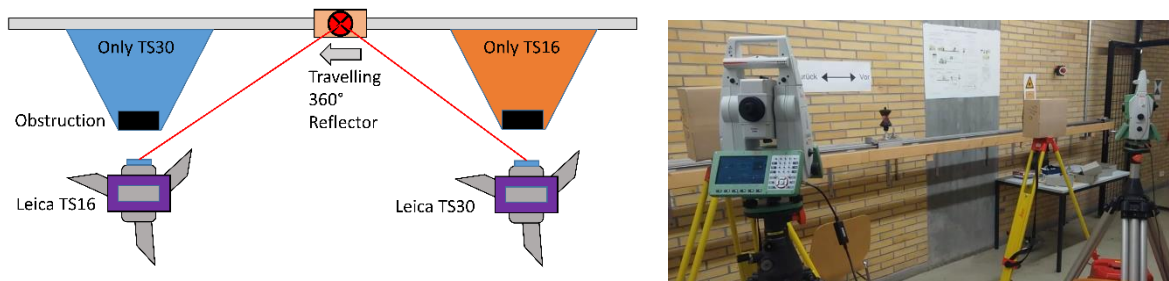


Figure 3: Overview of RTS Network in the first scenario

On the other side, if the system is used for kinematic applications that involve irregular movements or quick direction changes, like an operator carrying a reflector on a measurement pole or tracking and guiding of an UAV (MAXIM *et al.*, 2017), the reachable accuracy and reliability need to be evaluated. The second scenario includes variable speeds and interruption of the line-of-sight during a random walk.

3 Performance evaluation

Asserting the quality of a measurement in engineering geodesy can be done in multiple ways by either using reference values and calculating differences to have a measure for control or evaluating the precision by using standard deviations. The rail serves as line of reference having coordinates determined by a laser tracker (API Radian). Lateral deviations to this line are considered as quality indicators for the tracking process. Another way to evaluate the position is by individual standard deviations. These are determined either by law of propagation of variance (KAHMEN, 2006) if one RTS is available, or by a least square adjustment if two or more RTS are available.

3.1 Lateral deviation

In an ideal case, differences between the reference rail and RTS measurements should be zero, but because of random errors, differences occur and can be roughly defined

with the help of technical specifications. Both RTS are precision total stations and show an angle measurement accuracy of 0.3 mgon and 0.15 mgon, whereas the distance measurement accuracy in tracking mode is $\sqrt{(3\text{mm})^2 + (1\text{ppm})^2}$ (LEICA GEOSYSTEMS, 2018). During the measurement, it is possible to separate the measured data for each instrument and visualize the respective differences. **Fig. 4** presents the differences between the reference positions (zero) that were determined with the laser tracker and the two RTS measurements. Only the X-axis is taken as comparison because the rail is perpendicular to this coordinate direction.

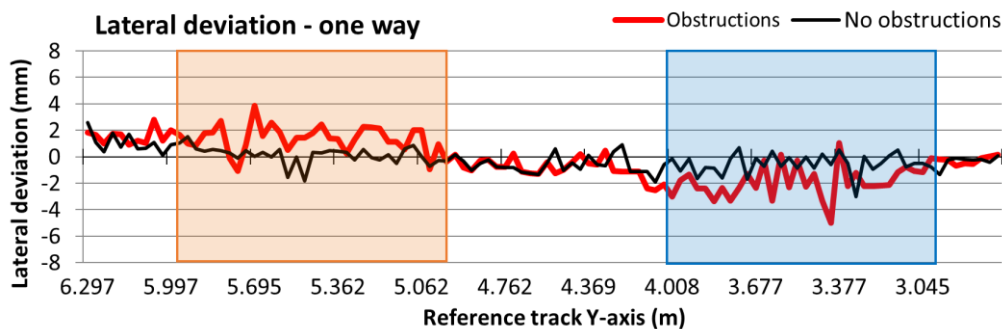


Figure 4: Lateral deviations in comparison with laser tracker measurements (zero reference)

It can be observed that the use of two RTS reduces the total deviation (middle) and offers improved position accuracy for the moving object. The current measurement setup is similar to theodolite measurement systems, often used in industrial measurement for high accuracy demanding tasks. Because of the high angle measurement accuracy, well-conditioned intersection angles lead to error minimization. This is why coordinates determined by intersection will have a better quality than those through polar point determination using one RTS only. If there are more than two RTS in the network, the best position is obtained by an adjustment.

3.2 Adjusted results

Having two directions, two distances and two zenith angles measured from two different station points, allowed the calculation of the point positions through a least square adjustment. Station points are considered reference points and the observed points are defined as new points having the timestamp as their name. One indicator for the positioning quality is the 3-dimensional Helmertian error of position (NIEMEIER, 2008).

The individual standard deviations are determined after an adjustment of the two RTS measurements and in case of line-of-sight interruption, law of propagation of variance is used to calculate the Helmertian error of position. **Fig. 5** presents the magnitude of these standard deviations in each case. These vary between 1.3 mm and 1.9 mm in case of no obstructions and from 1.3 mm to 4.8 mm with obstructions.

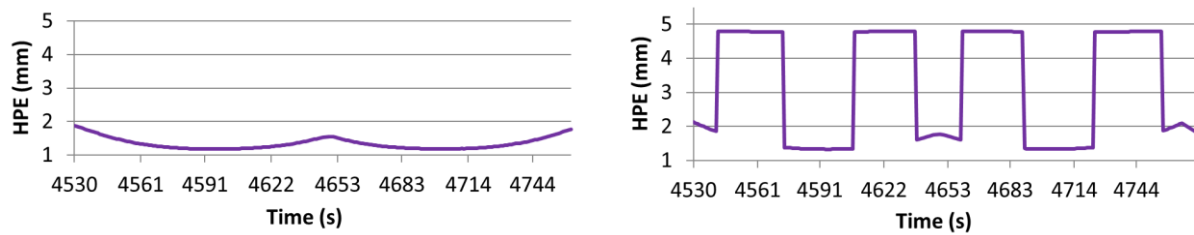


Figure 5: Helmertian error of position in a two way trip without obstructions (left) and with obstructions (right)

Another method of analyzing accuracy is with the help of confidence ellipsoids. After the aforementioned adjustment, the variance and covariance of each point coordinate are known and used to determine the size and orientation of the confidence ellipsoids. The smaller the semi-axes of the ellipsoids, the better the positioning quality. Ratio between semi-axes is also a quality indicator, and spheres (3D) or circles (2D) resemble a good conditioned measurement configuration. Orientation of the ellipsoids gives information about the distribution of the variances. These parameters are all dependent on network configuration and instrument measurement accuracy and will vary in shape according to the point distribution in space, like in the setup shown.

In the first scenario, when both RTS are tracking, semi-axes of the confidence ellipses (here 2D representation) have an average value of 2.6 mm and achieve a circle like the form in the middle of the rail (**Fig. 6** left). If only one instrument is tracking, semi-axes reach a maximum of 10.7 mm and ellipses are elongated as can be seen in **Fig. 6** right. In transition areas, semi-axes show jumps in magnitude of up to 7 mm.

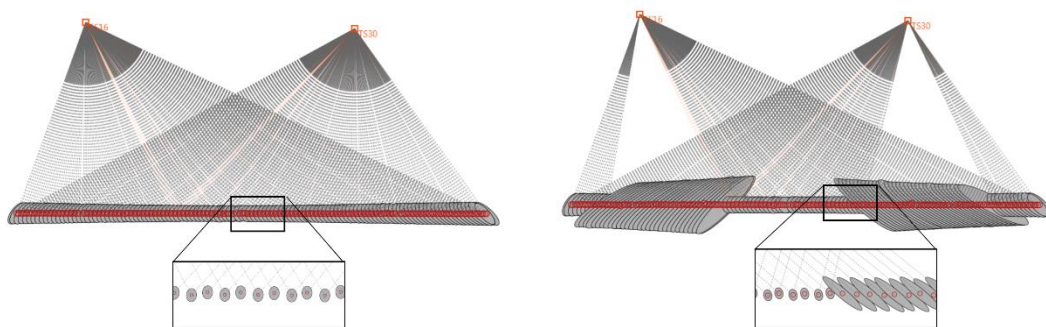


Figure 6: Confidence ellipses after network adjustment without obstructions left and with obstructions right (calculated and represented with JAG3D)

The second scenario involved reflector movements at variable speeds and lead to positioning errors that are larger than expected. The reflector position was apparently falsified by both RTS measurements. In the moment current research is undertaken to determine the cause of this problem and possible improvements. Another drawback in this case, is that prediction algorithms fail to correctly redirect a passive RTS if the last known positions do not represent a predictable movement, a fact that will be further discussed.

3.3 Reflector tracking speed

Tracking speed is constrained by two main hardware limitations; firstly the angle measurement frequency rate and the turning speed of the telescope. For the TS generation, a radial speed of up to 20 km/h at 1 km distance (KLEEMAIER *et al.*, 2016) is achievable. The currently presented system incorporates two RTS with different motorization technology. The TS30 can rotate with a speed of up to 200 gon/s, whereas the TS16 has a maximum rotation speed of 50 gon/s and restricts the RTS Network System to this limit. At a constant range of 5 m this means a maximum linear speed of ca. 14 km/h and at 30 m of ca. 85 km/h, and increasing linearly up to a certain range limited by the ATR function and distance measurement unit (GRIMM *et al.*, 2015).

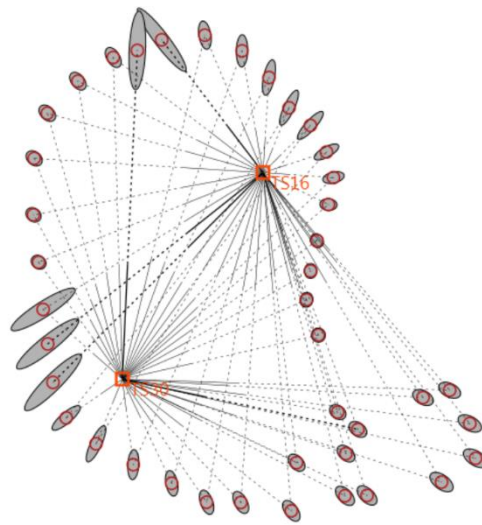


Figure 7: Confidence ellipses for random walk

Another aspect that is notable during the “blind” tracking is that after losing sight of the reflector, the software changes the status of that RTS to passive and starts sending commands that direct the telescope towards the predicted position of the target. This takes time and currently, for each necessary angular increment and telescope turn, between 1 up to 1.5 s are elapsed. To overcome this dead time a Kalman-Filter is implemented that uses the last 20 reflector positions (epochs) to determine the future position of the reflector. Depending on the application, this number can be adapted. One reason for using this is that the prediction bypasses the RTS serial connection problem of handling and executing one command at a time, thus compensating for the dead times necessary to process commands.

4 Conclusions and perspectives

Using a network of RTS for tracking and guiding in kinematic applications leads to continuous tracking of a moving object, even in case of a line-of-sight interruption. The tests showed that while both RTS were tracking, the Helmertian error of position for controlled motion did not exceed 2 mm. If only one RTS was active, this error rose up to almost 5 mm, but the tracking processes still continued. This becomes especially im-

portant when a construction machine like an asphalt paver depends on RTS measurements for guidance. Another advantage of the presented system is that a larger number of RTS that are well distributed in the area of interest offer a better positioning availability, as seen in the experiment with obstructions, and lead to high data redundancy.

The Achilles' heel of the currently presented system was discovered through the second scenario where rapid and irregular reflector movements eventually stopped the continuous tracking process and lead to position falsification. To overcome and improve some issues, perspective experiments foresee a larger number of RTS in the network and the possibility of adding total stations from other manufacturers to the network. Another possible improvement is reducing the reaction time of the "blind" RTS and the usage of image information in the target identification process (ERHART & LIENHART, 2017). Such enhancements may lead to a more frequent use of real time robotic total stations network, not only in machine guidance and control, but also other applications that require high positioning accuracy in real time.

References

- BEETZ A (2012):** Ein modulares Simulationskonzept zur Evaluierung von Positionssensoren sowie Filter- und Regelalgorithmen am Beispiel des automatisierten Straßenbaus. PhD Thesis, Munich, DGK 2012.
- ERHART M, LIENHART W (2017):** Object tracking with robotic total stations: Current technologies and improvements based on image data. *Journal of Applied Geodesy* 11(3): 131–142.
- GEORGI W, METIN E (2007):** Einführung in LabVIEW 3. Auflage. Carl Hanser Verlag, Munich.
- GRIMM D, KLEEMAIER G, ZOGG HM (2015):** ATR Plus Whitepaper. Leica Geosystems AG.
- GSA –EUROPEAN GNSS AGENCY (2017):** GNSS Market Report, Issue 5, copyright © European GNSS Agency. Retrieved from: <https://www.gsa.europa.eu/>, last accessed on 02.06.2018.
- KAHMEN H (2006):** Angewandte Geodäsie: Vermessungskunde. 20. Auflage. Walter de Gruyter, Berlin.
- KLEEMAIER G, MAAR H, ZOGG HM (2016):** Enhanced automation performance of Total Stations for kinematic applications using the ATRplus technology. 5th International Conference on Machine Control & Guidance, Vichy, France, 2016.
- LAATSCH S (2015):** Vernetzung zweier Tachymeter zur automatischen Zielverfolgung. Diploma thesis, University of Stuttgart, not published.
- LACKNER S, LIENHART W (2016):** Impact of Prism Type and Prism Orientation on the Accuracy of Automated Total Station Measurements. Proceedings on Joint International Symposium on Deformation Monitoring, Vienna, Austria, 2016.
- LEICA GEOSYSTEMS AG (2009):** Leica Viva TS16 Data Sheet, Leica Viva TS30 Data Sheet, 2009, 2015. Retrieved from <https://leica-geosystems.com>, last accessed on 02.06.2018.
- MAO S, LU M, SHEN X, HERMANN U (2013):** Multi-point Concurrent Tracking and surveying in construction field. 30th International Symposium on Automation and Robotics in Construction, Montreal, Canada, 2013.
- MAXIM A, LERKE O, PRADO M, DÖRSTELMANN M, MENGES A, SCHWIEGER V (2017):** UAV Guidance with Robotic Total Station for Architectural Fabrication Processes. 156th DVW-Seminar, Unmanned Aerial Vehicles, Stuttgart, Germany, 2017.

- MÖSER M, HOFFMEISTER H, MÜLLER G, STAIGER R, SCHLEMMER H, WANNINGER L (2012):** Handbuch Ingenieurgeodäsie: Grundlagen. Wichmann, Berlin.
- NIEMEIER W (2008):** Ausgleichungsrechnung 2. Auflage. Walter de Gruyter, New York.
- SAMA MP, STOMBAUGH TS (2014):** Performance Evaluation of a Tracking Total Station as a Position Reference for Dynamic GNSS Accuracy Testing. *Applied Engineering in Agriculture* 30(4): 557-563.
- SCHWIEGER V, BEETZ A, WENGERT M, SCHWEITZER J (2010):** Echtzeit-Integration ingenieurgeodätischer Messsysteme in Bauregelkreise. 16. Internationaler Ingenieurvermessungskurs. Munich, Germany 2010.
- STEMPFHUBER W, INGENSAND H (2008):** Baumaschinenführung und -steuerung – Von der statischen zur kinematischen Absteckung. ZfV: 36-44.

In-field position accuracy at the millimetre level using a total station: Validation using an industrial robotic arm

Dimitris S. Paraforos¹, Marcus Reutemann², Galibjon Sharipov¹,
Roland Werner², Hans W. Griepentrog¹

¹University of Hohenheim, Institute of Agricultural Engineering, Technology in Crop Production, Garbenstr. 9, D-70599, Stuttgart, Germany

²John Deere GmbH & Co. KG, Intelligent Solutions Group, Advanced Engineering, Straßburger Allee 3, D-67657 Kaiserslautern, Germany
E-mail: d.paraforos@uni-hohenheim.de, tel.: +49 711 459 24556

Abstract: For agricultural tasks related to precision farming, accurate in-field positioning is a necessity. Although the accuracy of some centimetres that the real time kinematic-global navigation satellite system (RTK-GNSS) can provide is adequate for many applications, the demand for higher in-field accuracy at a millimetre level is increasing. A device that is gaining a lot of attention for its increased accuracy is the robotic total station (TS). Aiming at using the TS under realistic conditions for dynamic in-field positioning, its accuracy was assessed utilising an industrial robotic arm. Straight AB lines but also U-turn and Pattern-8 experiments were performed. The horizontal and vertical relative cross-track error (XTE) between the TS and the robotic arm data was calculated for various speeds and for two different positions of the TS. From the results, it was evident that as the speed increased so did the horizontal relative XTE. Changing the position of the TS from in line to perpendicular, in respect to the direction of motion, proved to result in a higher accuracy. The maximum mean horizontal relative XTE value of all experiments was 4.01 mm for Pattern-8, which also had the maximum value for the 95th percentile, i.e. 12.86 mm.

Key words: 3D positioning; cross-track error; in-field accuracy; robotic arm; total station

1 Introduction

Over the last decades, the use of real time kinematic-global navigation satellite system (RTK-GNSS), which offers position accuracy at the centimetre level, has widely expanded introducing new possibilities to agricultural applications. Nevertheless, there has been always a demand for even more accurate in-field positioning at the millimetre level. The RTK-GNSS is not accurate enough, especially in the vertical direction. This level of accuracy is necessary when aiming to increase the level of automation in agricultural tasks. An example is the area of plant phenotyping using autonomous vehicles (RUCKELSHAUSEN *et al.*, 2009), where data fusion from various sensors are used to create a three-dimensional (3D) reconstruction of crop plants. Although vision systems have been developed aiming to provide such a high accuracy by fusing information from

different images, usually a positioning system is utilised to georeference the acquired images (ROSE *et al.*, 2016).

A device with a higher accuracy than the RTK-GNSS is the total station (TS), which could be utilised to provide position data when this level of accuracy is demanded. Commonly, this device is used in the domain of civil engineering and provides a higher accuracy compared to satellite-based positioning systems.

The use of a TS for accurate 3D positioning related to agricultural applications is increasing the last years. This can be seen from the research papers that are being published and utilise TSs for ground-truth (VOUGIOUKAS *et al.*, 2016; VROEGINDEWEIJ *et al.*, 2016). An important issue regarding data synchronisation when assessing the GNSS with a TS has also been discussed by SAMA *et al.* (2013) and a hardware method for time-stamping these asynchronous data was introduced.

The question that arises is if the TS can replace the GNSS for accurate in-field 3D dynamic positioning. In a research by PARAFOROS *et al.* (2015) the TS was utilised to assess in-field positioning provided by RTK-GNSS and inertial measurement unit (IMU) fused data. It was concluded that the TS could also be used for carrying out precision agriculture-related applications that require high accuracy. Nevertheless, this high accuracy of the TS needs to be determined and quantified under realistic conditions.

The aim of the paper is to assess the 3D accuracy of a TS from an agricultural-related perspective, in order to be used for dynamic in-field positioning when sub-centimetre accuracy is required, but also when a satellite-based solution is not available due to reflection or shading errors caused by high trees or buildings. The novelty of the presented methodology lies in the fact that it examines the accuracy of the TS measurements under dynamic and realistic outdoor conditions, compared to indoor laboratory environment like previous studies (KIRSCHNER & STEMPFHUBER, 2008). Furthermore, except straight AB lines, other patterns are examined, i.e. U-turn and Pattern-8, which are usually followed when performing in-field agricultural-related tasks.

2 Materials and Methods

A Trimble SPS930 (Trimble, Sunnyvale, USA) universal TS was used to track a Trimble MT900 prism, which was mounted on the end effector of a TX200L robotic arm (Stäubli International AG, Pfäffikon, Switzerland) (**Fig. 1**). The specific robotic arm is placed on the rooftop of the John Deere European Technology Innovation Centre (Kaiserslautern, Germany).



Figure 1: The total station that was used to track a prism on a robotic arm (photo: John Deere GmbH & Co. KG, Intelligent Solutions Group, Advanced Engineering, modified).

2.1 Performed experiments

The experimental design is presented in **Fig. 2**. An AB line was performed with three different speeds, i.e. 50 mm s^{-1} , 200 mm s^{-1} , and 500 mm s^{-1} . For these measurements, the TS was placed in the same line as the AB line (**Fig. 2a**). The AB line with a speed of 500 mm s^{-1} was repeated but this time the TS was placed perpendicular to the AB line (**Fig. 2b**). Without moving the TS, the speed of the robotic arm was increased to 1000 mm s^{-1} and, both a U-turn and a Pattern-8 experiment were performed as can be seen in **Fig. 2c**, and d, respectively.

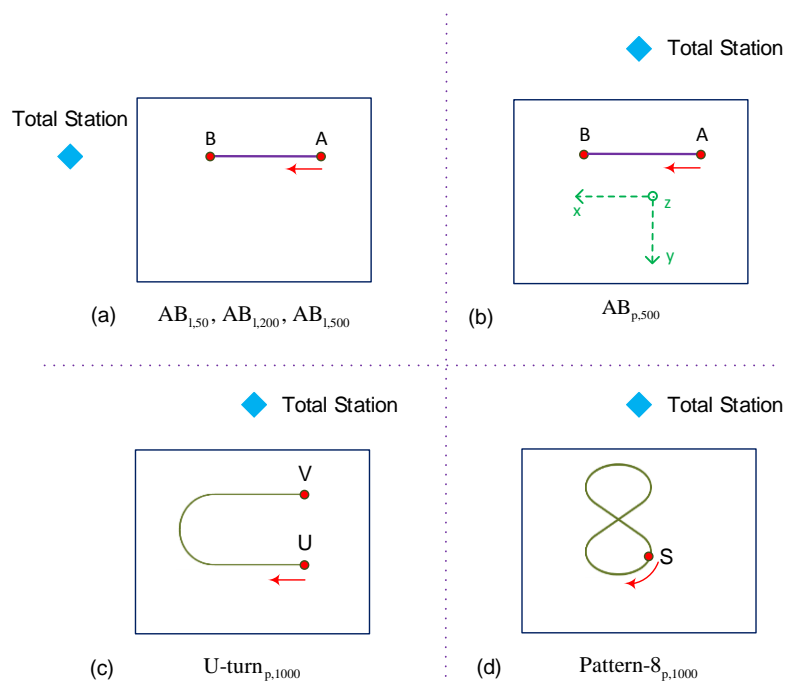


Figure 2: Performed experiments: (a) AB line with 50 mm s^{-1} , 200 mm s^{-1} , and 500 mm s^{-1} and the TS placed in the same line, (b) AB line with 500 mm s^{-1} and the TS placed perpendicular to the AB line, (c) U-turn with 1000 mm s^{-1} , and (d) Pattern-8 with 1000 mm s^{-1} . The red arrows indicate the starting point and direction of each experiment.

The red arrows in **Fig. 2** indicate the starting point and direction of each measurement. The coordinate frame of the robotic arm $O(x,y,z)$ (**Fig. 2b**) indicates the origin and the direction of the positive values of the three axes (the z axis was pointing upwards), and was the same for all performed experiments. The data acquisition software of the robotic arm was configured to provide the position data of the same point where the prism was attached on.

The Trimble SCS900 Site Controller software, running on a Trimble Yuma 2 tablet computer, was used to acquire and store data from the TS. In order to have all measurements of the TS in the same coordinate frame (robotic arm frame), independently of its position, the TS was stationed using the known coordinates of the points A and B. By placing the prism at these points and by inserting the corresponding x , y , and z values of the robotic arm to the SCS900 software of the TS, a rigid transformation was performed that transformed all subsequent measured points by the TS, to the O frame. The 3D position data were transmitted from the TS as long as the current measurement varied at least by 1 mm from the previous one but with a maximum frequency of 20 Hz.

2.2 Accuracy assessment

The relative cross-track error (XTE) was chosen as an accuracy assessment criterion for the TS data, as it is a common method for assessing positioning systems (EASTERLY *et al.*, 2010) and takes into consideration the measured points of the assessing device. The geometrical representation of the relative XTE is presented in **Fig. 3**. The XTE is the horizontal distance d between any measured position of the prism $p_j^t = (x_j^t, y_j^t)$ ($j=1, \dots, k$) and the specific path of the recorded robotic arm end effector $p_i^r = (x_i^r, y_i^r)$ ($i=1, \dots, \xi$), where k and ξ is the total number of measured points for the prism and the robotic arm, respectively.

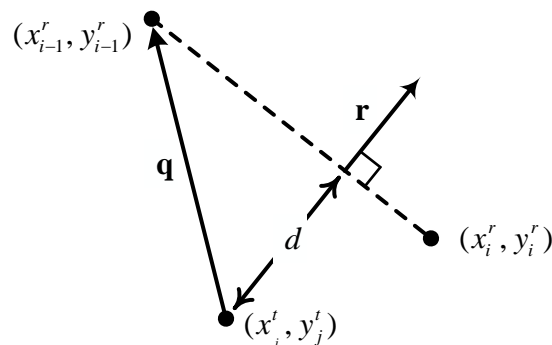


Figure 3: Geometrical representation for calculating the 2D distance of the measured by the TS prism positions $p_j^t = (x_j^t, y_j^t)$ from a line connecting the two reference points $p_{i-1}^r = (x_{i-1}^r, y_{i-1}^r)$ and $p_i^r = (x_i^r, y_i^r)$ as they were provided by the robotic arm.

In order to find the relative XTE for all measured data, a heuristic algorithm was developed, which for each measured prism point p_j^t calculated the distance to all points of the robotic arm that belonged to the same path. Subsequently, the two robotic arm points with the smallest distance to p_j^t were chosen as p_{i-1}^r and p_i^r , to find the relative XTE. In order to find the horizontal relative XTE in the xy -plane, the procedure was as described above but for the vertical relative XTE in the xz -plane, all values of the y axis were replaced with the corresponding values of the z axis.

The vector \mathbf{r} that is perpendicular to the line connecting the two reference points p_{i-1}^r and p_i^r is calculated by

$$\mathbf{r} = \begin{bmatrix} y_i^r - y_{i-1}^r \\ -(x_i^r - x_{i-1}^r) \end{bmatrix}.$$

Considering a vector \mathbf{q} from the prism position p_j^t to the first robotic arm point p_{i-1}^r defined by

$$\mathbf{q} = \begin{bmatrix} x_{i-1}^r - x_j^t \\ y_{i-1}^r - y_j^t \end{bmatrix},$$

then the relative XTE is equal to the distance d , which is given by projecting \mathbf{q} onto \mathbf{r} provided by

$$d = |\text{proj}_{\mathbf{r}} \mathbf{q}| = |\hat{\mathbf{r}} \cdot \mathbf{q}| = \frac{|\mathbf{r} \cdot \mathbf{q}|}{|\mathbf{r}|} = \frac{|(x_{i-1}^r - x_j^t)(y_i^r - y_{i-1}^r) - (x_i^r - x_{i-1}^r)(y_{i-1}^r - y_j^t)|}{\sqrt{(x_i^r - x_{i-1}^r)^2 + (y_i^r - y_{i-1}^r)^2}}, \quad (1)$$

where $\hat{\mathbf{r}}$ is the unit vector in the direction of \mathbf{r} .

3 Results and Discussion

3.1 AB lines

The boxplots for $AB_{1,50}$, $AB_{1,200}$, $AB_{1,500}$, and $AB_{p,500}$ relative XTE are presented in **Fig. 4**. For the $AB_{1,50}$ experiment as the for the $AB_{1,200}$, the whiskers of the horizontal and vertical relative XTE did not exceed 2 mm, and 3 mm, respectively, except for some outliers that can be seen in the vertical XTE. It is evident that the speed increase from 50 mm s^{-1} to 200 mm s^{-1} did not significantly affect the accuracy of the TS. The former had a slightly better accuracy compared to the latter. For $AB_{1,500}$ experiments, the whiskers of the horizontal relative XTE had a maximum value of around 3 mm with $AB_{p,500}$ having a slightly better performance. Nevertheless, for the $AB_{p,500}$ a high number of outliers is present, reaching up to 16 mm (not illustrated for better comparison of results).

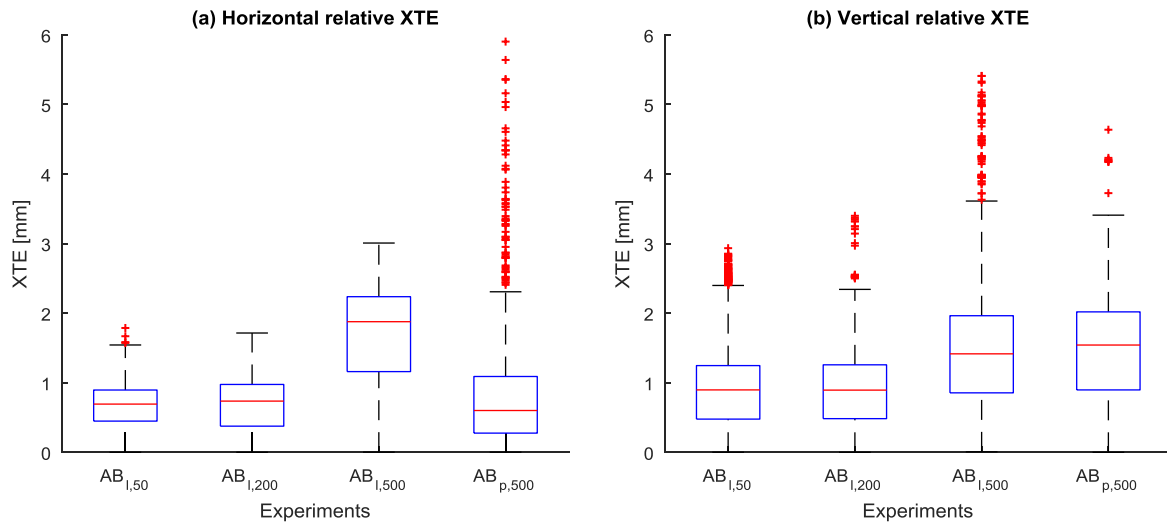


Figure 4: Boxplots for (a) horizontal and (b) vertical relative XTE for the AB lines. The outliers are also presented with red crosses.

3.2 U-turn and Pattern-8

The acquired data from the TS and the robotic arm from the U-turn and Pattern-8 experiment are illustrated in **Fig. 5a** and **b**, respectively. Even from these illustrations, it is obvious that the vertical absolute deviation of the TS from the end effector did not exceed one centimetre since the entire length of the z-axes of **Fig. 5a** and **b** is 10 mm. Nevertheless, a difference of the TS data compared to the robotic arm data is easily noticeable and specifically for the Pattern-8 experiment, where a higher error can be noticed at the turning sections compared to the straight parts.

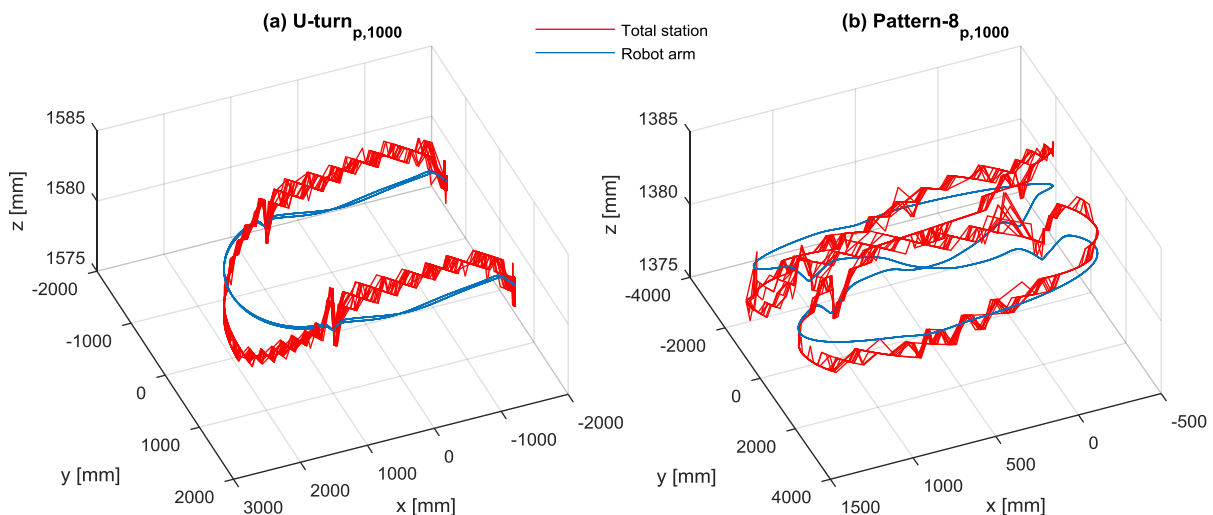


Figure 5: (a) U-turn and (b) Pattern-8 position data from the TS (red) and the robotic arm (blue).

3.3 Comparison of all experiments

In **Table 1**, the summary statistics for the horizontal and vertical relative XTE for all performed experiments are presented. It is evident that when the speed was increased, the horizontal and vertical relative XTE also increased. A big difference can be seen between the U-turn and Pattern-8 experiments. Even though these two experiments were performed with the same speed, and without moving the TS, the latter had a larger mean horizontal relative XTE by 92%, while the standard deviation and the 95th percentile were larger by 313% and 199%, respectively. This was because the Pattern-8 experiment had a bigger part of the route with turning sections than the U-turn experiment, resulting in a higher error. Regarding the vertical relative XTE, the increase in mean, standard deviation, and 95th percentile for these two experiments was smaller, up to 5%, 10%, and 12%, respectively.

Table 1: XTE error for all performed experiments.

Experiment	Horizontal relative XTE [mm]			Vertical relative XTE [mm]		
	Mean	St. dev.	95th perc.	Mean	St. dev.	95th perc.
AB _{i,50}	0.67	0.31	1.16	0.92	0.57	1.99
AB _{i,200}	0.69	0.37	1.24	0.89	0.51	1.72
AB _{i,500}	1.70	0.65	2.53	1.51	0.89	2.99
AB _{p,500}	0.86	1.21	2.06	1.46	0.74	2.54
U-turn _{p,1000}	2.09	1.24	4.30	1.65	0.90	3.00
Pattern-8 _{p,1000}	4.01	5.12	12.86	1.73	0.99	3.35

4 Conclusions

From the performed experiments, the resulted accuracy of the TS is very promising in replacing the RTK-GNSS where a sub-centimetre accuracy of the 3D dynamic position is required. The mean value of the relative XTE for all experiments had a maximum value of 4.01 mm. The only experiment where the relative XTE exceeded the sub-centimetre level was for Pattern-8 with a value of 12.86 mm for the 95th percentile of the measurements. Of course, this is an extreme case of in-field movement compared to most of the normal agricultural tasks. Finally, changing the position of the total station, from in-line to perpendicular to the direction of the prism movement, improved the horizontal accuracy of the provided information.

References

- EASTERLY DR, ADAMCHUK VI, KOCHER MF, HOY RM (2010):** Using a vision sensor system for performance testing of satellite-based tractor auto-guidance. *Comput. Electron. Agric.* 72: 107–118. doi:10.1016/j.compag.2010.03.004.
- KIRSCHNER H, STEMPFHUBER W (2008):** The Kinematic Potential of Modern Tracking Total Stations - A State of the Art Report on the Leica TPS1200+. 1st International Conference on Machine Control & Guidance: 51–60.
- PARAFOROS DS, GRIEPENTROG HW, GEIPEL J, STEHLE T (2015):** Fused inertial measurement unit and real time kinematic-global navigation satellite system data assessment based on robotic total station information for in-field dynamic positioning. STAFFORD JV (Ed.): *Precision Agriculture '15*: 275–282. doi:10.3920/978-90-8686-814-8_33.
- ROSE J, KICHERER A, WIELAND M, KLINGBEIL L, TÖPFER R, KUHLMANN H (2016):** Towards Automated Large-Scale 3D Phenotyping of Vineyards under Field Conditions. *Sensors* 16: 2136. doi:10.3390/s16122136.
- RUCKELSHAUSEN A, BIBER P, DORNA M, GREMMES H, KLOSE R, LINZ A, RAHE R, RESCH R, THIEL M, TRAUTZ D, WEISS U (2009):** BoniRob: An autonomous field robot platform for individual plant phenotyping. *Precision Agriculture 2009 - Papers Presented at the 7th European Conference on Precision Agriculture, ECPA 2009*.
- SAMA MP, STOMBAUGH TS, LUMPP JE (2013):** A hardware method for time-stamping asynchronous serial data streams relative to GNSS time. *Comput. Electron. Agric.* 97: 56–60. doi:10.1016/j.compag.2013.07.003.
- VOUGIOUKAS SG, HE L, ARIKAPUDI R (2016):** Orchard worker localisation relative to a vehicle using radio ranging and trilateration. *Biosyst. Eng.* 147: 1–16. doi:10.1016/j.biosystemseng.2016.03.006.
- VROEGINDEWEIJ BA, IJSSELMUIDEN J, VAN HENTEN EJ (2016):** Probabilistic localisation in repetitive environments: Estimating a robot's position in an aviary poultry house. *Comput. Electron. Agric.* 124: 303–317. doi:10.1016/j.compag.2016.04.019.

Representation Learning for Segment Matching for Future Applications in Relative Positioning of Machinery

Julian Schmiemann, Jan Schattenberg, Ludger Frerichs

*Technische Universität Braunschweig, Institute of mobile Machines and Commercial Vehicles,
Germany*

E-mail: julian.schmiemann@tu-braunschweig.de

Abstract: In this work we investigate the possibility to use state of the art approaches for deep learning on point clouds for matching segments, sensed from objects under varying perspectives, with the aim to obtain positional information for relative positioning. Therefore we propose a method and evaluate it using a custom real world data set.

Key words: Multi Agent 6DOF SLAM, Relative Positioning in GNSS-degraded Terrain, Automated Machine Cooperation, Deep Learning on Point Sets, Segment Matching, Representation Learning

1 Introduction

Relative Positioning is one of the key challenges when it comes to automation of cooperative machinery e.g. within agricultural processes. Nowadays most types of applications are relying on satellite navigation solely. This is feasible since large scale machinery is used, but developing of techniques for relative positioning using environmental sensors only, has had a rising upwind within the past few years, due to multiple reasons.

Lot of researchers nowadays are developing novel concepts for machinery of the future. Many of them feeling quite confident thinking of many small fully automated machines, which achieve comparable performance – with respect e.g. to area output – by teaming up (MINBEN *et al.*, 2017). Due to economic reasons, development of such systems is strongly coupled with developing novel sensor concepts, since GNSS systems, which are capable of achieving accuracy within few centimeter range, may account for a large share of the total cost of a single machine.

1.1 Learning Representations on Point Sets

Representation learning on images has become state of the art in many different applications like Classification (KRIZHEVSKY *et al.*, 2012), Semantic Segmentation (SHELLHAMER *et al.*, 2014), Recognition – e.g. face recognition (OUYANG *et al.*, 2014), Pose Estimation (XIANG *et al.*, 2017) and so on. Therefore mostly CNN are used, which require a regular structure of processed data.

To be able to apply similar techniques to three dimensional space, one has to ensure a regularly structured data representation, as well. For those purposes, typically a Voxel representation is chosen. Therefore the space is subdivided into volumetric pixels with uniform edge length, accumulating all data points falling within the same Voxel. Then it is possible to extend conventional convolution operations, using kernels with extension to all three dimensions. Those networks mostly are used for tasks like 3D shape recognition (WU *et al.*, 2015) and shape completion (DAI *et al.*, 2017).

Using representations like Voxels comes along with multiple shortcomings. First of all one has to convert the natural representation obtained by a three dimensional sensor, which usually is an unorganized point set, rather than regularly arranged Voxels. Second to mention is an irreversible loss of information caused by accumulation of single data points within Voxels.

Point clouds can be interpreted as an unordered set of vectors from Euclidian space, leading to the following main properties.

The ordering of the points does not include any information, thus the approach has to be invariant to the ordering of the points in the set. A Point Cloud incorporates metric directly. Neighboring points therefore form a meaningful subset. Approaches shall incorporate the local structure of the point cloud. Point Clouds are invariant to certain transformation like rotation and translation. Therefore learned representations have to be invariant to the same transformations.

To be able to operate directly on point clouds, recently few approaches have been published. Since PointNet (Qi *et al.*, 2016) realizes a straightforward implementation acquiring state of the art capabilities, this approach shall be discussed briefly within the next chapter. For experiments we also implemented PointNet++ (Qi *et al.*, 2017) and Dynamic Graph CNN (WANG *et al.*, 2018). In fact our pipeline does not require a special structure of the feature abstraction layer, rather any algorithm, which is capable of abstracting a global feature vector from a point set, can be used.

1.2 PointNet

One of the very first approaches to run CNNs directly on point clouds is PointNet by (Qi *et al.*, 2016). The CNN's structure is shown in **fig. 1**. The main idea is to train a Multi-level Perceptron (MLP) on each point within the point set with shared weights. Multiple MLPs are used leading to a feature vector of dimension 1024 for each point.

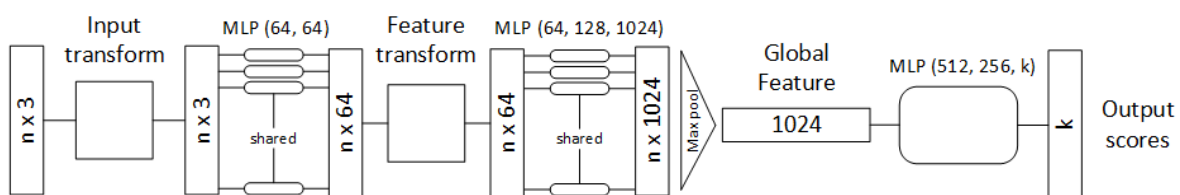


Figure 1: Design of the PointNet CNN by (Qi *et al.*, 2016)

To acquire a global feature vector describing the whole point set, a max pooling layer is used, which is a symmetric function, thus producing the same output no matter the ordering of points.

To achieve invariance with respect to rotation, they use two Spatial Transform Networks (JADEBERG *et al.*, 2015), which learns a 3×3 rotation matrix over the input point set and a 64×64 matrix over midlevel features to align both. To avoid the network to learn undesirable transformations (such as scaling), they introduce an additional loss, which penalizes the transformation matrices for not being orthogonal.

Despite of its comparatively simple design, PointNet has shown to be high-performant dealing with high level tasks like classification. Under slight modifications, it can be used for other high level tasks like point wise segmentation or part segmentation, too.

2 Materials & Methods

A typical processing pipeline to extract positional information from environmental sensors is shown in **fig. 2**. In a first steps segments are generated for raw readings of the environment. After segments are retrieved passing them to an appropriate matching algorithm yields to an estimate of the probability of segments being sampled from the same physical object. This information can then be used to obtain geometric information using appropriate algorithms for geometric verification – e.g. RANSAC (FISCHLER *et al.*, 1981).

In this paper we focus on the matching part of the pipeline shown in **fig. 2**. Therefore we propose an algorithm for Representation Learning directly on Point Sets, which is evaluated within a real world outdoor scenario.

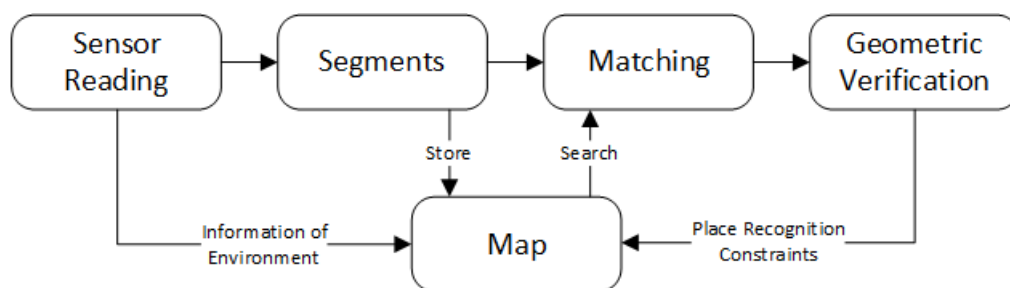


Figure 2: Typical processing pipeline to generate relative position information from readings of environmental sensors

2.1 Segmentation

Following **fig. 2**, the first step of the processing pipelines is to extract segments. Extracted segments can vary substantially depending on the underlying methodology. Segments can be approximated directly on information space, but mostly are calculated using an appropriate feature space.

In 2D Computer Vision features are calculated using the image gradient convolved with in a sliding filter. To acquire scale invariance, images are typically processed with multiple resolutions using e.g. image pyramids for down sampling. Typical feature response functions are built to find corners of any type. Segments are then generated by fitting models – e.g. lines – to correspond best with the appearance of detected features. The goal always is to retrieve homogeneous areas. Therefore algorithms like Region Growing are used. By now most of the common 2D operations for segmentation have been ported to 3D and are publically available e.g. in the Point Cloud Library (Rusu, 2011)

2.2 Matching

Figure 3 shows different segments acquired from the same physical objects. On the left hand side two different point clouds acquired from physically the same tree and the point cloud generated by registering both clouds are shown. The right hand side of the figure shows two different point clouds captured from physically the same car and the combined point cloud.

After retrieving segments, matching multiple of them yields to positional information from the current sensor readings. When an agent maps a specific area and recognizes objects within its current field of view, which were mapped before, e.g. one can close loops on large scale trajectories, which leads to significant reduction of drift.

Furthermore object and especially place recognition can be used to relocalize an agent, which has lost its positional tracking and whose localization lacks of external positional information such as GNSS (often referred to the “kidnapped robot problem”). Using advanced methods it is even possible not only to relocalize an agent within an area it has mapped on its own, but place recognition is a useful method when multiple agents have to be aware of their relative position e.g. to be able to share information within a consistent frame of reference.

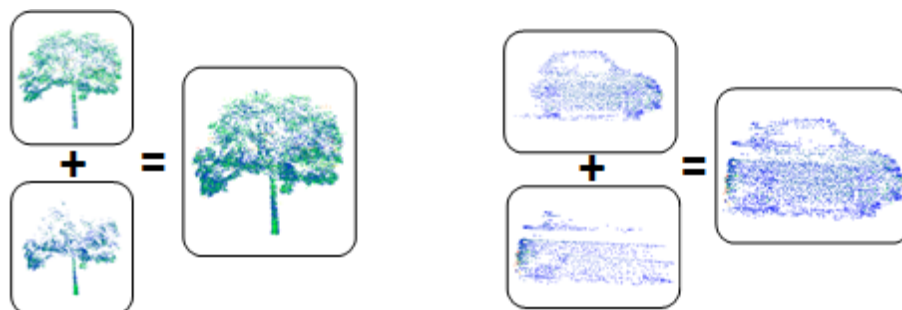


Figure 3: Segments obtained from different perspectives. Left: Two segments acquired from the same tree under different perspectives and the resulting registered point cloud. Right: Two segments acquired from the same car under different perspectives and the resulting registered point cloud.

Traditionally hand crafted features are used to describe segments. Those features can be both, based on the local neighborhood of each point or based on the global shape. Most of the features used on point clouds are derived from 2D features. Another often used approach is based on the eigenvectors and κ -values of the local neighborhood, representing the linearity, planarity and sphericity respectively (DEMANTK *et al.*, 2011).

Based on arbitrary descriptors, a classifier can be trained, which has to be able to distinguish segments acquired from different physical objects and to recognize segments, which are sensed from the surface of the same object. This approach has shown to work quite well, if the segments to match are sampled from roughly the same portion of the surface of the same object, but is likely to fail, if the segments are sampled under varying conditions e.g. from differing perspectives or with other sensing modalities.

2.3 Learning Models for Segment Matching

We propose a matching pipeline as shown in **fig. 4**. The first step of the processing pipeline is uniform sample data points from each segment, since segments can contain arbitrary number of points and the feature abstraction CNN requires a fixed amount of points. In our experiments we use 1024 points. For sampling process we do allow re-picking, to be able to process segments containing less points.

Then n segments are combined to a batch. For experiments we chose a batch size of 16. The batches are then fed to a CNN to abstract global feature vectors for the segments. For experiments a feature dimension F of size 1024 is chosen.

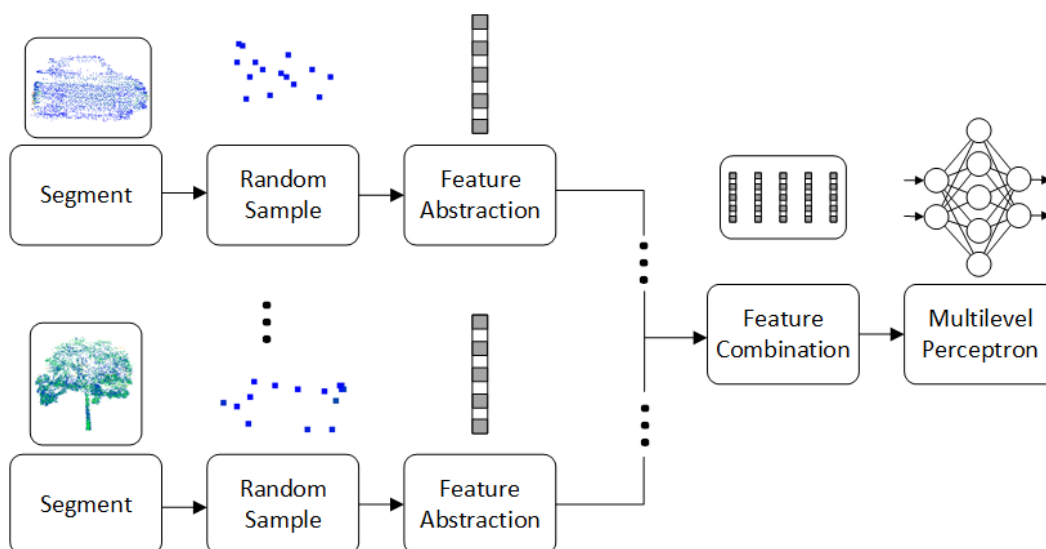


Figure 4: Our processing pipeline to generate matching predictions. From each segment a fixed number of points is uniformly sampled. Then features are calculated using a propitiat CNN. Feature vectors are then combined and a Multilevel Perceptron is trained to predict probabilities for segments to be sampled from same physical object.

Afterwards all point clouds within a batch are concatenated along the feature dimensions. This yields to a tensor of size $[n, n, 2 * F]$. To obtain predictions for potential matches, a MLP is added on top, which reduces the feature dimensions successively in three layers (*channel dimensions: 512, 256, 1*). Before the last layer a single dropout layer is implemented. For experiments the probability to keep the neurons is chosen to 0.7.

We train the MLP by feeding it with labels 0 - for non-matching segments - and label 1 - for matching ones. A sigmoid activation function at the very last layer of the MLP guarantees all predicted values to be in the range from 0 to 1, representing the probability for a positive match. Furthermore a sigmoid like activation function for the output represents best the binary labels since we only feed binary labels at train.

To evaluate accuracy we choose the 95% quantile. Therefore a prediction for a positive match is treated as correct, if predicted probability is greater or equal to 0.95. On the other hand a negative match is treated correct, if the predicted probability is equal or less 0.05.

2.4 Experimental Setup

We evaluated our proposed approach in a real world scenario. **Fig. 5** shows two maps of different physical areas, which were segments generated from for matching.

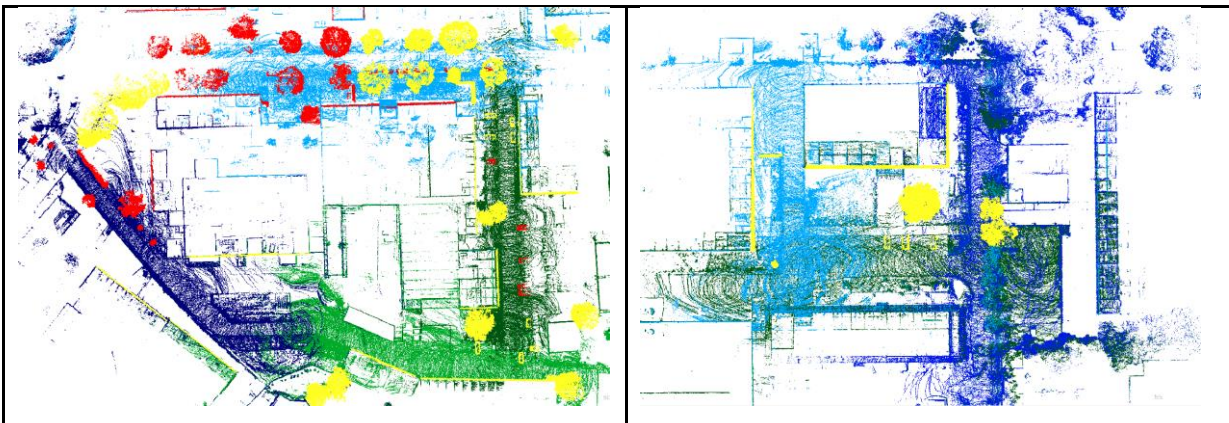


Figure 5: On the left: Map of an outdoor area consisting of four trajectories captured by independent agents. The complete travelled distance is about 500 meters. We segmented 86 different objects at a total of 119 instances for training purposes. Data from this map is used for training the CNN. On the right: Map of another area consisting of three trajectories captured by independent agents. The complete travelled distance is about 300 meters. We segmented 11 different objects at a total of 27 instances. Data from this map is used for evaluating of the CNN.

On the left hand side the maps of four trajectories of independent agents are drawn in dark blue, light blue, dark green and light green. Objects segmented are either shown in red or yellow, whereby yellow signals objects, which were observed by multiple agents from different perspectives (at multiple instances), while red indicates objects, which

were observed only by a single agent. The numbers of objects and instances segmented on both maps is shown in **Table 1**.

Table 1: Objects and instances in train and evaluation data set

-	Training data set		Evaluation data set	
	Objects	Instances	Objects	Instances
Facades	26	30	3	8
High vegetation	30	50	4	11
Low vegetation	5	6	1	2
Cars	25	33	3	7

On the left hand side we travelled a loop around a building complex, which is located in the center of the map. The trajectory on the top is generated while travelling a road, which has plenty trees on each side and multiple cars parking on each side of the street. On the right hand side of the left map, the agent is travelling between buildings reaching a parking lot on the bottom and then travelling along the rear side of the building complex back to the street.

The map on the right hand side consists of two parallel trajectories from top to bottom, which were crossed by a third trajectory from left to right. At the center of the map, we are crossing a parking lot which is surrounded by multiple buildings.

For training and for testing objects of four different classes have been extracted. Those are: facades of buildings, high vegetation (trees), low vegetation (bushes) and cars. Since our goal is to match objects under differing perspectives, to be able to match objects across different agents, we extracted objects on all different trajectories, if present. Thus results in extracting multiple instances of the same object.

3 Results

To evaluate the performance of our proposed pipeline different experiments were processed. In first experiments the influence of the loss function has been analyzed. Results are presented in **fig. 6**. The matching pipeline (ref. **fig. 4**) has been trained with the Mean Square Error Loss function (often referred to L2 Loss), with Mean Absolute Error Loss function (often referred to L1 Loss) and the Huber Loss function. It can be seen, that the model convergences for all three loss functions. Furthermore one can see that convergence speed is the highest and overall performance is best when using L1 Loss.

In a second experiment the goal was to analyze, if overall performance can be boosted by using additional information. First the influence of data augmentation while training was examined. This method is often used to reach higher degree of generalization capabilities of the model in particular if the training data set is small. To extend the training

dataset the segments were rotated, scaled and shifted randomly. Furthermore single points were jittered randomly and points were dropped randomly. In **fig. 7** it can be seen that this procedure will reduce convergence speed while training but increases the overall performance slightly. Additionally it was tested, if transferring additional data is useful. Therefore the feature abstraction layers of the CNN were trained using the famous ModelNet40 (Wu *et al.*, 2015) dataset was used. After full convergence the last layers were replaced with the matching MLP as shown in **fig. 4**. While training the matching MLP the feature abstraction layer was fixed. As shown in Figure 7 this approach did not lead to a worse overall performance.

In a last experiment different CNNs for feature abstraction were tested. Besides PointNet (Qi *et al.*, 2016), the PointNet++ (Qi *et al.*, 2017) and the DGCNN (Wang *et al.*, 2018) was trained and tested. As can be seen in **fig. 8**, the PointNet++ shows the highest convergence speed while training but is evaluated as worst in generalizing to the unseen test data. DGCNN is based on constructing a nearest neighbor graph. Features are generated by calculating distances to the nearest neighbors and a MLP is trained on top of that.

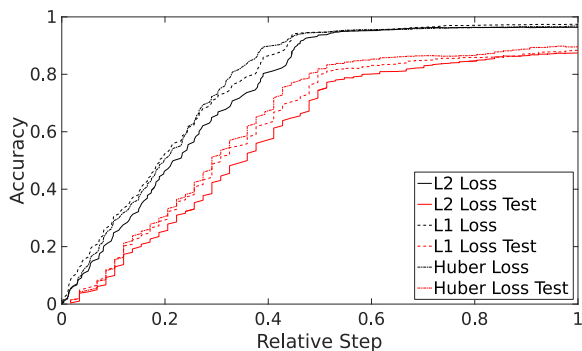


Figure 6: Training process (black) and testing with unseen data (red). L2-Loss (solid line), L1-Loss (dash dot line) and Huber-Loss (dotted line)

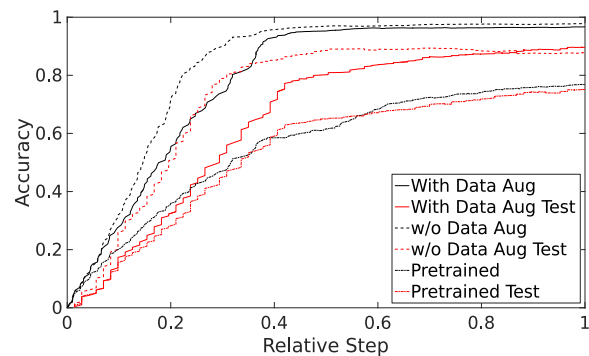


Figure 7: Training process (black) and testing with unseen data (red) with pre-trained feature abstraction layer (dash dot line), without data augmentation (dotted line)

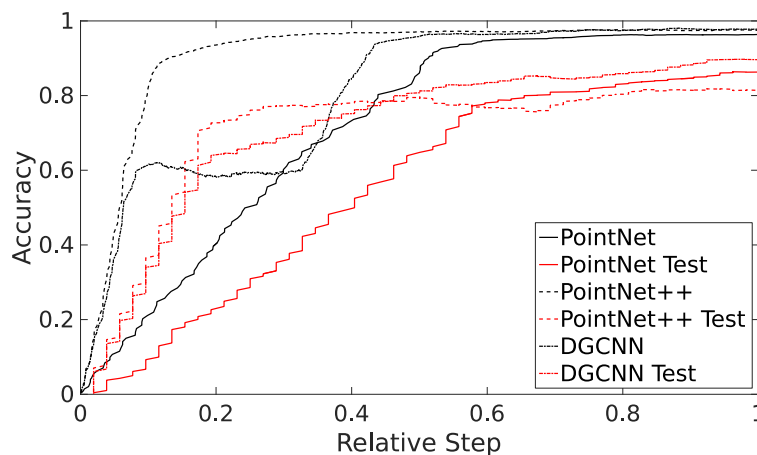


Figure 8: Training process (black) and testing with unseen data (red) of matching pipeline with different CNNs for feature abstraction. PointNet (Qi *et al.*, 2016) (solid line), PointNet++ (Qi *et al.*, 2017) (dash dot line) and DGCNN (Wang *et al.*, 2018) (dotted line)

Table 2 summarizes the results of the different experiments. As can be seen PointNet with L1 Loss leads to best overall performance with respect to matching accuracy.

Table 2: Summarized results of the different experiments.

-	Matching Accuracy	-	Matching Accuracy
PointNet with L2 Loss	92,2 %	PointNet w/o Data Augmentation	91,2 %
PointNet with L1 Loss	93,1 %	Pretrained on ModelNet	88 %
PointNet with Huber Loss	91,2 %	PointNet++	90,4 %
		DGCNN	91,5 %

4 Conclusion

It could be shown, that Deep Learning approaches operating on point clouds directly can be used for segment matching. The experiments have shown, that our proposed method is performing quite well and is able to recognize segments sensed from same physical objects. Furthermore it could be shown, that no additional preprocessing of extracted segments is mandatory and segments with arbitrary number of points can be processed equally.

Acknowledgement

The presented work was done within the joint research project ANKommEn 2 funded by the German Federal Ministry of Economic Affairs and Energy administrated by the Space Administration of the DLR (funding code: 50NA1807).

References

- DAI A, QI C, NIEßNER M (2016):** Shape Completion using 3D-Encoder-Predictor CNNs and Shape Synthesis. In: *CoRR*, abs/1612.00101.
- DEMANTK J, MALLET C, DAVID N, VALLET B (2011):** Dimensionality based scale selection in 3D lidar point clouds. *International Archives of the Photogrammetry, Remote Sensing and Spatial Information Sciences XXXVIII-5/W12*: 97–102.
- FISCHLER M, BOLLES R (1981):** Random Sample Consensus: A Paradigm for Model Fitting with Applications to Image Analysis and Automated Cartography. *Communications of the ACM* 24 (6): 381-395.
- JADERBERG M, SIMONYAN K, ZISSERMAN A, KAVUKCUOGLU K, CORTES C, LAWRENCE ND, LEE DD, SUGIYAMA M, GARNETT R (2015):** Spatial Transformer Networks. *NIPS*: 2017-2025.
- MINBEN TF, HANKE S, SCHATTENBERG J, FRERICHS L, GAUS CC, URSO LM (2017):** Robots for Plant-Specific Care Operations in Arable Farming – Concept and Technological Requirements for the Operation of Robot Swarms for Plant Care Tasks.
- KRIZHEVSKY A, SUTSKEVER I, HINTON GE (2012):** Imagenet classification with deep convolutional neural networks. *Advances in neural information processing systems*: 1097-1105.

- QI CR, SU H, MO K, GUIBAS LJ (2016):** PointNet: Deep Learning on Point Sets for 3D Classification and Segmentation. cite arxiv:1612.00593.
- QI CR, YI L, SU H, GUIBAS LJ (2017):** PointNet++: Deep Hierarchical Feature Learning on Point Sets in a Metric Space. cite arxiv:1706.02413.
- OUYANG W, WANG X, ZENG X, QIU S, LUO P, TIAN Y, LI H, YANG S, WANG Z, LOY CC, TANG X (2014):** DeepID-Net: Deformable Deep Convolutional Neural Networks for Object Detection. *CoRR*, abs/1412.5661.
- RUSU RB, COUSINS S (2011):** 3D is here: Point Cloud Library (PCL). *ICRA*: IEEE.
- SHELHAMER E, LONG J, DARRELL T (2017):** Fully Convolutional Networks for Semantic Segmentation. *IEEE Transactions on Pattern Analysis and Machine Intelligence* 39 (4): 640-651.
- WANG Y, SUN Y, LIU Z, SARMA SE, BRONSTEIN MM, SOLOMON J (2018):** Dynamic Graph CNN for Learning on Point Clouds. *CoRR*, abs/1801.07829.
- WU Z, SONG S, KHOSLA A, YU F, ZHANG L, TANG X, XIAO J (2015):** 3D ShapeNets: A deep representation for volumetric shapes. *CVPR*: IEEE Computer Society. ISBN 978-1-4673-6964-0: 1912-1920.
- XIANG Y, SCHMIDT T, NARAYANAN V, FOX D (2017):** PoseCNN: A Convolutional Neural Network for 6D Object Pose Estimation in Cluttered Scenes. *CoRR*, abs/1711.00199.

Cooperative localization based on range-only measurements from robots and infrastructure

Cyrille Pierre¹, Roland Chapuis¹, Romuald Aufrère¹, Jean Laneurit², Christophe Debain²

¹*Institut Pascal, Clermont-Ferrand, France*

²*Irstea, Clermont-Ferrand, France*

E-mail: cyrille.pierre@uca.fr

Abstract: In this paper, we address the problem of localizing mobile robots based on range-only measurements from low cost Ultra-Wide-Band (UWB) sensors placed in infrastructure and other robots. The cooperative localization problem is simplified and only rely on these range measurements. Each robot perform a Split Intersection Covariance Filter to fusion the highly correlated information of its own sensors. The consistency and the cooperative aspect of this solution are shown in a simulation with 3 heterogeneous robots and several static UWB tags. We also demonstrate its feasibility with a real experimentation with 1 robot and several UWB tags.

Key words: cooperative localization, range only localization, UWB, Split Intersection Covariance, v2v localization, v2i localization

1 Introduction

In agriculture as in many economic fields, mobile robots can improve productivity. If the milking robot has brought a lot in our farms other tasks can also be automated such as the distribution of food. To do that we need mobile robots that can move as well inside and outside cow barns. So that these robots can move they must be able to locate each moment with a very good reliability. Localization is a requirement in a lot of mobile robots applications. A robot is able to locate itself using its own proprioceptive or exteroceptive sensors. However the quality of this localization will depend of the accuracy and the availability of these sensors. When several robots work in a same environment, the localization can be cooperative if the robots are able to detect each other and exchange their information. A solution can be to gather the sensors measurements of the robots and perform a centralized localization. This solution allows keeping the correlation between the robot state vectors but the algorithm cannot be performed in real time if the number of robot is high and this can also lead to high bandwidth usage. (ROUMELIOTIS & BEKEY, 2002) and (MARTINELLI, 2007) have proposed an approach to distribute the computation between the robots.

The modern cooperative localization solutions tend to focus on the decentralized approach which has better real-time performance but is suboptimal (CARRILLO-ARCE *et al.*, 2013), (LASSOUED *et al.*, 2014). If the robot pose estimations are computed independently, the correlation between these poses will be lost. A Kalman filter cannot cor-

rectly handle this problem because the robot pose estimations will be considered as fully independent and the estimation will be inconsistent. One of the solutions is to avoid reusing the same information several times. (KARAM *et al.*, 2006) proposes an approach where each robot computes a local estimation based on its sensors and a fused estimation including all other robots information. Only the local estimation is shared with other robots. Another solution (CARRILLO-ARCE *et al.*, 2013) is based on the Covariance Intersection Filter (JULIER *et al.*, 2009). In this filter, the correlation between the measurements and state vector are considered as fully dependent. This corresponds to a pessimistic version of the Kalman Filter. This dependency can be configured more precisely with the Split Covariance Intersection Filter and allows making better pose estimation (LI & NASHASHIBI, 2013), (WANASINGHE *et al.*, 2014).

In most of these approaches, a measurement with another robot corresponds to a pose measurement. This type of measurement allows exploiting all the information of the state vector of the other robot. In practice, it is difficult to measure a pose difference. This can be done using LIDARs (HOWARD, 2002), (HOWARD, 2003) or camera (DAVINSON, 2000) but these solutions require data processing and impose constraints on the robots. The main problem mentioned in this paper is the ability to perform a cooperative localization with heterogeneous robots and with robot-to-robot or robot-to-infrastructure measurements. The sensor able to make these measurements must be easily embedded in any object.

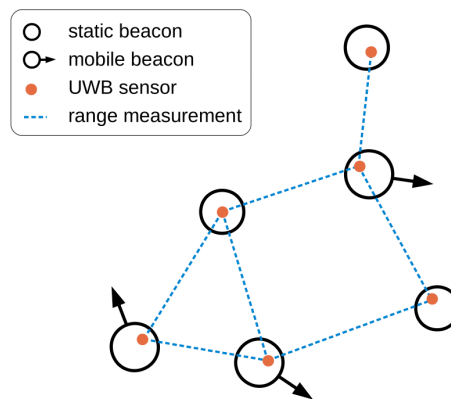


Figure 1: Illustration of the beacons (robots or static object) and the range measurements of its UWB sensors

The Ultra Wide Band (UWB) sensor meets these constraints. It allows making range measurement from another UWB sensor with a centimetric precision and it is low cost. However, the technology of this sensor does not allow exploiting the classic trilateration process because the range measurement requests cannot be done simultaneously (GONZÁLEZ, 2009), (LANEURIT *et al.*, 2016). Moreover, it is well known that range only data lead to very non-linear functions that are difficult to handle for fusion.

A measurement with a beacon involves the range measurement but also the current position estimation computed by the target beacon. With this generic architecture, the cooperative localization aspect is hidden behind these measurements: A robot does not

need to know if the target is a robot or an element of the infrastructure. This strategy simplifies the cooperative localization problem but it does not solve it. Suppose a static beacon has a non-negligible position uncertainty. A robot should make several measurements from this beacon, but this induces an overuse of the position information of the beacon. A Kalman filter cannot correctly handle this highly correlated position uncertainty because it will introduce inconsistency in the robot state estimation. Our solution is based on the Split Covariance Intersection filter which allows splitting the covariance matrix into independent and dependent covariance matrices (JULIER *et al.*, 2009), (LI *et al.*, 2013). In our case, the range measurement of a beacon can be considered independent of the previous measurement but its position is very correlated to the previous one.

2 Localization Algorithm

From a general point of view, this algorithm acts as cooperative localization but for a robot, this is a classical fusion algorithm with simple robots measurements. In this approach, the localization of each robot is computed individually, thus the algorithm described here will only concern the current robot. However, the same algorithm is applied to every other robot or beacons if needed. The localization problem is modeled by an estimation of the state X_k of the robot at the moment k . We use a bayesian approach based on the classical state model:

$$X_k = f(X_{k-1}, U_k, W_k) \quad (1)$$

$$Z_k^{(i)} = h^{(i)}(X_k, V_k^{(i)}) \quad (2)$$

The evolution function f is based on the vector u_k including proprioceptive information of the robot and the involved noise vector w_k of the model. The function $h(i)$ describes one of the observation model. This function allows to link the i th measurement vector $z_k(i)$ to the robot state X_k . This model also involves a noise vector $v_k(i)$.

2.1 The fusion algorithm

The fusion algorithm used in this approach is the Split Intersection Covariance Filter (SCIF). It is an alternative between the Kalman Filter (KF) and the Covariance Intersection Filter (CIF) (JULIER *et al.*, 2009). The KF allows to estimate a dynamic state by merging informations from several sources. One of the particularity of this algorithm is to consider that every information is independent. Conversely, the CIF considers that every information is highly correlated to another. The SCIF combines these two approaches to provide more flexibility in the control of the information correlation.

In a standard KF, the estimate of a state X_k at the moment k corresponds to a pair $(X_{k|k}; P_{k|k})$ where $X_{k|k}$ is the state vector and $P_{k|k}$ is its associated covariance matrix.

$$p(X_k) \sim N(X_{k|k}, P_{k|k}) \quad (3)$$

In a SCIF, this matrix is cut in two parts: the independent covariance matrix $P_{i,k|k}$ corresponding to the covariance of the state without correlation from any sources and the dependent covariance matrix $P_{d,k|k}$ corresponding to the correlated one.

$$P_{k|k} = P_{i,k|k} + P_{d,k|k} \quad (4)$$

Thus the SCIF works with the triplet $(X_{k|k}, P_{i,k|k}, P_{d,k|k})$. This formalism is also applied to any information vector to fuse. For example, if the triplet (z_k, R_{ik}, R_{dk}) is a sensor measurement, the matrix R_{dk} will contain the estimated part of its uncertainty correlated with a previous observation.

2.2 The evolution model

The robot state X is a vector containing the position x, y, z and the orientation of the robot at the moment k .

$$X_k = [x \ y \ z \ \theta]_k^T \quad (5)$$

The third geometric dimension is necessary because the UWB sensors can be placed to any height from ground and this height will affect the range measurement. However, in our experimentations, all robots move on a relatively flat ground, thus only the yaw angle is used for the orientation of the robot.

There are various robot models but, in this paper, only the Ackermann model has been used. The proprioceptive informations of our robots correspond to the speed s and the steering angle φ of the front wheels. These measurements are associated to the noise vector W .

$$U_k = [s \ \varphi]_k^T \quad W_k = [w_s \ w_\varphi]_k^T \quad (6)$$

Given the period δt and the wheelbase of the robot L , the evolution function is:

$$f(X_k, U_k, W_k) = X_k + \begin{bmatrix} (s + w_s)\delta t \cos \theta \\ (s + w_s)\delta t \sin \theta \\ 0 \\ -\frac{s+w_s}{L} \delta t \tan(\varphi + w_\varphi) \end{bmatrix}_k \quad (7)$$

2.3 The observation models

Different observation models based on different sensors are used in this approach but the main model rely the UWB sensor. These sensors can perform range-only measurement z_{bk} at the moment k but we add some contextual informations: the position of the target UWB and the uncertainty of this position. This uncertainty follows a normal distribution and can be modeled as a mean value b_k and covariance matrix B_k . If the target beacon is static, its position have been fixed at its initialization. But if this beacon corresponds to a mobile object (like another robot), its position information is extracted from its current state estimation.

In both cases, a measurement will be correlated to previous measurements with the same target because its position information may change a little. This implies that the uncertainty of the target position must be processed as a dependent covariance. (**Fig. 2**) illustrates the importance of this configuration. If the only information source of the robot localization is an unique beacon, the position estimation of the robot cannot be better than the beacon position estimation.

Let (z_b, R_i, R_d) be a range measurement with a target beacon. The noise vector V of this measurement contains the range measurement noise v_r and also the beacon position noise vector $V_p \in \mathbb{R}^3$. Thus, z_b is a scalar corresponding to the range measurement.

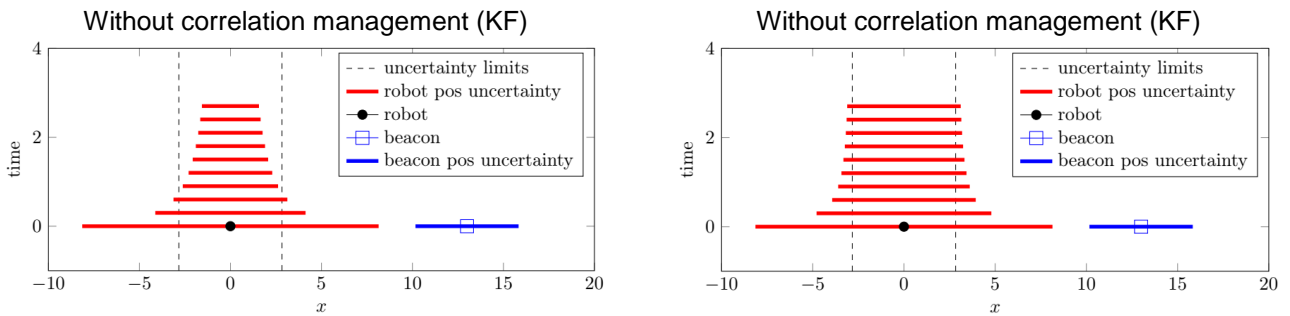


Figure 2: Evolution of the robot position uncertainty after several noisy range measurements from a beacon. With a standard KF, the position uncertainty of the beacon is used as a new information for each range measurement, thus the robot position estimation will lose its integrity. In the second case, the position uncertainty is considered as fully dependent on the robot state, thus the overconvergence is avoided.

$$R_i = \begin{bmatrix} \sigma_r^2 & 0 \\ 0 & 0 \end{bmatrix}, \quad R_d = \begin{bmatrix} 0 & 0 \\ 0 & B \end{bmatrix} \quad (8)$$

R_i, R_d contain the range measurement variance σ_r^2 and the position covariance matrix of the beacon B . For a UWB sensor, the range measurement has a static error but the noise is white. The observation function h_b of a range measurement uses the position of the target beacon p_b as a constant. Because the sensor of the robot used in this measurement can be placed anywhere on the robot, this function also integrates a sensor position P_s .

$$h_b(X, V) = \|(x, y, z)^T + \text{rot}(\theta)P_s - p_b - V_p\| + V_r \quad (9)$$

$$\text{rot}(\theta) = \begin{bmatrix} \cos \theta & -\sin \theta & 0 \\ \sin \theta & \cos \theta & 0 \\ 0 & 0 & 1 \end{bmatrix} \quad (10)$$

A localization based on range measurement from individual beacon is unstable when the position uncertainty is significant because of the non-linearity of the model. That's why we use low cost GPS to make a brief estimation of the robot position. Let $(Z_g; G_i; G_d)$ be a position measurement from a GPS, the vector $Z_g \in \mathbb{R}^3$ contains the measured position and V_g corresponds to the noise of this measurement. The measurements of this kind of sensor are easily disturbed by the environment and its noise cannot be con-

sidered as white. It is possible to improve the model and integrate a bias parameter in the robot state to model more accurately its noise (TAO *et al.*, 2013). Because we do not need to have an accurate model of this sensor, we only consider that a part of the covariance is dependent to previous measurements.

Given the sensor position vector P_g , the observation function of a GPS is:

$$h_g(X, V_g) = (x, y, z)^T + \text{rot}(\theta)P_g + V_g \quad (11)$$

3 Results

3.1 Simulation

In this section, we present a simulation with 3 robots and several static beacons using a realistic simulator able to simulate robot physics and sensor noises. The simulation is performed in an agricultural context: the environment is a farm and vehicles used are adapted to this kind of land (**Fig. 3**).



Figure 3: The 3D environment of the simulator (4D-Virtualiz): a farm, 2 RobucarTT (robot 1 & 3) and a tractor (robot 2)

The configuration of the robots and the position of the static beacons allow testing the main characteristics of this approach. We use different robot sizes (a tractor and a smaller robot) and different sensor configurations (**Table 1**). For example, robot 1 has two UWB sensors and, consequently, increases the harvested information from its neighbours. The trajectory of the robots and the position of the other beacons allow testing the localization in different circumstances. All robots will follow a path around the farm in a dynamic convoy. Most of the time, the robot 3 is used as an accurately localized mobile beacon. The simulated RTK GPS used in this robot enable it to make almost perfect position measurements. The configuration of all sensors is presented in the (**Table 2**).

Table 1: Characteristics of the robots

Characteristic	robot 1	robot 2	robot 3
robot type	Robucar TT	tractor	Robucar TT
robot size (m)	$2.63 \times 1.23 \times 1.35$	$5 \times 3 \times 2.95$	$2.63 \times 1.23 \times 1.35$
GPS type	Low cost	Low cost	RTK
UWB sensors	2	1	1

Table 2: Configuration of the simulated sensors

Robot 1 & 2		
Parameter	Value	Unit
odometry measurement freq	10	Hz
std. dev. of linear speed	0.24	m.s-1
std. dev. of steering angle	0.02	rad
GPS measurement freq.	10	Hz
std. dev. of GPS (x & y)	12	m
beacons measurement freq.	10	Hz
Robot 3		
odometry measurement freq.	10	Hz
std. dev. of linear speed	0.24	m.s-1
std. dev. of steering angle	0.02	rad
GPS measurement freq.	10	Hz
std. dev. of GPS (x & y)	0.12	m
std. dev. of GPS (z)	0.3	m
beacons measurement freq.	10	Hz
Static beacons		
number of static beacons	6	
maximal range	25	m
std. dev. of position (x, y & z)	0.2	m
std. dev. of range measurement	0.15	m

The simulation can be cut in 4 steps described in the (**Table 3**). All the state vectors of the robots are initialized to the center of the area and with a sufficiently high uncertainty to cover all the area. At the beginning, the GPS measurements of robots 1 and 2 allow to make a brief estimation of the position and correct the orientation of these robots after few seconds. Because of its low quality, these measurements cannot be used to make accurate localization but they limit the uncertainty of the state and thus, the non-linearity phenomenon on the range measurements. In the third step of the simulation, all GPS sensors are disabled. This allows simulating an indoor localization. During this period, the robot 3 has no advantage over the other robots.

Table 3: Scenario of the simulation

Time	Description
0 s	Only GPS are enabled. This initialisation step allows to make a brief estimation of the robot poses
18 s	GPS and UWB sensors are enabled. The robots start measuring each other. Later, the robots enter in the range of the first beacon.
68 s	Only UWB sensors are enabled. The robots can see simultaneously 1 or 2 static beacons. After 20 seconds, the robot 3 leave the range of all beacons.
118 s	GPS and UWB sensors are enabled. There is no more static beacons in range of the robots.

The objective of this simulation is to validate the consistency of the pose estimation for all robots. The quality of the localization is measured through the distance between the

estimated pose of a robot and the real pose. A Monte Carlo procedure based on 100 simulations has been used to improve the results.

The mean and the standard deviation of these simulations are shown in (Fig. 4, 5 and 6) During the first 18 seconds, the position error of robots 1 and 3 is significant because the GPS measurements are biased. However the high uncertainty of these measurements allows to keep a consistent estimation of the pose. When the beacons measurements start, the pose estimation becomes more accurate. When there is no visible static beacon, the accuracy of the pose estimation of the robots 1 and 2 is provided by the range measurement with the robot 3.

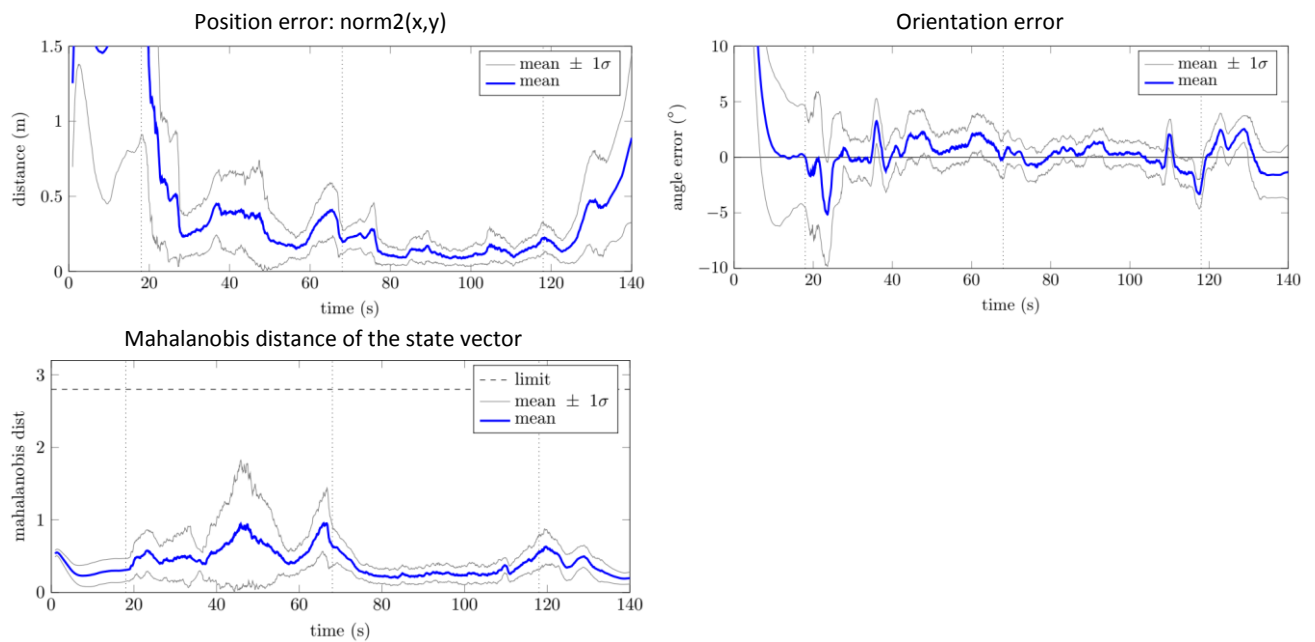


Figure 4: The results of the localization of the robots 1. The curves correspond to the mean error of the pose estimation and its standard deviation for 100 simulations.

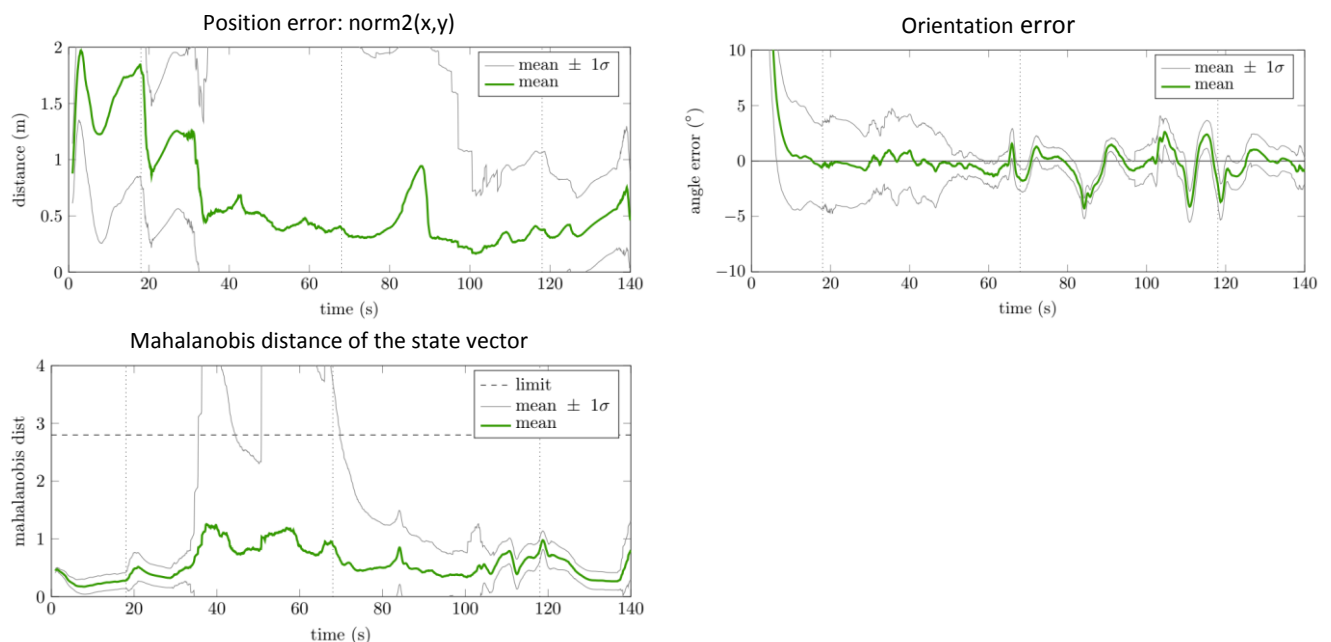


Figure 5: The results of the localization of the robots 2. The curves correspond to the mean error of the pose estimation and its standard deviation for 100 simulations.

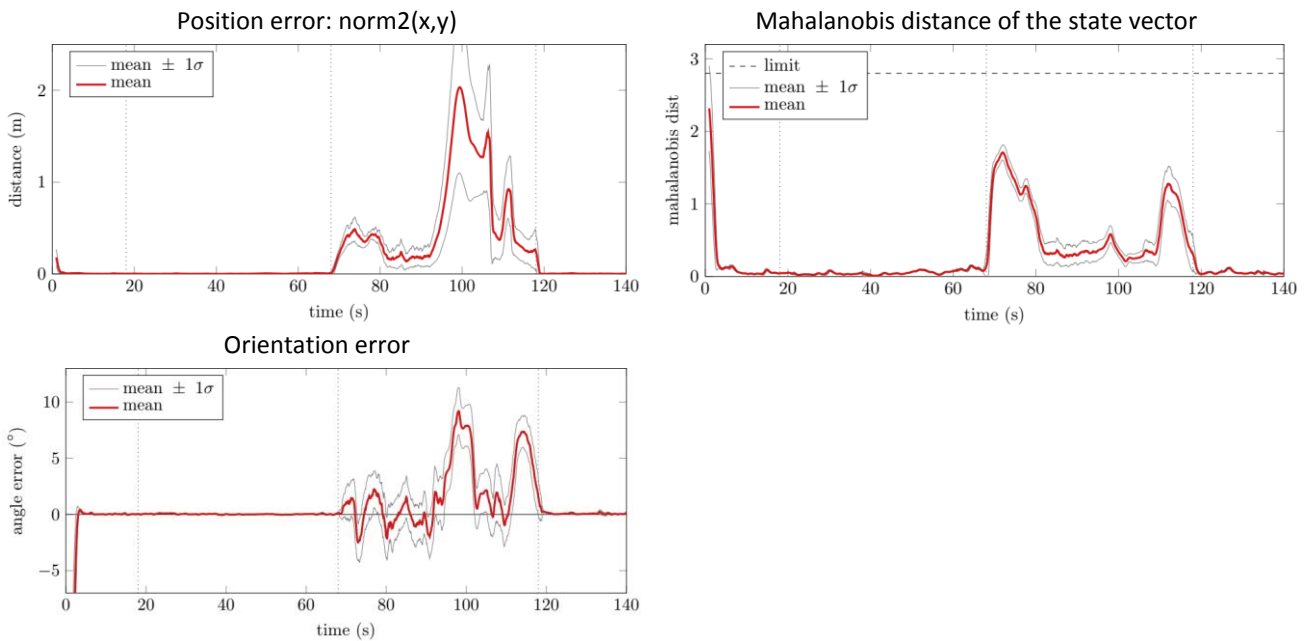


Figure 6: The results of the localization of the robots 3. The curves correspond to the mean error of the pose estimation and its standard deviation for 100 simulations

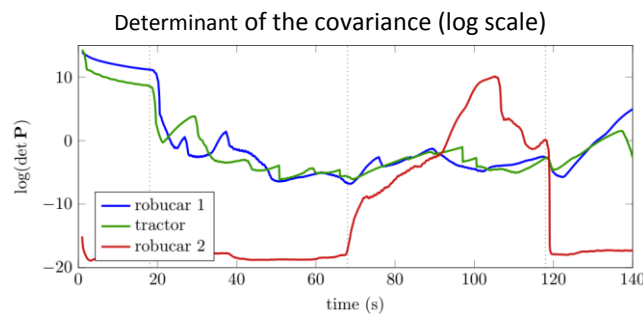


Figure 7: The determinant of the state covariance matrix for each robot. This information gives a good estimation of the covariance matrix size

The quality of this measurement is enough to make the measurements of a low cost GPS negligible but the best result happen when there are several static beacons within range.

The Mahalanobis distance between the estimated vector (x, y, θ) and the ground truth allows to evaluate the consistency of the localization. For a 3 degrees of freedom chi-square random variable, the square root of the 5 % tail point is $\sqrt{\chi_3^2(0.95)} = 2.8$.

Because the mean Mahalanobis distance is always lower than 2.8, we consider that the result of the simulation is consistent for all robots (Bar-Shalom, 2004). However we can see that, sometimes, the accuracy of the robot position decreases. This occurs when the robot is not able to see more than one beacon. Consequently, the odometry noise cannot be corrected in all direction and the non-linearity of the range measurement pull the pose estimation off the ground truth.

3.2 Real experimentation

In this section, we present an experimentation with a real robot. The objective of this experimentation is to validate the accuracy of the localization with real UWB sensors. The second objective is to show that a range-only localization algorithm is an efficient solution to handle indoor and outdoor localization problem.

The environment is similar to the simulated one but the beacons configuration is different. The robot is equipped with a RTK GPS and two UWB sensors (**Table 4**). In the same way as the simulation, the GPS measurements will be disabled and the localization will become range only. In this experimentation, the trajectory of the robot begins with an outdoor environment and passes through a cow barn (**Fig. 8, 9**). The GPS will be temporarily inoperable and then, the observations will be based on the UWB measurements with the static beacons placed in the barn.

The results of this experimentation demonstrate that a localization based on range measurement from UWB sensor is a workable solution to the indoor/outdoor problem. We cannot go into detail about the accuracy of the indoor localization because these conditions don't allow having a ground truth. However the uncertainty of the estimated pose and the trajectory of the robot indicate that the consistency is kept. The quality of the localization can also be studied when the robot moves towards the exit of the barn. At this point the RTK GPS can again give accurate measurements and the localization can be improved by this precise observations. In this experimentation, the very small jump in the localization after the fusion with the first GPS measurement show that the bias created during the range only period is low.



Figure 8: The trajectory of the robot and the position of the static beacons. The localization algorithm is running and the robot is in the barn



Figure 9: A picture of the robot in front of the entrance of the cow barn

Table 4: Characteristics of the robot

Characteristic	value
robot type	Minitract
robot size (m)	$2 \times 1.2 \times 1.5$
GPS type	RTK
number of UWB sensors	2

Table 5: Configuration of the experimentation

Robot			
Parameter	Value	Unit	
odometry measurement freq.	100	Hz	
std. dev. of linear speed	0.1	m.s ⁻¹	
std. dev. of angular speed	0.02	rad	
GPS measurement freq.	11	Hz	
std. dev. of GPS (x & y)	0.8	m	
beacons measurement freq.	10	Hz	
Static beacons			
number of static beacons	6		
maximal range	20	m	
std. dev. of position (x, y & z)	0.3	m	
std. dev. of range measurement	0.15	m	

4 Conclusion and future works

In this paper we presented a localization algorithm based on range measurements from mobile or static beacons. If this algorithm is performed by several beacons, the localization becomes cooperative thanks to the information exchange during the measurements with other beacons. This strategy allows generalize the vehicle to vehicle and the vehicle to infrastructure localization problem and also hide the complexity of the cooperative localization.

We have tested the algorithm in a simulation and a real experimentation with heterogeneous robots and various environment configurations. We show that this algorithm is a viable solution for indoor and outdoor localization and give reliable and precise results.

However this work assumes that the robot pose estimation is sufficiently accurate at any time to avoid the linearity problem of the range-only measurements. This issue can be solved by using sensor able to make this first estimation. This algorithm can be improved by implementing a solution able to handle this non-linearity and maintains the consistency of the localization in all cases.

Acknowledgment

This work has been sponsored by the French government research programm Investissements d'avenir through the RobotEx Equipment of Excellence (ANR-10-EQPX-44) and the IMobS3 Laboratory of Excellence (ANR-10-LABX-16-01), by the European Union through the programm Regional competitiveness and employment 2007-2013 (ERDF – Auvergne region), by the Auvergne region and by French Institute for Advanced Mechanics

References

- BAR-SHALOM Y, LI XR, KIRUBARAJAN T (2004):** Estimation with Applications to Tracking and Navigation: Theory Algorithms and Software. John Wiley & Sons.
- CARRILLO-ARCE LC, NERURKAR ED, GORDILLO JL, ROUMELIOTIS SI (2013):** Decentralized multi-robot cooperative localization using covariance intersection. International Conference on Intelligent Robots and Systems (IROS), IEEE.
- DAVISON AJ, KITA N (2000):** Active visual localisation for cooperating inspection robots. International Conference on Intelligent Robots and Systems (IROS), vol. 3, IEEE.
- GONZÁLEZ J, BLANCO JL, GALINDO C, ORTIZ-DE-GALISTEO A, FERNÁNDEZ-MADRIGAL JA, MORENO FA, MARTINEZ JL (2009):** Mobile robot localization based on Ultra-Wide-Band ranging: A particle filter approach. *Robotics and autonomous systems* 57(5).
- HOWARD A, MATARK MJ, SUKHATME GS (2002):** Localization for mobile robot teams using maximum likelihood estimation. International Conference on Intelligent Robots and Systems (IROS), vol. 1, IEEE.
- HOWARD A, MATARIC MJ, SUKHATME GS (2003):** Putting the 'I' in 'team': An ego-centric approach to cooperative localization. International Conference on Robotics and Automation (ICRA), vol. 1, IEEE.
- JULIER SJ, UHLMANN JK (2009):** General decentralized data fusion with covariance intersection. Handbook of Multi-sensor Data Fusion: Theory and Practice.
- KARAM N, CHAUSSE F, AUFRERE R, CHAPUIS R (2006):** Localization of a group of communicating vehicles by state exchange. International Conference on Intelligent Robots and Systems (IROS), IEEE.
- LANEURIT J, CHAPUIS R, DEBAIN C (2016):** TRACKBOD, an accurate, robust and low cost system for mobile robot person following. International Conference on Machine Control & Guidance (MCG).
- LASSOUED K, FANTONI I, BONNIFAIT P (2015):** Mutual localization and positioning of vehicles sharing GNSS pseudorange: Sequential bayesian approach and experiments. International Conference on Intelligent Transportation Systems (ITSC), IEEE.
- LASSOUED K, STANOI O, BONNIFAIT P, FANTONI I (2014):** Mobile robots cooperation with biased exteroceptive measurements. International Conference on Control Automation Robotics & Vision (ICARCV), IEEE.
- LI H, NASHASHIBI F (2013):** Cooperative multi-vehicle localization using split covariance intersection filter. *IEEE Intelligent transportation systems magazine* 5(2).
- LI H, NASHASHIBI F, YANG M (2013):** Split covariance intersection filter: Theory and its application to vehicle localization. *IEEE Transactions on Intelligent Transportation Systems* 14(4).
- MARTINELLI A (2007):** Improving the precision on multi robot localization by using a series of filters hierarchically distributed. International Conference on Intelligent Robots and Systems (IROS), IEEE.
- ROUMELIOTIS SI, BEKEY GA (2002):** Distributed multirobot localization. *IEEE Transactions on Robotics and Automation* 18(5).
- TAO Z, BONNIFAIT P, FREMONT V, IBANEZ-GUZMAN J (2013):** Mapping and localization using GPS, lane markings and proprioceptive sensors. International Conference on Intelligent Robots and Systems (IROS), IEEE.
- WANASINGHE TR, MANN GKI, GOSINE RG (2014):** De-centralized Cooperative Localization for Heterogeneous Multi-robot System Using Split Covariance Intersection Filter. Canadian Conference on Computer and Robot Vision (CRV).

Comparison of controls for a stereo camera based reversing assistance system for vehicle trailer combinations

Ilja Stasewitsch, Tobias Blume, Jan Schattenberg, Ludger Frerichs

*Institut für mobile Maschinen und Nutzfahrzeuge Technische Universität Braunschweig, Langer
Kamp 19a, 38106 Braunschweig, Germany*

E-mail: i.stasewitsch@tu-bs.de, Tel.: +49 531 3912665

Abstract: This paper will compare two control methods for a reversing assistance system which are able to control the angle of the last vehicle trailer combination joint. One method is based on a feedback linearization of the combination with a reference-model control. The other method is a nonlinear model predictive control. Firstly, the comparison is executed in a simulation for the implementation of a suitable control scheme and preset the control parameters to verify control algorithms. For the studies on the real test vehicle the controlled angles are not measured directly with angle sensors. Instead, the angles are identified through a stereo vision camera and the iterative closest point algorithm. This algorithm calculates the angles by matching a model with the current scene.

Keywords: 3D point cloud processing, feedback linearization, nonlinear model predictive control, reference-model control, reversing assistance system, vehicle trailer combination

1 Introduction

The trend in the agricultural and construction machinery industry is like in the automotive industry to install more advanced driver-assistance systems. The main goal is to reduce the workload of truck drivers and farmers. One opportunity is to automate the reversing for combinations composed of vehicles with full trailer or two semi-trailer. A full trailer has a turnable front axle so that the two hitch and the front axle lead to two joints. A semi-trailer does not have a front axle but two coupled semi-trailers have two joints. The jackknifing between the vehicle and the trailer is a difficult circumstance for the driver during the reversing. With this assistant system the driver is able to control the full trailer, i.e. the driver is steering the trailer and the control strategy adjust the tractor's steering. Related literature handles either path tracking control (LAUMOND, 1993, BOLZERN *et al.*, 2001) or considering only one semi-trailer (CHIU & GOSWAMI, 2012). Designing such a driver assist, the only suitable literature source is (SKLYARENKO *et al.*, 2013). A full-trailer coupled to a vehicle was here controlled by designing a control based on feedback linearization with a reference-model control (FBLC). The project team implemented initially this control strategy. Subsequent to the verification in the simulation, experiments on the test vehicle revealed that the dynamic of the FBLC is not satisfied. Therefore, the project team implemented a nonlinear model predictive control

(NMPC) because of the ability to consider the system constraints in the control. The constraints are important for this application because the system can get into an irreversible state. Only driving forward can restore that.

2 Material and methods

Fig. 1 illustrates the developed assistance system. A reference value for the angle between the drawbar and the trailer φ_T^{ref} is set by a joystick. By the help of φ_T^{ref} an equilibrium for angle between the tractor and drawbar φ_D^{ref} is calculated. A kinematic model of the system was used for calculation and the control methods (see section 2.1). A FBLC (see section 2.3) or a NMPC (see section 2.4) are used as the control method to generate a suitable steering angle φ_S . The robotics simulator Gazebo and a Fendt 724 were used as test environments (see section 2.5). At the Fendt 724 φ_T and φ_D are identified by a stereo vision camera “MultiSense S21” (see section 2.2). Using this modules in a control loop, the trailer can be steered with the joystick like a vehicle with front steering.

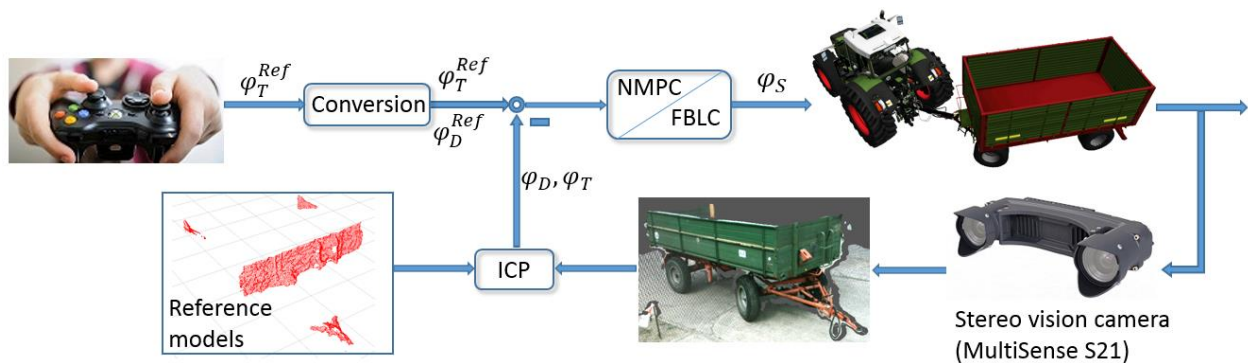


Figure 1: Schematic overview of implemented control structure

2.1 System modeling

The design of a FBLC and a MPC needs because of their model based approach a system model. This model has to describe for this application the system behavior in the reverse driving direction. The vehicle drive with small and constant velocities and the resulting slight accelerations occur only at the maneuver start. For this reason the dynamic of slippage and inertia does not have to be considered. These simplifications are sufficient regarding to the accuracy and using in a FBLC and NMPC. Especially, the few differential equations of the model are advantageous concerning the computation time at the NMPC. **Fig. 2** depicts the schematic representation of a vehicle with a full trailer where the tow hitch is out of the vehicle’s rear axle. The following variables and parameters are used in this figure:

φ_S - Steering angle	l_V - Distance between vehicle's axes = 2.78 m
φ_D - Angle between vehicle and drawbar	l_C - Length of the tow hitch = -0.76 m
φ_T - Angle between drawbar and trailer	l_D - Length of the drawbar = 2.53 m
v_F - Velocity at the vehicle's front wheels	l_T - Distance between the full trailer's axes = 3.03 m

The differential equations

$$\dot{\varphi}_D = \left(-\frac{v_F}{l_T} \sin \varphi_D \cos \varphi_T + \frac{v_F}{l_D} \sin \varphi_T \right) \cos \varphi_S - \left(\frac{v_F l_C}{l_V l_T} \sin \varphi_D \sin \varphi_T + \frac{v_F l_C}{l_V l_D} \cos \varphi_T \right) \sin \varphi_S \quad (1)$$

$$\dot{\varphi}_T = -\frac{v_F}{l_D} \sin \varphi_T \cos \varphi_S + \frac{v_F l_C}{l_V l_D} \cos \varphi_T \sin \varphi_S - \frac{v_F}{l_V} \sin \varphi_S \quad (2)$$

for the system model are taken out from (SKLYARENKO *et al.*, 2013). Only the kinematic of angles φ_D and φ_T have to be considered, because a position control is not applied and the dynamic is ignored. Additionally, the steering is considered by a first-lag order lag element

$$\dot{\varphi}_S = (u - \varphi_S) \frac{1}{T_{Steer}} \quad (3)$$

to get a more exact system behavior where u is the system input and $T_{Steer} = 0.35 \text{ s}$ is the time constant for the vehicle's steering dynamic determined by step responses.

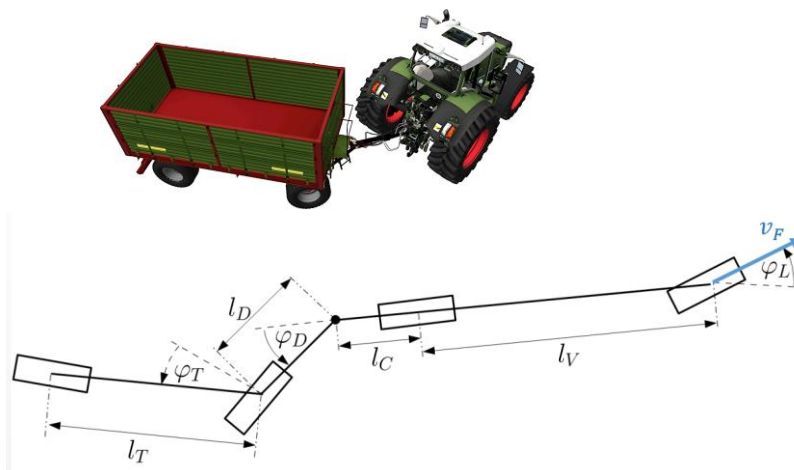


Figure 2: Planar bicycle model of vehicle with a full trailer

2.2 Angle computation

To compute the angles φ_T and φ_D we utilize the stereo vision camera MultiSense S21. This camera is placed on the roof of the tractor and bended so that the drawbar and the front wall are in the field of view. **Fig. 3** shows an exemplary 3D image of the full trailer. The relevant parts of the trailer are the drawbar and the front wall. A model as a point cloud of each part is generated by applying thresholds to separate them from the surrounding and irrelevant trailer parts. At each sampling time the relevant parts are filtered

from the depth image as the source point clouds for the iterative closest point algorithm. The iterative closest point algorithm was introduced in (BESL & MCKAY, 1992). Subsequently, these source point clouds are aligned with the reference point clouds (model) for each part in a separate ICP to get the transformation between the point clouds. From these transformation the angles φ_T and φ_D can be determined.

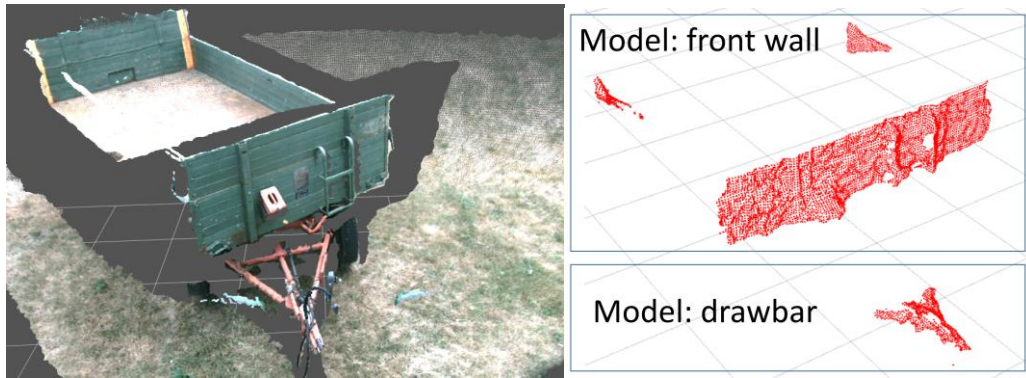


Figure 3: Source and reference point clouds for the calculations of the angles

2.3 Basics and implementation of the control based on feedback linearization

The feedback linearization bases on the idea by ISIDORI (2013) to design a controller so that the nonlinearities are compensated. A respective state transformation linearizes the system behavior between the input and output and a linear control method can be used for the linearized system behavior. This method is valid for control-affine systems, which is usually the issue, and the basic idea is shown for a nonlinear control-affine SISO-System with the states \mathbf{x} , the system input u and the system output y

$$\begin{aligned}\dot{\mathbf{x}} &= \mathbf{a}(\mathbf{x}) + \mathbf{b}(\mathbf{x}) u \\ y &= c(\mathbf{x})\end{aligned}\quad (4)$$

If a diffeomorphic state transformation $\mathbf{z}(\mathbf{x}) = [z_1(\mathbf{x}) \dots z_n(\mathbf{x})]^T$ can be found, then the system (4) can be transformed to the nonlinear controllable canonical form $\dot{\mathbf{z}} = [z_2, \dots, z_n, \alpha(\mathbf{x}) + \beta(\mathbf{x})u]^T$. With the aid of input $u = (v - \alpha(\mathbf{x})) \beta^{-1}(\mathbf{x})$ the system can be transformed into the linear state space representation

$$\dot{\mathbf{z}} = \mathbf{A}\mathbf{z} + \mathbf{B}v \quad (5)$$

The system matrix \mathbf{A} and the input vector \mathbf{B} of Eq. (5) is present in the canonical Brunovský form

$$\mathbf{A} = \begin{bmatrix} 0 & 1 & 0 & \dots & 0 \\ 0 & 0 & 1 & \dots & 0 \\ \vdots & \vdots & \vdots & \ddots & \vdots \\ 0 & 0 & 0 & \dots & 1 \\ 0 & 0 & 0 & 0 & 0 \end{bmatrix}, \mathbf{B} = \begin{bmatrix} 0 \\ 0 \\ \vdots \\ 0 \\ 1 \end{bmatrix} \quad (6)$$

i.e. the input-output system linearization yield to a dynamic free system representation which consist only of an integrator chain. A state controller can be applied on the system Eq. (5) to define the control dynamic.

For the system Eqs. (1) and (2) a diffeomorphic state transformation was found in (SKLYARENKO *et al.*, 2013) but this transformation is restricted on the operating point. In spite of this restriction, the feedback linearization is properly functioning with a reference-model control strategy which is illustrated in **Fig. 3**. Here, a simulation model is controlled in the first control loop. The output of this controller is used as feedforward for the subsequent control loop that controls the actual system. The input of the second control loop is the system output of the first control loop. The second control loop only eliminates model errors of the first control loop and disturbances that affect it. Thus, the first control loop determines the reference behavior of the strategy. The advantage of this method is that the system model does not have to be invertible, especially if this is not possible. In this case the steering dynamic can be taken into account, even if no state transformation exists for this model extension. According to section 2, the dynamics of a feedback linearized control loop can be arbitrarily defined. The linear transfer function

$$G(s) = \frac{1}{s^2 + 2Dw_0 s + w_0^2} \quad (7)$$

is used to determine the control loop dynamic by the state controllers for further tests.

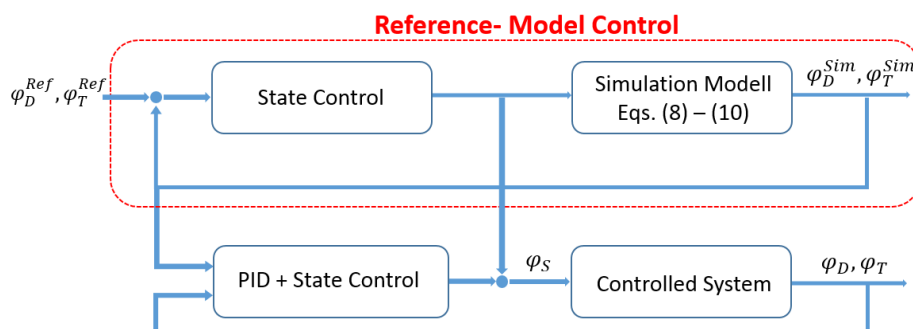


Figure 3: Schematic block diagram of control based on feedback linearization with a reference-model control

2.4 Basics and implementation of the nonlinear Model Predictive Control

The NMPC is one of few nonlinear control methods, it is e.g. described detailed in (GRÜNE & PANNEK, 2011). Compared with other nonlinear model based control methods, it has a less complicated design process. Especially, if the system model gets large with several or even many inputs and outputs. NMPC can handle with every model which consists of ordinary differential equation. But it has the challenges to guarantee a global optimum of the optimization problem because the formulation due to the nonlinear models do not lead to a convex optimization. Calculation within real-time requirements is another challenge. The mathematical unprovable stability of this control law is another drawback. The mathematical formulation of the NMPC optimization is defined as

$$\min J = \sum_{k=0}^{N-1} (\|x_{\text{ref}}(\mathbf{k}) - \mathbf{x}(\mathbf{k})\|_Q^2 + \|\mathbf{u}(\mathbf{k})\|_R^2) + \|x_{\text{ref}}(\mathbf{N}) - \mathbf{x}(\mathbf{N})\|_P^2 \quad (8)$$

subject to

$$\mathbf{x}_{\min} \leq \mathbf{x}(\mathbf{k}) \leq \mathbf{x}_{\max}, \quad \mathbf{k} = 0, \dots, N \quad (9)$$

$$\mathbf{u}_{\min} \leq \mathbf{u}(\mathbf{k}) \leq \mathbf{u}_{\max}, \quad \mathbf{k} = 0, \dots, N \quad (10)$$

$$\mathbf{x}(\mathbf{k}) = \mathbf{f}(\mathbf{x}(\mathbf{k} - 1), \mathbf{u}(\mathbf{k} - 1)), \quad \mathbf{k} = 0, \dots, N. \quad (11)$$

The inputs of the system $\mathbf{u}(\mathbf{k})$ are optimized so that the states $\mathbf{x}(\mathbf{k})$ have a minimal error to future reference values $x_{\text{ref}}(\mathbf{k})$. The observation into the future has a finite horizon by N steps. The main advantage of NMPC is regarding the Eqs. (5) and (6) the ability to consider constraints of system inputs \mathbf{u}_{\min} , \mathbf{u}_{\max} and states \mathbf{x}_{\min} , \mathbf{x}_{\max} into the optimization formulation. Due to model errors and disturbance a new optimization has to be executed at each sampling interval. Only the first optimized input vector $\mathbf{u}(0)$ is applied to the controlled system to get a closed loop control, this is called moving horizon.

The advantage of the NMPC is that every nonlinear model can be used, even there is no flat output. So, the Eqs. (8) - (10) can be used directly without any transformation. The system input u , i.e. desired steering angle, was restricted to the maximal physical limit of $\pm 35^\circ$. The steering angle φ_S does not have to be limited, because the steering is modeled as a first order lag element. It cannot overshoot and u is already restricted. For both system angles, the constraints are chosen as followed $|\varphi_D|, |\varphi_T| < 40^\circ$. For higher values of $|\varphi_D|, |\varphi_T|$ the trailer jackknives, i.e. the system gets into an unstable state. The control cannot push them afterwards to lower angles, so that the only option is to drive forward to get into a controllable state. The prediction steps N were chosen to 100 steps, so that at a driving velocity of $v_F = 0.3$ m/s and a sampling time of 0.2 s the prediction length yield to 6 m. Simulation tests showed that this highly prediction is necessary to get a stable control law.

2.5 Description of the simulation and test environment

Some details will follow in this subsection additional to **Fig. 1**. The simulation environment used was Gazebo (KOENIG & HOWARD, 2004), which has an interface to ROS (QUIGELY *et al.*, 2009). As middleware, ROS communicates with various software packages that were also used for on the test vehicle Fendt 724. The steering and drive are controlled here via a CAN interface. The C++ library ACADO Toolkit (HOUSKA, 2011) was used for the implementation of the NMPC. The library calculates the required matrices for the optimization offline, which otherwise have to be computed online. This is usually the bottleneck of a NMPC. The FBLC was designed in MATLAB/Simulink which has a ROS interface. As already mentioned, a MultiSense S21 was used as the stereo camera. A Xbox-Joystick was used to generate the reference angle between the drawbar and the trailer φ_T^{ref} .

3 Results

This section is divided into the simulation results in simulation and real vehicle tests. The simulation environment Gazebo is used to show the functioning of the control strategies and to preset the controller parameters. In the next step the same control parameters are applied on the Fendt 724 for real vehicle tests. As the parameters in the linear transfer function (see Eq. (7)) of the reference-control loop at the FBLC was chosen $\omega_0 = 0.12 \text{ s}$ and $D = 0.95$. Corresponding parameters for the disturbance control loop are $\omega_0 = 0.15 \text{ s}$ and $D = 0.95$. The weights for the NMPC were set for Eq. (8) as followed: weight for $\varphi_D = 1$, weight for $\varphi_T = 10$, terminal weight for $\varphi_D = 10$, terminal weight for $\varphi_D = 100$. For lower values for the weight φ_T the control has a low dynamic because the optimization have to deal with an error for $\varphi_T^{\text{ref}} - \varphi_T$ as well as an error for $\varphi_D^{\text{ref}} - \varphi_D$. The simulation results are illustrated in **Fig. 5**. The dynamic of the NMPC is much higher, because the control law can apply the maximal steering angle without getting into an open loop control. The steering angle φ_S oscillates yet which is bad regarding the driver's comfort. But both strategies are stable. The **Fig. 6** depicts the test results on the Fendt 724. For a pure reverse drive, the NMPC oscillates compared to the FBLC due to the excessive steering movements. At the step response, the NMPC shows a higher dynamic, as in the simulation, but an oscillation is also recognizable here. This is noticeable in the Fendt 724 and is at the expense of comfort.

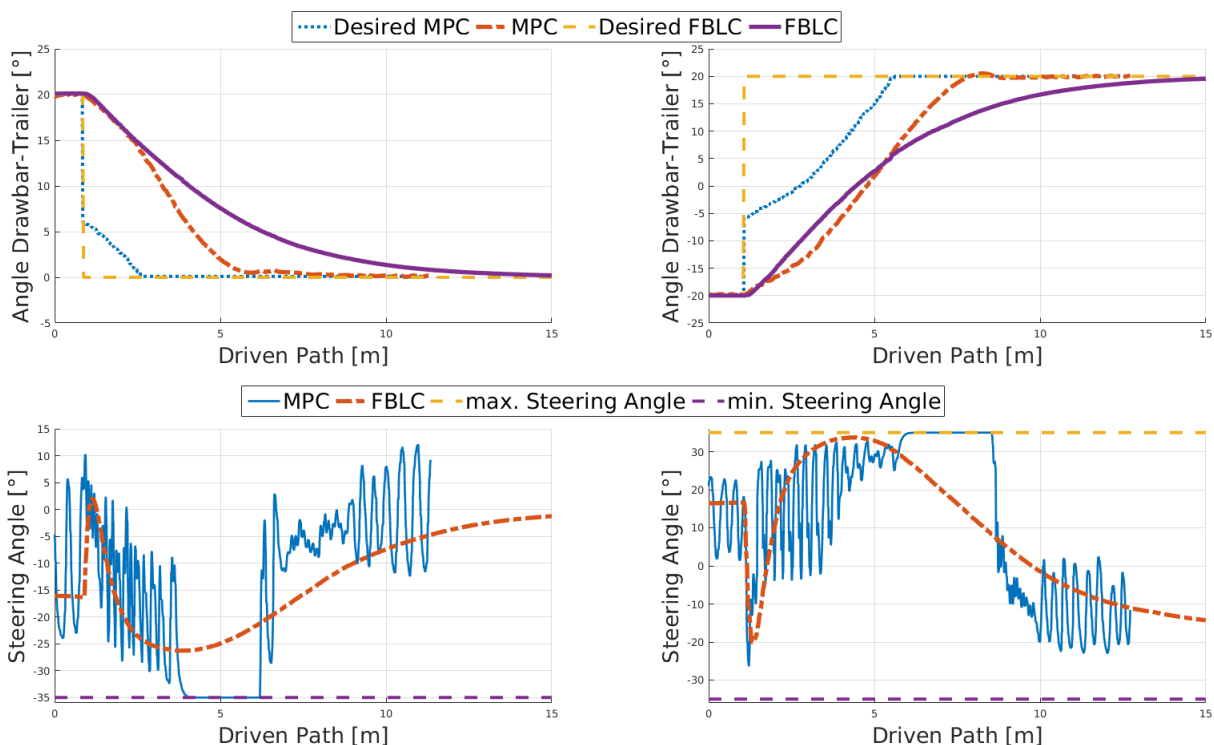


Figure 5: Simulation results of the model predictive control and the control based on feedback linearization

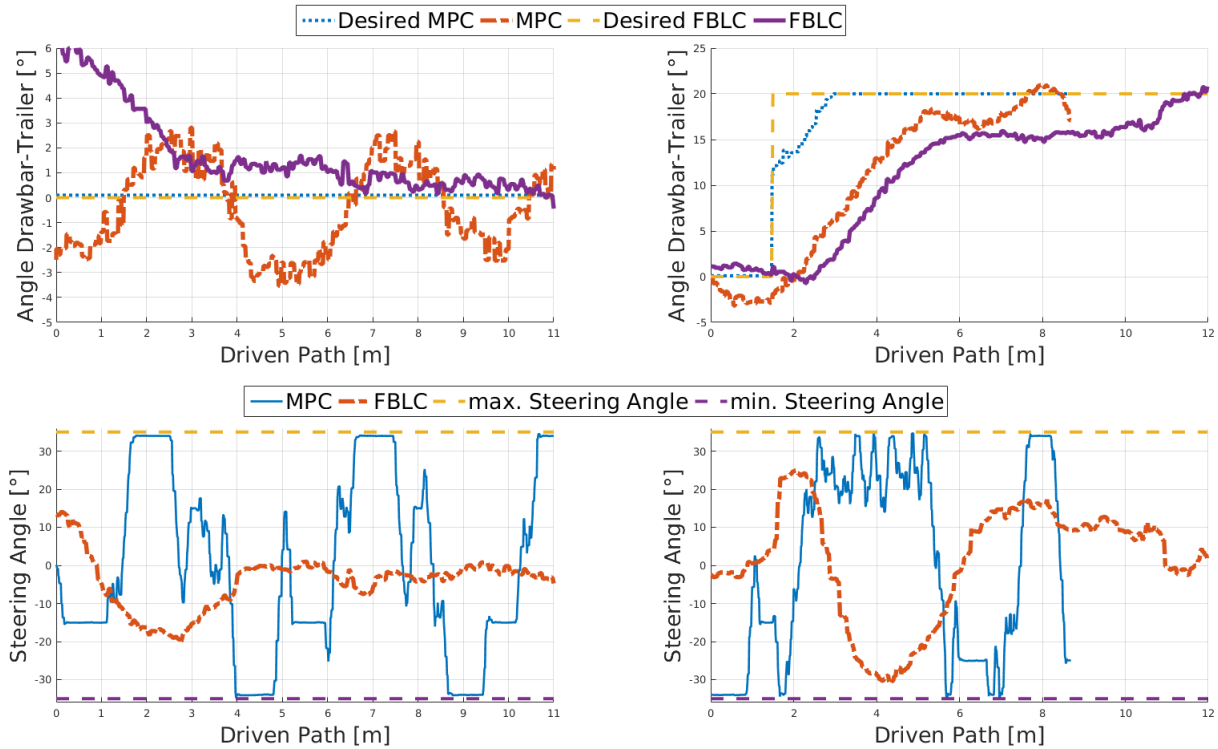


Figure 6: Test results on the test vehicle Fendt 724 of the model predictive control and the control based on the feedback linearization

4 Discussion and Conclusion

This paper shows the comparison of two controls for an assist system in which the driver can directly steer a full trailer. Firstly, a FBLC was implemented, moreover, a NMPC was built up which is not yet known in the literature. The NMPC showed in the simulation a significantly better control quality. In terms of dynamics, it could also be proven on the test vehicle Fendt 724. However, the developed NMPC has difficulties with pure reverse driving ($\varphi_T = 0$) and the steering oscillates intensive to the disadvantage of comfort. To improve the comfort, the project team tried to use the angular velocity as the system input in the NMPC and the angular velocity was weighted and constrained, so that the steps in the steering angle shrunk. With this additional state in the state space representation the calculation time was far too high to yet a stable control law with a high prediction horizon. If dynamics are more important than comfort, such as in a driverless transport system, then the NMPC has to be chosen over FBLC.

For an operator it is quite difficult to steer the vehicle-trailer combination into a garage or a hall in the simulation and real test environment. Because the dynamic of changing the angle between the drawbar and trailer φ_T is high, the operator has to predict this circumstance during the maneuvering. Even the NMPC is up to 50 % faster than the FBLC, the control loop dynamic is still too high. Only pure reverse driving is working satisfying, especially with the FBLC. In future it is conceivable tractor will have many cameras attached which can be used to realize this assistance system as an add-on module. Like in the automotive industry it is possible to implement the system by using

only a mono vision camera. To use angle sensors is an alternative solution but every trailer needs to be upgraded and the system is because of mechanical parts not wear-free. For parking the trailer into a hall or garage, it is more convenient to use a position control. The presented control strategies can be than used in a cascade control loop as the inner control loop.

Acknowledgment

The project was supported by funds of the German Government's Special Purpose Fund held at Landwirtschaftliche Rentenbank.

References

- BESL P, MCKAY ND (1992):** Method for registration of 3-D shapes. In: Sensor Fusion IV: Control Paradigms and Data Structures. *International Society for Optics and Photonics*: 586-607.
- BOLZERN P, DESANTIS RM, LOCATELI A (2001):** An input-output linearization approach to the control of an n-body articulated vehicle. *Journal of Dynamic Systems, Measurement, and Control* 123(3): 309-316.
- CHIU J, GOSWAMI A (2012):** Driver assist for backing-up a vehicle with a long-wheelbase dual-axle trailer. International Symposium on Advanced Vehicle Control (AVEC). Seoul, Korea: KSAE.
- GRÜNE L, PANNEK J (2011):** Nonlinear model predictive control. *Nonlinear Model Predictive Control*. Springer, London, 43-66.
- HOUSKA B, FERREAU HJ, DIEHL M (2011):** ACADO toolkit—An open-source framework for automatic control and dynamic optimization. *Optimal Control Applications and Methods* 32(3): 298-312.
- ISIDORI A (2013):** Nonlinear control systems. Springer Science & Business Media.
- KOENIG N, HOWARD A (2004):** Design and use paradigms for gazebo, an open-source multi-robot simulator. Proceedings of 2004 IEEE/RSJ International Conference on Intelligent Robots and Systems (IROS 2004): 2149-2154.
- LAUMOND JP (1993):** Controllability of a multibody mobile robot. *IEEE Transactions on Robotics and Automation* 9(6): 755-763.
- QUIGLEY M, GERKEY B, CONLEY K, FAUST J, FOOTE T, LEIBS J, BERGER E, WHEELER R, NG A (2009):** ROS: an open-source Robot Operating System. ICRA workshop on open source software: 5.
- SKLYARENKO Y, SCHREIBER F, SCHUMACHER W (2013):** Maneuvering assistant for truck and trailer combinations with arbitrary trailer hitching. IEEE International Conference on Mechatronics (ICM): 774-779.

Adaptive Control for Guidance of Tracked Vehicles

Otto Lerke, Volker Schwieger

*Institute of Engineering Geodesy, Geschwister-Scholl-Str. 24D, 70174 Stuttgart, Germany
E-Mail: otto.lerke@iigs.uni-stuttgart.de, volker.schwieger@iigs.uni-stuttgart.de*

Abstract: During vehicle guidance operations in alternating conditions conventional controller types as e.g. PID- or Fuzzy-controllers may not perform properly due to their constant parameter settings. To counteract these adverse effects adaptive controllers can be used instead. Adaptive controllers are capable to automatically adjust their behavior according to the set requirements on guidance quality. This work investigates the performance of a self-tuning controller (STC). The structure of the STC has some modifications in comparison to a conventional closed-loop system. These modifications are represented by two additional steps during the loop run, namely system identification and control calculation. The identification step is solved with the widespread recursive least square algorithm, which has real-time capability. The control calculation step is based on the identification step and aims at the provision of the regulating variable for the closed-loop system. Compared to the PID-controller the results show a slightly worse guidance performance of the adaptive controller for laboratory conditions. Whereas, the results for outdoor-scenarios indicate improved guidance performance of the adaptive controller compared to the PID-controller.

Key words: closed-loop systems, adaptive control, self-tuning controllers, recursive least squares algorithm

1 Introduction

Automation plays an important role on construction sites. Automation also yield benefits regarding the reduction of expenses and the increase of efficiency and product quality e.g. in road construction and maintenance (KILPELÄINEN *et al.*, 2011). Construction machines can be categorized under aspects of their application field, as e.g. transportation, roadworks or earthworks (KÜHN, 1991). Furthermore construction machines can be divided into two main categories according to their chassis design, namely into wheeled chassis and tracked chassis (GEBHARD, 2010). This investigation examines the performance of automatically controlled tracked vehicles using an adaptive controller.

The automatic control may be established by designing a closed-loop system, which controls a vehicle in such a way that it follows a predefined reference trajectory. Different controller types can be used within the closed-loop system aiming to minimize the difference between the current machine's position and the desired position, expressed by the reference trajectory (MANN *et al.*, 2005). Such controllers are e.g. 2-, 3- point controllers, PID- or Fuzzy-controllers. When using these conventional controller types the

main challenge is the individual controller tuning procedure. Each controller type needs a set of parameters to ensure optimal control operation. These parameters must be tuned in advance for each particular operational scenario. Hence, in alternating environmental conditions the parameters need to be retuned and reset in order to keep the control quality at a desirable level. To overcome this disadvantage an adaptive controller has to be applied instead.

In particular alternating operational conditions the adaptive controller adjusts automatically in such a manner, that the set requirements on control quality are kept. According to ÅSTRÖM (1983) there are three main adaptive control schemes: gain scheduling, model-reference adaptive control (MRAS) and self-tuning controllers (STC). This work examines the performance of a self-tuning controller which is used to control a model crawler at scale 1:14.

2 Methods

The starting point of the STC design is an ordinary closed-loop system, where the feedback signal is processed within the controller in order to minimize the control deviation. The feedback control loop is extended by an additional functionality which identifies the controlled process by the use of its input and output. This part, called the “process identification” (ÅSTRÖM & WITTENMARK, 1989), is the base for calculations of the controller properties, respectively the controller parameters. **Fig. 1** depicts the general scheme of the STC. Table 1 summarizes the variables of the extended closed-loop, as well as their appropriate meaning within the guidance algorithm of the model crawler.

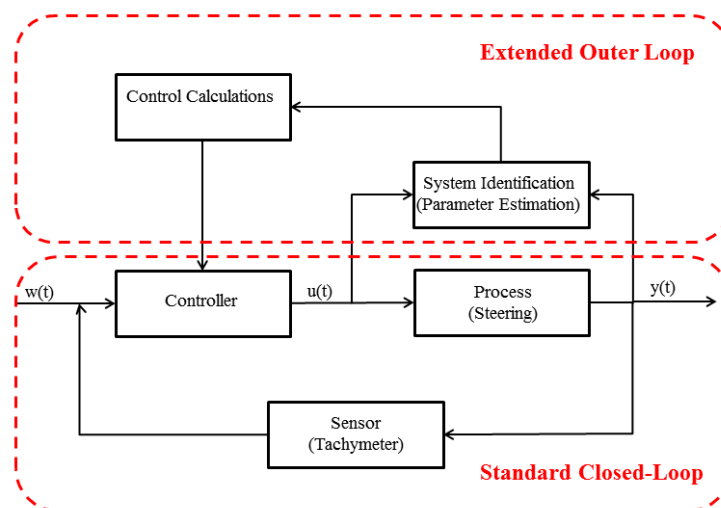


Figure 1: General STC Scheme according to SEBORG *et al.* (1986)

Hence, to achieve adjustable control two steps have to be performed (SEBORG *et al.*, 1986): system identification and control calculations.

Within the scope of this work the adjustable control affects the lateral control of the vehicle, moving on a predefined reference track with a constant velocity. The 360° prism, which is part of the sensor system, is mounted in the anticipated computation point (ACP), located 7 cm in front of vehicle's center of gravity. This causes a position calculation for an earlier point in time and helps to compensate dead time (BEETZ, 2012). The lateral control is realized by the design of an appropriate steering method introduced by LERKE & SCHWIEGER (2017). The approach is based on the kinematic model for tracked vehicles according to LE (1991), where the equation which describes the relationship between the driven radius and different velocities for the left track v_l and right track v_r has been modified and solved in a way that a scaling factor n , embedded within two scaling terms, could be derived. Based on the equation for the total velocity of a tracked vehicle $v_{total} = \frac{1}{2} \cdot (v_l + v_r)$, the following two expressions for the velocities of the left and right track could be determined:

$$v_l = v_{total} \cdot \frac{2 \cdot n}{1+n}, \quad (1)$$

$$v_r = v_{total} \cdot \frac{2}{1+n}. \quad (2)$$

In equations (1) und (2) the scaling terms are represented by expressions $\frac{2 \cdot n}{1+n}$ and $\frac{2}{1+n}$.

Table 1 summarises the variables of the STC and their meaning within the guidance algorithm.

Table 1

Variable	Meaning within the STR scheme	Meaning within the guidance algorithm
$w(t)$	Reference variable	Reference trajectory, represented by series of reference positions
$u(t)$	Regulating variable	Steering parameter, represented by scaling factor n
$y(t)$	Controlled variable	Current vehicle's position

2.1 System Identification

The system identification step can be classified as an implicit approach, because the process model is converted to a predictive form that allows the future process model output to be calculated from current and past values of the input and output variables (SEBORG *et al.*, 1986). The online parameter estimation, related to the identification step, is based on a linear single input - single output (SISO) system, expressed as linear difference equation in the shape of ARMA (autoregressive moving average) model (TEUSCH, 2006, NEUNER, 2008). SEBORG *et al.* (1986) formulates the SISO system as ARMAX (autoregressive moving average model with auxiliary or exogenous input), which is written as follows:

$$y(t) + a_1 y(t-1) + \dots + a_n y(t-n) = b_0 u(t-k) + b_1 u(t-k-1) + \dots \\ \dots + b_m u(t-k-m) + c_0 \xi(t) + c_1 \xi(t-1) + \dots + c_n \xi(t-n) + d(t) \quad (3)$$

y - controlled variable,

u - regulating variable,

ξ - stochastic noise,

d - disturbance variable (not measured),

$a_1, \dots, a_n, b_0, \dots, b_m, c_0, \dots, c_n$ - model parameters.

As a simplification for further considerations we suppose the noise parameters c_i and disturbance d in (3) are set to zero.

The aim of the identification step is to establish a model, based on model parameter estimates \hat{a}_i, \hat{b}_i , from a given data record. The estimation is carried out in real time, due to the dynamic behavior of the system. One of the common real-time estimation methods is the recursive least squares algorithm (RLS), proposed by e.g. ÅSTRÖM & WITTENMARK (1989) or WANG & TANG (2014). The RLS can be understood as a special case of the recursive Kalman filter (ÅSTRÖM, 1983). The algorithm is suitable for real-time estimates of the parameters by the use of their iteration-wise update.

Hence, equation (3) can be rewritten as:

$$y(t) = \boldsymbol{\psi}^T(t-1) \cdot \boldsymbol{\theta}(t-1) \quad (4)$$

with

$\boldsymbol{\psi}$ - regressor vector, shaped as

$$\boldsymbol{\psi}(t-1) = [y(t-1) \ y(t-2) \ \dots \ y(t-n) \ u(t-1) \ u(t-2) \ \dots \ u(t-n)]^T,$$

$\boldsymbol{\theta}$ - parameter vector, shaped as

$$\boldsymbol{\theta}(t-1) = [a_1 \ a_2 \ \dots \ a_n \ b_1 \ b_2 \ \dots \ b_n].$$

The set of equations for the RLS according to SEBORG *et al.* (1986) is represented by (5):

$$\begin{aligned} \hat{\boldsymbol{\theta}}(t) &= \hat{\boldsymbol{\theta}}(t-1) + \mathbf{K}(t) \cdot \varepsilon(t) \\ \varepsilon(t) &= y(t) - \boldsymbol{\psi}^T(t-1) \cdot \hat{\boldsymbol{\theta}}(t-1) \\ \mathbf{K}(t) &= \mathbf{P}(t-1) \cdot \boldsymbol{\psi}(t-1) \cdot (\lambda + \boldsymbol{\psi}^T(t-1) \cdot \mathbf{P}(t-1) \cdot \boldsymbol{\psi}(t-1))^{-1} \\ \mathbf{P}(t) &= \frac{1}{\lambda} \cdot [(\mathbf{I} - \mathbf{K}(t) \cdot \boldsymbol{\psi}^T(t-1)) \cdot \mathbf{P}(t-1)] \end{aligned} \quad (5)$$

\mathbf{K} – Kalman filter gain matrix,

\mathbf{P} – covariance matrix of the estimator error,

\mathbf{I} – identity matrix,

λ – weighting factor,

ε – estimation error.

The weighting factor λ is introduced to maintain the algorithm's sensitivity to variations of the process parameters. In case of $\lambda = 1$ all data is weighted equally, whereas for $0 < \lambda \leq 1$ more weight is placed on recent than on older data (SEBORG *et al.*, 1986).

By the use of (5) the estimation of the model parameters \hat{a}_i, \hat{b}_i is now possible.

2.2 Control Calculations

The simplified ARMAX model equation (3) can further be rewritten as follows (ÅSTRÖM & WITTENMARK, 1989):

$$\mathbf{A} \cdot y = \mathbf{B} \cdot u, \quad (6)$$

where \mathbf{A} and \mathbf{B} are matrices, containing the parameters a_i, b_i . Equation (6) represents the identification step. To convey a link from the identification step to the control calculation step, according to figure 1, the rule for the controller is introduced. The general linear controller is expressed by equation (7) (ÅSTRÖM & WITTENMARK, 1989):

$$\mathbf{R} \cdot u = \mathbf{T} \cdot w - \mathbf{S} \cdot y, \quad (7)$$

where \mathbf{R}, \mathbf{T} and \mathbf{S} are matrices, containing the parameters r_i, t_i and s_i . In order to calculate the regulating variable u the matrices \mathbf{R}, \mathbf{T} and \mathbf{S} have to be solved. To do so, the following closed-loop system equations can be established by the use of (6) and (7), where u is eliminated:

$$y = \frac{\mathbf{B} \cdot \mathbf{T}}{\mathbf{A} \cdot \mathbf{R} + \mathbf{B} \cdot \mathbf{S}} \cdot w, \quad (8)$$

$$u = \frac{\mathbf{A} \cdot \mathbf{T}}{\mathbf{A} \cdot \mathbf{R} + \mathbf{B} \cdot \mathbf{S}} \cdot w. \quad (9)$$

In the next step the dominator of (8) and (9) is set to zero and equation (10) results:

$$\mathbf{A} \cdot \mathbf{R} + \mathbf{B} \cdot \mathbf{S} = \zeta \quad (10)$$

$$\zeta \in \mathbb{Z}.$$

Equation (10) is known as Diophantine equation and is defined as the closed-loop characteristic polynomial (ÅSTRÖM & WITTENMARK, 1989). With known matrices \mathbf{A} and \mathbf{B} from the identification step, \mathbf{R} and \mathbf{S} can be obtained by solving the Diophantine equation (10), e.g. by the use of the Euclidean algorithm (OSWALD & STEUDING, 2015). The last unknown matrix \mathbf{T} in (7) can be derived by the use of equation (8). It follows from (8) that the gain from the reference variable w to the output signal y is static in each iteration. Thus the relationship (11) is valid (ÅSTRÖM & WITTENMARK, 1989):

$$\frac{\mathbf{B} \cdot \mathbf{T}}{\mathbf{A} \cdot \mathbf{R} + \mathbf{B} \cdot \mathbf{S}} = \frac{\mathbf{T}}{\mathbf{S}}. \quad (11)$$

In the simplest configuration this gain would be:

$$\frac{\mathbf{T}}{\mathbf{S}} = 1. \quad (12)$$

Hence, one can set $T = S$.

Now the regulating variable can be obtained by reshaping equation (7) as follows:

$$u = \frac{T}{R} \cdot w - \frac{S}{R} \cdot y \quad (13)$$

2.3 Current Realization of the Controller for Guidance Operations

For the current realization of the controller a system model with polynomials of second order has been chosen. This decision was made under aspects of an adequate system model description and, on the other hand, a reasonable computational effort. SEBORG *et al.* (1986) propose polynomial orders between 2 and 3. Moreover a direct self-tuning regulator according to ÅSTRÖM & WITTENMARK (1989) has been applied. The term “direct” is justified by the fact that the plant parameters and the control parameters are estimated directly. To do so equation (4) has been reparameterized in terms of the controller parameters:

$$y^*(t) = \psi^T(t-1) \cdot \theta^*(t-1) \quad (14)$$

The parameter vector in (14) is defined as:

$$\theta^*(t-1) = [r_1 \ r_2 \ s_1 \ s_2].$$

The obtainment of θ^* , respectively the matrices R and S is carried out by the RLS algorithm presented in chapter 2.1. Then, after setting $T = S$, the general control law (7) can be applied for the calculation of the regulating variable u according to (13).

Fig. 2 depicts the applied direct self-tuning controller scheme.

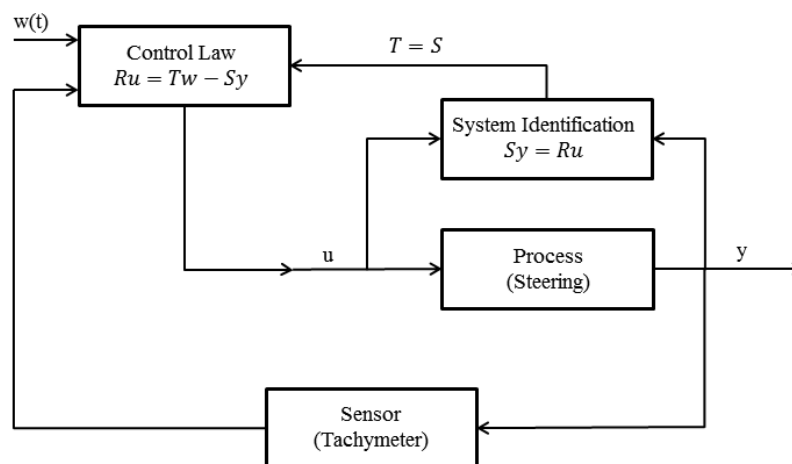


Figure 2: Direct STC Scheme

For the provision of the RLS algorithm initial values for r_1 , r_2 , s_1 , s_2 , P , y and u must be selected. These values were set as follows:

$$r_1(0) = 1 \cdot 10^{-3}, r_2(0) = 1 \cdot 10^{-3}, s_1(0) = 1 \cdot 10^{-3}, s_2(0) = 1 \cdot 10^{-3}, y(0) = 1, u(0) = 1,$$

$$P(0) = \begin{bmatrix} 1 \cdot 10^3 & 0 & 0 & 0 \\ 0 & 1 \cdot 10^3 & 0 & 0 \\ 0 & 0 & 1 \cdot 10^3 & 0 \\ 0 & 0 & 0 & 1 \cdot 10^3 \end{bmatrix}.$$

The values for $r_1(0)$, $r_2(0)$, $s_1(0)$, $s_2(0)$, $y(0)$ and $u(0)$ have been chosen randomly. The elements p_{ii} of the covariance matrix $P(0)$ have been chosen large, in order to let the confidence in the estimate $\hat{\theta}^*(0)$ be poor. Examinations of the RLS performance have shown, that setting large initial values implies rapid changes of $\hat{\theta}^*$, whereas small values for p_{ii} let $\hat{\theta}^*$ change slowly.

3 Implementation and Experimental Setup

To investigate and analyze the performance of the adaptive controller, driving experiments have been conducted. For this purpose the construction machine simulator, operated by the Institute of Engineering Geodesy, has been used. The simulator has been developed to test and evaluate the performance of different sensors, as well as filter and control algorithms (GLÄSER, 2007; BEETZ, 2012). The simulator, in the current configuration, consists of a crawler model at scale 1:14 with a step-less drive, a control computer, an analogue-digital converter and a remote control. The sensor, in the feedback branch of the STC in figures 1 and 2, is a Leica TS 30 robot tachymeter with an accuracy of 3 mm + 1 ppm in kinematic mode (LEICA, 2018). The hardware components and their interaction are shown in **fig. 3**.

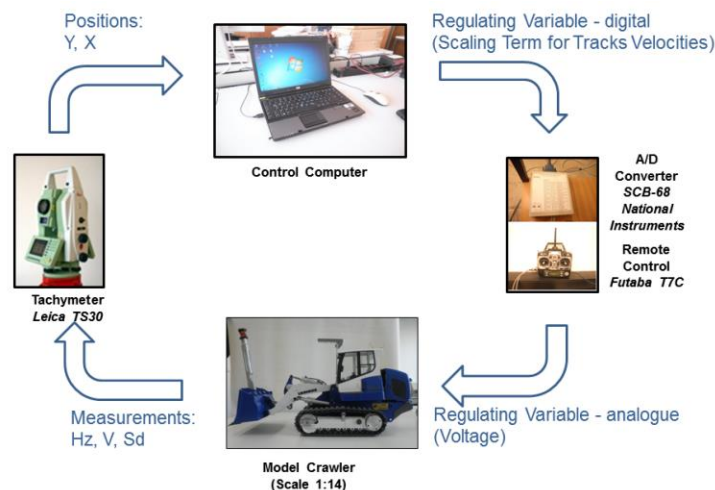


Figure 3: Hardware Components (LERKE & SCHWIEGER, 2017)

The interaction in **fig. 3** is as follows: the tachymeter measures the position of the prism, mounted in the ACP of the crawler model and sends it to the control computer. The computer calculates the perpendicular distance/ lateral deviation between the crawler's position and the reference trajectory. Based on this information, the algorithm calculates the regulating variable, expressed in the form of the steering angle, respectively the ap-

appropriate track velocity differences, to get the crawler back on the reference trajectory as fast as possible. The information is passed to the remote control via A/D converter, which subsequently sends the voltages to the driving actuators of the crawler. The self-tuning controller is running on the control computer, where the variable $w(t)$ represents the reference trajectory and the variable $y(t)$ the position, measured by the tachymeter.

The evaluation has been carried out by comparing the reference trajectory with the effectively driven trajectory and the subsequent calculation of the lateral deviations and their root mean square RMS according to BEETZ & SCHWIEGER (2012).

$$RMS = \sqrt{\frac{\sum_{i=1}^n e_i^2}{n}} \quad (16)$$

e_i – lateral deviation,

n – number of measurements.

Exemplarily, four driving experiments have been conducted. The first and the second experiment should show the general functionality of the STC. These experiments took place in non-alternating operational environment under laboratory conditions. For the drives two perfectly defined and shaped trajectories in form of an oval and an eight have been chosen as references. The trajectories consist of the main route design elements as clothoids, curves and straight lines. The third and the fourth experiment took place under variable conditions of outdoor scenarios. These drives have been conducted on two freely shaped trajectories, with changing and randomly tilted driving underground. Thereby the underground sections changed from paving stones to gravel, varying in shape and size. The four experimental trajectories are depicted in **fig. 4**.

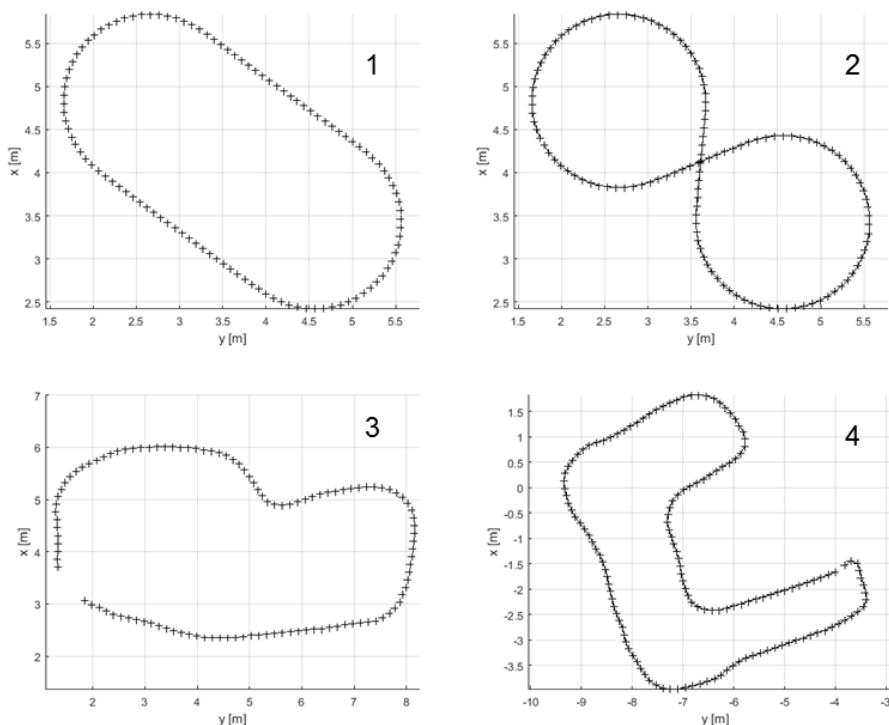


Figure 4: laboratory trajectories (1 and 2); outdoor trajectories (3 and 4)

For each trajectory one single lap has been completed. To classify the performance in both scenarios the assessment includes a comparison with a consummately tuned PID-controller. The PID controller parameters have been determined as follows: $P = 200$, $T_n = 0,4 \text{ min}$, $T_v = 0,003 \text{ min}$.

4 Results

Table 2 depicts the numerical results of the test drives in non-alternating laboratory environment. According to the RMS values one can say that the performance of both controllers is nearly the same. The slight differences of 0.5 mm for trajectory 1 and 0.9 mm for trajectory 2 are beneath the measurement accuracy of the used robot tachymeter.

Table 2: RMS values for the laboratory experiments

Trajectory	Self-tuning controller (STC)	PID controller
1 (oval)	0.0023 m	0.0018 m
2 (eight)	0.0037 m	0.0028 m

Fig. 5 and **6** show the lateral deviation data collected during the laboratory experiments.

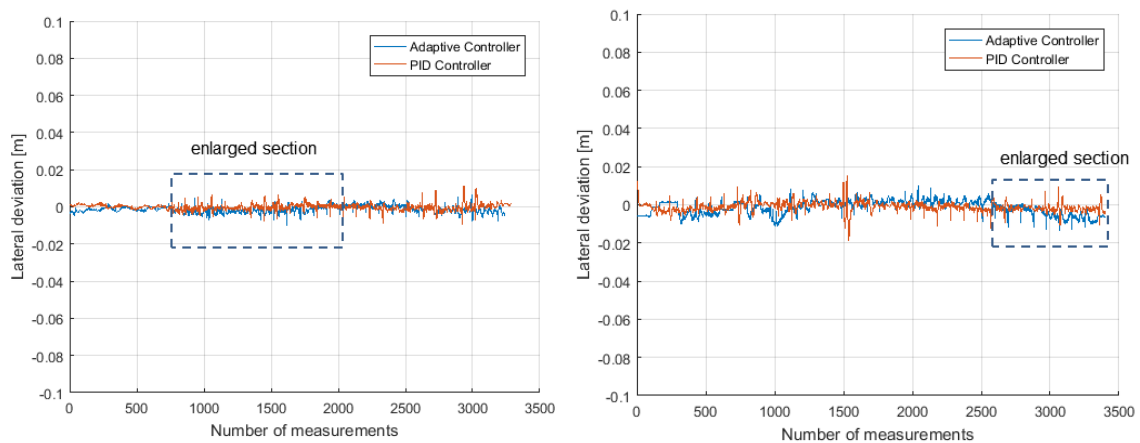


Figure 5: laboratory experiments: lateral deviations for trajectory 1 (left) and trajectory 2 (right)

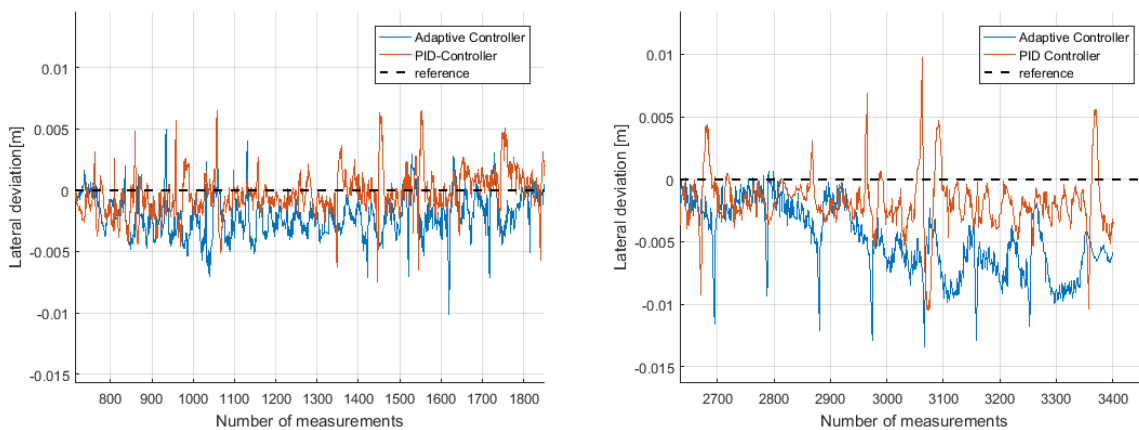


Figure 6: enlarged sections of figure 5; left trajectory 1; right trajectory 2

As can be seen in **Fig. 5** and **6** the STC needs some adjustment time to operate optimally, whereas the control impact of the PID-controller immediately occurs. **Fig. 5** and **6** show that the lateral deviations of the STC are greater than that of the PID-controller during curve drives. This can be explained by the characteristic of the STC. The permanently changing reference variable w during the curve drive affects the convergence of the system's identification parameters r_i, s_i . It seems that the settling time of the parameter estimation is little too long and therefore the system state is not optimally identified, which consequently has a negative impact on the control calculation. Though, the investigation on this behavior is outside the scope of this contribution.

The RMS values for the outdoor experiments indicate a better performance of the adaptive controller (**table 3**). The difference in the control quality is 4.2 mm for trajectory 3 and 1.4 mm for trajectory 4. However the value of 1.4 mm is beneath the tachymeter measurement accuracy as well.

Table 3: RMS values for the outdoor experiments

Trajectory	Self-tuning controller (STC)	PID controller
3	0.0089 m	0.0131 m
4	0.0072 m	0.0086 m

Fig. 7 shows the lateral deviation data collected during the outdoor experiments.

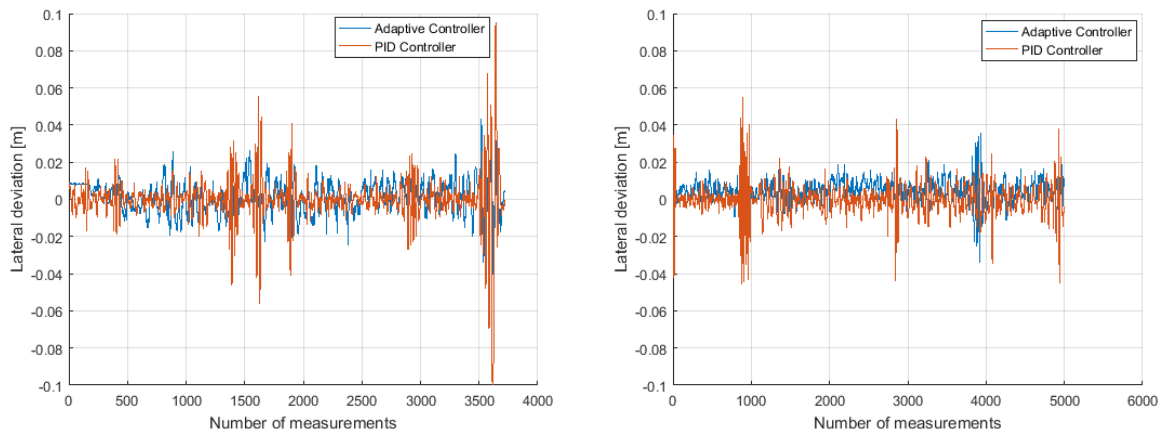


Figure 7: outdoor experiments: lateral deviation for trajectory 3 (left) and trajectory 4 (right)

The courses of the lateral deviation indicate large oscillations of the PID controlled drives after experienced disturbances, caused by sudden changes of the underground.

Due to the fact that only single laps have been driven on each trajectory, no learning effect of the adaptive controller could be observed.

5 Conclusion and Outlook

An adaptive control scheme has been applied in order to guide a tracked vehicle on a predefined trajectory. It has been shown how a self-tuning controller can be used within an automation closed-loop. The guidance performance of the self-tuning controller, with a RMS between 2.3 mm and 3.7 mm for non-alternating indoor scenarios and between 7.2 mm and 8.9 mm for alternating outdoor scenarios, can be regarded as satisfactory. Compared with the performance of the PID controller one can say, that the PID-controller shows slightly better results under laboratory conditions. However in the non-optimal outdoor scenarios, the adaptive controller seems to be superior. Though, it must be considered that the STC needs some settling time, before the optimal control performance is achieved.

In summary one can say that the great advantage of adaptive controllers in comparison with conventional controller types is the non-necessity of excessive, time-consuming tuning procedures and a seemingly better performance in alternating driving environments.

In the future it is worth to extend the system model by the noise parameters and disturbances for the purpose of performance enhancement. The negative effect on control calculation due to slow parameter settling must be analyzed and further investigations must be conducted to verify the achieved results of this contribution. Moreover hybrid controller schemes are conceivable, where a PID-controller and the STC are merged in a way, that the PID-controller is active until the STC parameters adjust and thereafter the STC takes over the control. Finally, the introduction of new concepts for test scenarios should help to illuminate further aspects of the adaptive control in the context of ma-

chine guidance. Additionally the longitudinal adaptive control of the vehicle must be implemented to set up a 3-D guidance system.

References

- ÅSTRÖM KJ (1983):** Theory and Applications of Adaptive Control – A Survey. *Automatica* 19(5). DOI: 10.1016/0005-1098(83)90002-X.
- ÅSTRÖM KJ, WITTENMARK B (1989):** Adaptive Control. Addison-Wesley Publishing Company, Reading Massachusetts, Menlo Park California, New York, Don Mills Ontario, Wokingham England, Amsterdam, Bonn, Sydney, Singapore, Tokyo, Madrid, San Juan.
- BEETZ A (2012):** Ein modulares Simulationskonzept zur Evaluierung von Positionssensoren sowie Filter- und Regelalgorithmen am Beispiel des automatisierten Straßenbaus. Bayerische Akademie der Wissenschaften, Verlag C. H. Beck, DGK, Reihe C, Heft Nr. 688.
- BEETZ A, SCHWIEGER V (2013):** Automatic lateral control of a dozer. *Journal of Applied Geodesy*, Heft 4, de Gruyter.
- GLÄSER A (2007):** Modulares System zur Automatisierung hochgenauer geometrischer Positionierung und Bahnführung im Bauwesen. Dissertation am Institut für Anwendungen der Geodäsie im Bauwesen, Universität Stuttgart, elektronische Publikation: <http://dx.doi.org/10.18419/opus-3746>. Letzter Zugriff: 04.06.2018.
- GEBHARD N (2010):** Fluidtechnik in Kraftfahrzeugen. Springer Verlag Berlin Heidelberg.
- KILPELÄINEN P, JAAKKOLA M, ALANAATU P (2011):** Development of a Control System for a Multipurpose Road Repairing Machine. *Automation in Construction* Volume 20. ISSN: 0926-5805.
- KÜHN G (1991):** Handbuch Baubetrieb: Organisation-Betrieb-Maschinen. Springer Verlag Berlin Heidelberg.
- LE AT (1991):** Modelling and Control of Tracked Vehicles. Doctoral Thesis University of Sidney. Electronic Publication, www.cas.edu.au/download.php/Le1999-PhDThesis.pdf?id=1222. Last Access: 14.04.2015.
- LEICA GEOSYSTEMS (2018):** [http://w3.leica-geosystems.com/downloads123/zz/tps/ts30/brochures-datasheet / ts30_technical_data_de.pdf](http://w3.leica-geosystems.com/downloads123/zz/tps/ts30/brochures-datasheet/ts30_technical_data_de.pdf). Last Access: 09.05.2018.
- LERKE O, SCHWIEGER V (2017):** Steering Method for Automatically Guided Tracked Vehicles. V. FIG Working Week 2017, Helsinki, Finland.
- MANN H, SCHIFFELGEN H, FRORIER P (2005):** Einführung in die Regelungstechnik. 10. Auflage, Carl Hanser Verlag, München Wien.
- NEUNER HB (2008):** Zur Modellierung und Analyse instationärer Deformationsprozesse. Bayerische Akademie der Wissenschaften, Verlag C. H. Beck, DGK, Reihe C, Heft Nr. 616.
- OSWALD N, STEUDING J (2015):** Elementare Zahlentheorie – Ein sanfter Einstieg in die höhere Mathematik. Springer Verlag 2015. ISBN: 978-3-662-44247-0.
- SEBORG DE, EDGAR TF, SHAH SL (1986):** Adaptive Control Strategies for Process Control – A Survey. *AIChE Journal* 32(6). DOI: 10.1002/aic.690320602.
- TEUSCH A (2006):** Einführung in die Spektral- und Zeitreihenanalyse mit Beispielen aus der Geodäsie. Bayerische Akademie der Wissenschaften, Verlag C. H. Beck, DGK, Reihe A, Heft Nr. 120.
- WANG C, TANG T (2014):** Recursive Least Squares Estimation Algorithm Applied to a Class of Linear-in-Parameters Output Error Moving Average Systems. *Applied Mathematics Letters* Volume 29. DOI: 10.1016/j.aml.2013.10.011.

Towards motor control adjustment with inertial sensor measurements for small differential drive robots

David Reiser¹, Marvin Hubl², Hans W. Griepentrog¹

¹University of Hohenheim, Institute of Agricultural Engineering, Garbenstr. 9, D-70599 Stuttgart, Germany

²University of Hohenheim, Chair of Information Systems II, D-70599 Stuttgart, Germany

E-mail: dreiser@uni-hohenheim.de

Abstract: Small robots can play an important role in saving agricultural productivity in future when they are able to navigate efficiently in a semi-structured agricultural environment. Different underground types, soil roughness and compaction levels can make it hard for these small robots to work reliably. For each environment, the control strategy must be adjusted correctly to be energy sufficient and successful. However, this requires detection of the surface characteristics and knowledge about the robot behavior. In this research, the inertial sensors of a small four-wheeled differential drive robot were used. The robot was equipped with an inertial measurement unit (IMU), encoders and an ampere meter at each of the four wheel motors. The robot was manually guided over three different surfaces: concrete, compacted sand and linoleum. The robot drove straight with constant speed and afterwards performed a headland turn, following a typical pattern for agricultural robot navigation. It was possible to detect the different surface types by analyzing the IMU and the power consumption of the motors. This could help to enhance self-control and guidance for small autonomous robots without external sensors.

Key words: inertial sensors, IMU, terrain classification, robots, differential drive, agriculture

1 Introduction

Modern agricultural machines are increasingly automated. In future there might be autonomous machines on fields, operating without human intervention. Especially object recognition (VÁZQUEZ-ARELLANO *et al.*, 2016) and navigation (BECHAR & VIGNEAULT, 2016), (REISER *et al.*, 2017) are in the research focus for agricultural robotics. However, actual behavior often deviates from desired behavior. Reasons are environmental uncertainty and dynamics which are hard to control. Field Robots have to handle varying conditions in time and space. The underground of a site may be loose at one place and compacted at another one. It may be dusty today and wet the other day. When applying false assumptions about present environmental conditions, modelled behavior tends to mismatch with the actual behavior. One example could be the actuator control of a robot, which was aligned for compacted and dry soil, while the real situation differs from

this assumption. Mismatches between modelled behavior and actual behavior are a typical source of hazards (LEVESON, 2011). Autonomy of the robots amplifies these hazards because no human intervention adjusts for these mismatches. In the worst cases, the robots get stuck or damage the plants. An autonomous robot needs to be able to retrieve relevant knowledge about its current state, without explicit human inputs. This can relate to several aspects, like space, or integrity. For example, some robots are required to identify the damages of itself (REINA *et al.*, 2015). With respect to space, agricultural robots often use a satellite-based positioning method which makes them dependent on other systems. Robots could use odometry instead, to remain independent from external systems. However, these internal measurements are dependent on environmental variables. Therefore, the robots need to apply reasoning about the environment and itself. To control a wheeled field robot through varying terrain, the robot is required to have knowledge about the actual underground conditions. This requirement is of particular importance for precise turning lanes, typical for agricultural applications.

There are considerable achievements in visual underground identification (KHAN & KOMMA, 2011; ZENKER *et al.*, 2013; ZOU *et al.*, 2014). However, visual sensors can fail in detecting undergrounds, especially when there are changing light conditions. Internal sensors (sensors monitoring the internal state of the machine like power consumption or wheel movement) could be shielded from exogenous impacts. To interpret the sensor perceptions, it is necessary to put them in the right context. Existing underground detection methods with internal sensors are mostly vibration-based and use machine learning classifiers, like support vector machines, or artificial neural networks (BROOKS & IAGNEMMA, 2005; DUPONT *et al.*, 2006, 2008; OJEDA *et al.*, 2006; WEISS *et al.*, 2006). Different underground classes produce distinct vibration signatures which can be recognized by a trained classifier.

The overall objective of our research is to improve the navigation of small autonomous field robots. Particularly by appropriately controlling its wheels with respect to the underground. We seek to find a method for underground detection based on an explicit model for enhancing self-control and pose the research question: How can a wheeled robot detect relevant underground conditions by just using its internal perceptions of acceleration and applied current to its wheel motors?

2 Materials and Methods

2.1 Model for Underground Detection with a small Wheeled Field Robot

In this research, the reasoning about the robot's current state in the environment is split into two parts. The first part relates the sensor inputs to a static environmental model of the robot. The static model contains non-changing facts and reflects assumptions. Essentially, the static model should be represented on a level which is sufficient for the robot's purposes. In most machine learning reasoning, like artificial neural networks, the causal dependencies that lead from an input variable to an output variable are unknown. We try to represent static relationships explicitly, allowing to map an input varia-

ble to an output variable. Reasoning on the sensor inputs combined with the static environmental model results in a dynamic environmental model. The situation is detected by the sensor inputs of the robot.

The self-control model of the robot is as follows: The robot applies energy to its motor controllers and therewith drives its wheels. How the driving of the wheels affects the actual spatial movement of the robot depends on the underground, most crucially characterized by the grip. Physically, the actual spatial movement of the robot is associated with an acceleration, which can be measured by the inertial measurement unit (IMU) of the robot. The IMU delivers measured accelerations which occur at the vehicle. The extent to which an underground translates energy applied to the motor controllers into spatial movement depends on the grip of the underground. Terrain with low grip induces more slippage. We assume grip as the most relevant terrain characteristic and expect underground distinction by grip to be sufficient.

In the study at hand, we focus on three exemplary underground classes: concrete, compacted sand and linoleum. We formulate the following hypotheses: Wheeled field robots can distinct concrete from compacted sand and linoleum by using inertial measurements and applied motor current only:

H1: Variance of motor current differs for each underground class

H2: Variance of linear acceleration differs for each underground class

In the research at hand, we seek to validate whether the hypothesized assumptions are supported and sufficient to effectively distinguish the three underground types, which is the basis for appropriate control modes.

2.2 Experimental Setup

For elimination of surface influences, a horizontal terrain setup was used for all three underground classes. A wheeled field robot named TALOS was used, which was manufactured by the Institute of Agricultural Engineering at the University of Hohenheim, Germany (see **Fig. 1A**). The inertial coordinate system of the IMU is also depicted in **Fig. 1(A)**.

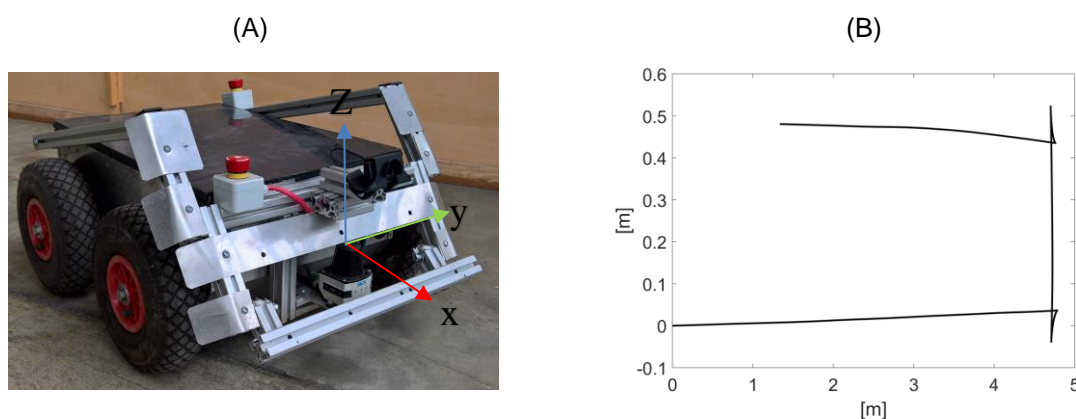


Figure 1: (A) The used wheeled field robot TALOS and (B) one of the paths followed by the robot

The size of the robot's platform is 400x500x600 mm. The robot is equipped with four separate driving motors with a total of 200 W and weights 25 kg. The inertial measurement unit used was a VN-100 (by VectorNav, Dallas, Texas, USA). The robot control software is programmed with ROS middleware (Robot Operating System) (QUIGLEY *et al.*, 2009). To test our model, we let the robot drive a straight line and then performed a rectangular turn: Turning 90° left on the spot, move forward for a few centimeters and turn again 90° left, followed by a straight movement. An exemplary path followed by the robot is shown in **Fig. 1B**. This path was recorded with the back wheel encoders of the robot. For following the predefined paths autonomously, a fixed voltage was applied to the motors to guarantee the same control command over the three different test classes. The used motor controllers were two dual-channel SDC2130 (Roboteq, Scottsdale, USA). The applied current to all 4 motors was tracked simultaneously with a frequency of 10 Hz. The values of the current were averaged and summed up for all four motors for each second, to estimate the applied current to the motors. In these test drives, we configured the motor controllers to apply the same voltage constantly to the wheel motors.



Figure 2: Three test areas: (A) linoleum, (B) compacted sand and (C) concrete.

Fig. 2 shows the three different test environments as seen by the robot camera. The surfaces just differed slightly in color and appearance. The synchronized ROS system allowed to compare the IMU acceleration data with the applied motor current.

3 Results and Discussion

The results of the three test runs showed high differences in the applied current to the motors and the resulting acceleration to the motor chassis measured by the IMU. The most differences could be detected while start time and while turning of the robot. The following **Fig. 3** summarizes the resulting currents applied to the motors. **Fig. 4** shows the corresponding linear accelerations of the robot. The applied currents to the motors showed always a peak when the robot system was turning, showing different peak heights dependent on the terrain. The highest peak with a maximum of 4.84A was applied to the motors at the concrete surface. The compacted sand resulted in a peak of 2.23A and the linoleum affected a peak of 1.95A. While driving straight, there was al-

most no difference visible in the motor current. When the robot was starting the movement, a small current peak could be assumed at all terrains.

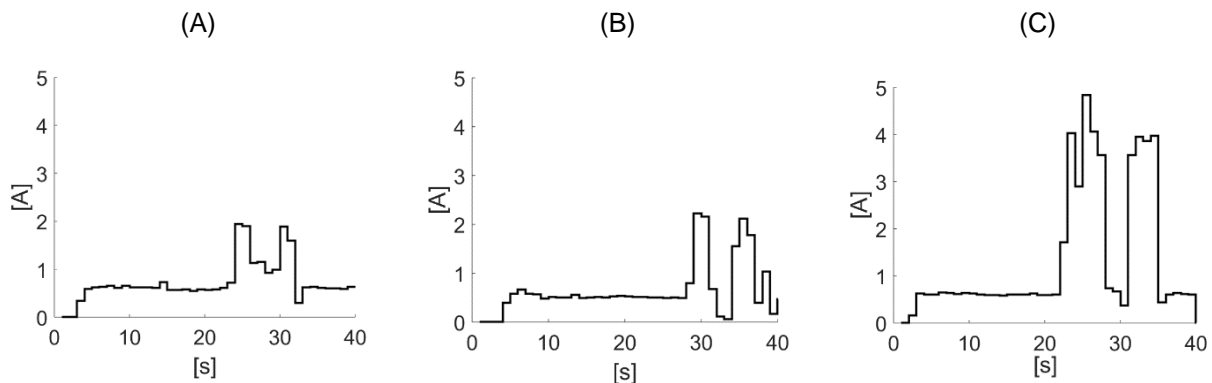


Figure 3: resulting currents at the motors (A) at linoleum (B) sand and (C) concrete

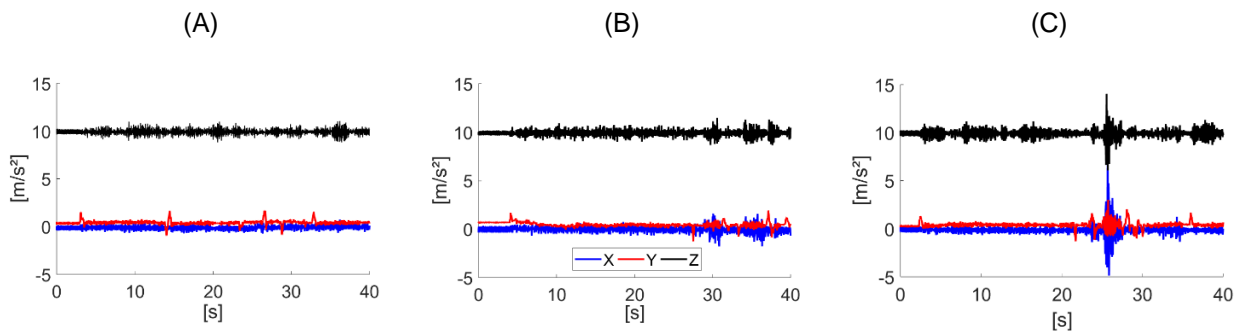


Figure 4: The resulting linear accelerations measured while driving (A) at linoleum (B) sand and (C) concrete. Linear acceleration X (blue), linear acceleration Y (red) and linear acceleration Z (black)

The driving direction was defined as the x-axis, the y-axis pointing to the left and the z-axis straight up of the robot (see **Fig. 1A**). The start of the driving is visible in all three linear acceleration axes depicted, independent on the surface. When the robot started moving after approximately 3 seconds, there is always a small peak at the y-axis. This results out of small differences of the motor friction, causing the motors not to start completely simultaneously. Interestingly the turning peaks of the x-axis and the z-Axis are almost not visible at the linoleum dataset of the accelerations. Just the y-axis shows small peaks when the direction changes happened. This is completely different when looking at the sand and the concrete dataset. Here are high peaks in the x and z acceleration visible. As more friction is applied to the wheels, the acceleration movement of the differential drive robot is not smooth, causing the wheels to slip irregular over the ground. This caused the peaks depicted here. The difference between the peaks is immense when we compare the different terrains.

When applying the data to hypothesis H1 it could be said that the currents at the motors differ highly dependent on the movement and the surface friction. Out of the datasets created, it is not possible to define, if the current applied to sand and linoleum always

differ and have to be proven in the future with more repetitions. However, there is the possibility to combine the information with the linear acceleration. Hypothesis H2 was proven for all three datasets. The highest impact of the surface roughness could be seen at the x-axis and the z-axis. Especially when the robot turns, there are high peaks at the x-axis and z-axis acceleration visible. As more friction at the surface as higher is the peak. Even more than 5m/s^2 for concrete.

These results indicate that it might be possible for wheeled field robots to distinct concrete from compacted sand and linoleum by using the change of linear accelerations in driving direction combined with the applied motor command by just using a decision tree structure. Although the directed H1 is not fully proven, the results indicate that systematic differences, depending on the underground classes, may also exist in the means of the linear x-axis accelerations. Our specific future research investigates how to implement appropriate control of the wheel motors. Therefore, control feedback from the model of the robot is required. A further question is, whether the acceleration data are more conclusive for higher velocities. Further research with respect to the implementation of an effective context-aware control pertains to the minimum duration of the evaluated time frames for reliable underground detection. The duration of the required time frames depends on the characteristics of the data. The aim is to keep the time frames as short as possible. Therefore, intelligent data preprocessing may be necessary.

4 Conclusion

The objective of this research was to improve accurate navigation of autonomous field robots. The fundamental idea is to incorporate models on causal dependencies where the internal sensors are used to correct the environmental model of the robot. For the case at hand, the causal dependencies are as follows: The robot applies electric energy to the wheel motor controllers. The wheel driving leads to a change in spatial position of the robot. The actual acceleration depends also on the grip of the underground. Model on the relationship between wheel driving and acceleration is represented in a static environmental model because it contains non-changing factors. The robot associates inertial measurements with this static environmental model. This enhances the self-control of the system, by retrieving environmental knowledge. The first hypothesis, the variance of motor current differs for each surface with different friction, is supported only under reserve. The second hypotheses that variance of linear acceleration varies for each surface with different friction was supported. Hence the deviation of the linear accelerations may be an indicator for the underground type. Future research is needed to further investigate the question how the magnitude of the linear accelerations relates to the underground type and motor torque.

References

- BECHAR A, VIGNEAULT C (2016):** Agricultural robots for field operations : Concepts and components. *Biosystems Engineering* 149: 94–111. doi:10.1016/j.biosystemseng.2016.06.014.
- BROOKS CA, IAGNEMMA K (2005):** Vibration-Based Terrain Classification for Planetary Exploration Rovers. *IEEE Transactions on Robotics* 21(6): 1185–1191.
- CASTELFRANCHI C, FALCONE R (2003):** From Automaticity to Autonomy : The Frontier of Artificial Agents. *Agent Autonomy*: 103–136.
- DUPONT EM, MOORE CA, COLLINS EG, COYLE JE (2008):** Frequency response method for terrain classification in autonomous ground vehicles. *Autonomous Robots* 24: 337–347. doi:10.1007/s10514-007-9077-0.
- DUPONT EM, ROBERTS RG, MOORE CA (2006):** Speed Independent Terrain Classification. Proceedings of the 38th Southeastern Symposium on System Theory: 240–244.
- GEORGE MP, INGRAND FF (1989):** Decision-Making in an Embedded Reasoning System. Proceedings - 11th International Joint Conference on AI: 972–978.
- JENNINGS NR, SYCARA K, WOOLDRIDGE M (1998):** A Roadmap of Agent Research and Development. *Autonomous Agents and Multi-Agent Systems* 1: 7–38.
- KHAN YN, KOMMA P (2011):** High Resolution Visual Terrain Classification for Outdoor Robots. IEEE International Conference on Computer Vision Workshops (ICCV Workshops).
- LEVESON NG (2011):** Engineering a Safer World. MIT Press.
- OJEDA L, CRUZ D, REINA G, BORENSTEIN J (2006):** Current-Based Slippage Detection and Odometry Correction for Mobile Robots and Planetary Rovers. *IEEE Transactions on Robotics* 22(2): 366–378.
- QUIGLEY M, GERKEY B, CONLEY K, FAUST J, FOOTE T, LEIBS J, BERGER E, WHEELER R, NG A (2009):** ROS: an open-source Robot Operating System. ICRA workshop on open source software 3: 5.
- RAO AS, GEORGEFF MP (1995):** BDI Agents : From Theory to Practice. Proceedings of the First International Conference on Multiagent Systems: 312–319.
- REINA G, MILELLA A, NIELSEN M, WORST R, BLAS MR (2015):** Ambient awareness for agricultural robotic vehicles. *Biosystems Engineering (Robotic Agriculture)*: 1–19. doi:10.1016/j.biosystemseng.2015.12.010.
- REISER D, PARAFOROS DS, KHAN MT, GRIEPENTROG HW, VÁZQUEZ-ARELLANO M (2017):** Autonomous field navigation, data acquisition and node location in wireless sensor networks. *Precision Agriculture* 18(3): 279–292. doi:10.1007/s11119-016-9477-2.
- VÁZQUEZ-ARELLANO M, GRIEPENTROG HW, REISER D, PARAFOROS DS (2016):** 3-D Imaging Systems for Agricultural Applications - A Review. *Sensors* 16(618): 24. doi:10.3390/s16050618.
- WEISS C, FRÖHLICH H, ZELL A (2006):** Vibration-based Terrain Classification Using Support Vector Machines. Proceedings of the 2006 IEEE/RSJ International Conference on Intelligent Robots and Systems: 4429–4434.
- ZENKER S, AKSOY EE, GOLDSCHMIDT D, WÖRGÖTTER F, MANOONPONG P (2013):** Visual Terrain Classification for Selecting Energy Efficient Gaits of a Hexapod Robot. IEEE/ASME International Conference on Advanced Intelligent Mechatronics (AIM).
- ZOU Y, CHEN W, XIE L, WU X (2014):** Comparison of different approaches to visual terrain classification for outdoor mobile robots. *Pattern Recognition Letters* 38: 54–62. doi:10.1016/j.patrec.2013.11.004.

Concept and first results of a field-robot-based on-the-go assessment of soil nutrients with ion-sensitive field effect transistors

Vadim Tsukor¹, Stefan Hinck¹, Walter Nietfeld², Frank Lorenz³, Elena Najdenko³, Andreas Möller⁴, Daniel Mentrup⁵, Tino Mosler⁶, Arno Ruckelshausen¹

¹University of Applied Sciences Osnabrueck, Postfach 1940, 49009 Osnabrueck, Germany;

²Bodenprobetechnik Nietfeld GmbH, Robert-Bosch-Str. 15, 49610 Quakenbrueck, Germany

³LUFA Nord-West, Jaegerstr. 23-27, 26121 Oldenburg, Germany

⁴ANEDO Ltd., Huelsemeyerstr. 35, 49406 Eydelstedt, Germany

⁵iotec GmbH, Albert-Einstein-Str. 1, 49076 Osnabrueck, Germany

⁶MMM Tech Support GmbH & Co. KG, Weigandufer 18, 12059 Berlin, Germany

E-mail: v.tsukor@hs-osnabrueck.de; Tel.: +49 (0)541 969 31 64

Abstract: In the research project "soil2data", a mobile field laboratory will be developed. While driving/moving over a field, it collects representative mixed soil samples, conducts a soil nutrient analysis and leaves the excavated soil on the field after measurement. The results with the corresponding GPS-position are stored or sent to a data platform. Innovative ion-sensitive field-effect transistors (ISFETs) are the key component of the mobile field laboratory. A custom-specific ISFET multi-sensor module – a "lab on chip" – was specified und produced to measure the nutrients (N, P, K), pH and electrical conductivity of the soil extraction solution.

The mobile field laboratory can be used with various vehicles. Mounted on a carrier and coupled on a tractor but also on an autonomous field-robot platform. The combination of the on-the-go soil nutrient analysis method with an autonomous field robot offers considerable advantages with respect to economic and environmental requirements. The soil nutrient analysis is done fully automated directly on the field, the result is promptly available real-time and can be considered for other ongoing or shortly following processes (e.g. planned fertilization measures).

Key words: field robot, ion-sensitive field effect transistors (ISFET), mobile field lab, soil nutrient analysis, soil test

1 Introduction

Knowledge of the spatial distribution of soil nutrient status is important information for a sustainable fertilization in crop production. Up to now the process of soil sampling and analysis is time consuming and cost-intensive. The current practice of soil nutrient analysis comprises the following steps: a) creation of a sampling plan, b) soil sampling in the field, c) transportation of the soil samples to a laboratory, d) physical and chemical preparing of the soil samples, e) analysis of the sample f) creation of a documentation and sending the analysis result to the farmer as well as g) disposing soil material from the laboratory. The entire process, from soil sampling until the farmer receives the analysis results takes in general several a long time (up to 8 weeks). This means that the analy-

sis results cannot be integrated into current fertilizing processes in a timely manner, which is very critical, especially in the spring.

The development of an on-the-go soil nutrient analysis method – a mobile field laboratory – that delivers soil parameters immediately will open up new options. The analysis results are available in a very short time. It will take only a short moment after finishing soil sampling and analysis at the field.

By combining a mobile field-laboratory (field-lab) with an autonomous carrier platform (e.g. field robotic “BoniRob”) will provide new opportunities in soil sampling and mapping. An on-the-go verification of the actual measurement results on the field with a database is one of the options. The dynamic adaptation of the sampling line during the soil sampling will be another innovative option. If the currently processed series of measurements on a sampling line or within a sub field show a high fluctuation in the measurements, it will be possible to subdivide this sampling line (HINCK *et al.*, 2018).

Transportation of soil probe material from field to laboratory is not necessary. Furthermore, it will greatly enhance infield variability characterization by dividing the field in smaller sub fields than it would be possible with traditional soil sampling and mapping. With this new technique, the knowledge of the spatial distribution of soil nutrients status will be improved. Also, the repetition of the measurement, e.g. annually, weekly or even daily (at a sub field or for specific area within a field) would be possible. Also, the availability of the analysis result will be improved and the real-time linking between the actual result and an existing database will be possible.

This new approach will contribute to a sustainable and demand-driven fertilization for crop production at small-scale field level.

2 Materials and methods

Several researchers have been working on the implementation of an on-the-go nutrient analysis for field application. A soil preparation method for mobile field laboratories for analyzing NO_3^- , K^+ and P was developed by KIM *et al.* (2007). Mobile field laboratories for on-the-go measurement have been designed for analyzing NO_3^- in the topsoil (SIBLEY *et al.*, 2010, SIBLEY, 2008), for pH (VISCARRA ROSSEL *et al.*, 2004) and for multiple parameters including NO_3^- , K and pH (SETHURAMASAMYRAJA *et al.*, 2008).

The interdisciplinary research project “soil2data” is about to develop a mobile field laboratory to measure the nutrients (N, P, K), pH and electrical conductivity of the soil extraction solution in on-the-go mode. Three carrier platforms are planned in the project for the use of the mobile field lab. The lab is equipped with additional systems for an automatic generation of a soil sampling plan, components for chemical and physical soil preparation, sensors for soil analysis and systems for storing the analysis results.

One of these carrier platforms is the autonomous field-robot BoniRob (RUCKELSHAUSEN *et al.*, 2009). It includes sensor systems for autonomously navigating autonomously along the crop rows or by using GPS coordinates. The robot has an empty cavity within

the body, which serves as carrier, electricity supplier for multiple application modules – App's (SCHOLZ *et al.*, 2014). The standardized field robot interfaces (hardware/software) and modular construction of the App's enable a flexible integration of these application modules also in other carrier platforms (e.g. a tractor) or other field-robots.



Figure 1: Autonomous field-robot BoniRob with "soil2data" application module

The application module for soil nutrient analysis – “soil2data” mobile field lab – contains the following components:

- A soil sampler to collect the soil samples
- A collection container to create a mixed soil sample (15-20 core samples, 250-300 g soil material)
- The measuring systems to determine the amount of collected soil material
- A transport system (chain elevator) for transporting the soil material
- A linear actuator and a mixer for homogenization / physical preparation of a mixed soil sample
- Various pumps / valves to supply the extraction agents for the chemical preparation of the soil material
- A filter station to filter the measurement solution extracted from the soil material
- An ISFET multi-sensor module including readout circuit for measuring the concentration of the nutrients (N, P, K), pH and electrical conductivity of the extracted solution.
- Transport system for the removal of extracted soil material
- Systems for cleaning of all components for preparing subsequent measurements
- An industry PC-system with real time Ethernet bus to control the components of the field lab, to communicate with readout circuit of the ISFET multi-sensor module and the carrier platform.

As soil sampler, a commercial product from the company Bodenprobetechnik Nietfeld GmbH (Germany) is used. This soil sampler (boring-type, soil auger Ø 16 mm) allows sampling at a depth of 30 cm and has been equipped with additional components for the automation of the overall soil nutrient analysis process.

After soil sampling and complete of a representative soil mix sample, the soil sample processing takes place. It should be noted, however, that the quality of soil sample processing in this on-the-go soil nutrient analysis process is fundamental and crucial for an autonomous, fully automated soil nutrient study. The flawed execution of the soil sampling process can lead to erroneous assessment of the measurement. Therefore, the results of future field trials measurements within the project will be qualitatively compared with the results of the state of the art laboratory analysis. In the context of the research project "soil2data", the project partner LUFA Nord-West – an accredited service laboratory affiliated with the Chamber of Agriculture in Lower Saxony / Germany – developed a new soil processing method for the on-the-go soil nutrient analysis on the field (NAJDENKO *et al.*, 2018).

The new soil sample processing method - referred to as the "soil2data LUFA method" - is based on the standard soil sample processing method for nutrient analysis in laboratory and includes the following steps: homogenization of a mixed soil sample, supply of the extraction agent to dissolve the nutrients from the soil, filtration of the soil sample extract. In order to reduce the soil sample processing time, a chemical and mechanical method for homogenizing the soil material in the pre-wet state with a mixer and simultaneous feed of the extraction solution is developed and tested. This method produced comparable results under labor conditions and will now be tested/used the "soil2data" mobile field lab for on-the-go soil sample preparation.

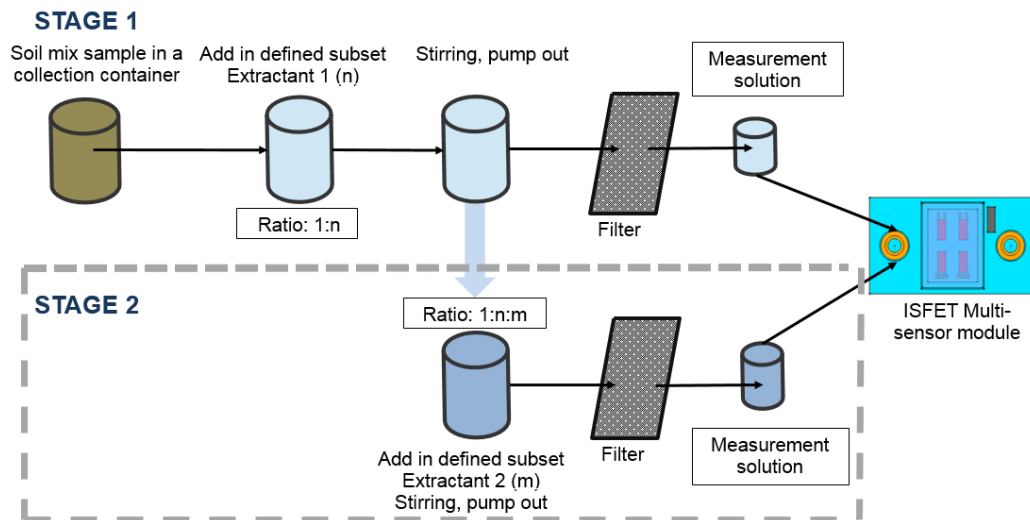


Figure 2: "soil2data" nutrient extraction procedure

In order to allow a flexibility during the testing of different extraction liquids and to cover the diversity of the extraction methods, a proposed soil sample processing method was extended. For a case, that only one extraction agent for a soil sample processing will be used, was a Stage 1 designed with the standard steps like laboratory soil sample processing procedure: homogenization of a mixed soil sample, supply of the extraction agent to dissolve the nutrients from the soil, filtration of the soil sample extract. In case,

that more than one extraction agent or a mix of several extraction agents will be used, is a soil sample processing method with a Stage 2 extended.

The description of the "soil2data" nutrient extraction procedure is as follows (**Fig. 2**):

- Stage 1 – after determining the amount of soil material in a collection container, an extraction fluid (Extractant 1) is added and stirred vigorously with a mixer for a fixed time. Afterwards, a defined quantity of the measurement solution is pumped out and passed to a filter station.
- Stage 2 – a various extraction fluid (Extractant 2) is added to the residual amount of soil material in the collection container is stirred again with a mixer. There after the measurement solution is pumped off and passed to same filter station.

These two stages were realized in the hardware of the "soil2data" mobile field lab with a chain elevator with a hydraulic drive. It contains the storage containers for mixed soil sample and has fixed reference points during operation – the so-called workstations (WS):

- Workstation 1 – transfer soil samples from soil sampler, collecting the mixed soil sample, pre-wetting with Extractant 1, determination of the quantity of the mixed soil sample
- Workstation 2 – "soil2data" soil nutrient extraction procedure (Stage 1 / Stage 2)
- Workstation 3 – removal of measured soil material from a collection container
- Workstation 4 – cleaning of collection container

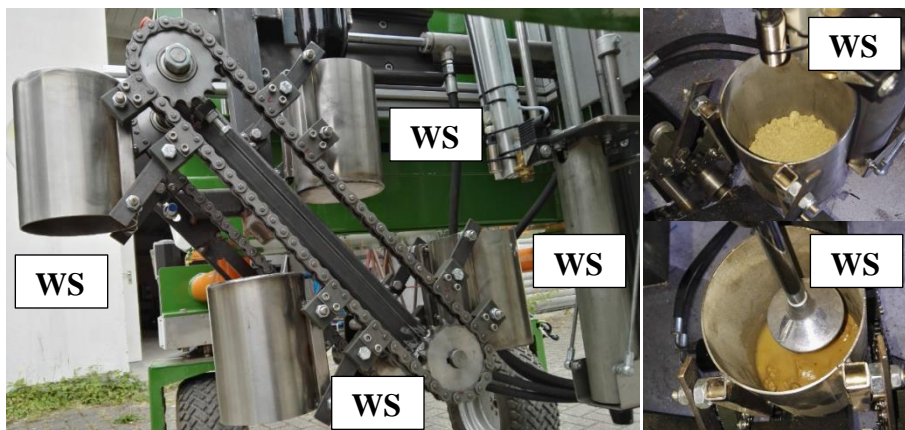


Figure 3: "soil2data" soil nutrient extraction procedure – hardware

The four workstations allow to perform the whole soil nutrient analysis process continuously without stopping – because work steps can be carried out simultaneously.

To enable the on-the-go soil nutrient analysis process directly on the field, a customer specific multi-sensor module for research project "soil2data" was produced by the company MICROSENS SA (Switzerland). This module is a key component of the mobile field laboratory. It consists of a closed LTCC (Low Temperature Cofired Ceramics) housing with an inlet / outlet tube for the influx / efflux of the prepared soil samples in liquid state (measurement solution) and contains four single ion-sensitive field-effect

transistors (ISFET) to measure the nutrients (N, P, K), pH and electrical conductivity of the soil (**Fig. 4**).

The conventional ISFET readout circuits cannot be used to read out the electrical output signals from all four ISFET chips build into a multi-sensor module simultaneously. Such readout circuits do not provide amplification to the electrical output, and simultaneous interrogation of multiple ISFET's provides an unstable, oscillating output signal. Therefore, a new readout circuit for the ISFET multi-sensor module has been developed by the University of Applied Sciences Osnabrück and ANEDO Ltd. It eliminates the above described problem and generates a stable output signal for the multi-sensor ISFET module.



Figure 4: Multi-sensor module with four ISFET chips

3 Results

The multi-sensor ISFET module with the newly developed readout circuit was tested under laboratory conditions to check the stability of the readout circuit output signal and the reproducibility and quality of the measurement data output from each individual ISFET chip (**Fig. 5**).

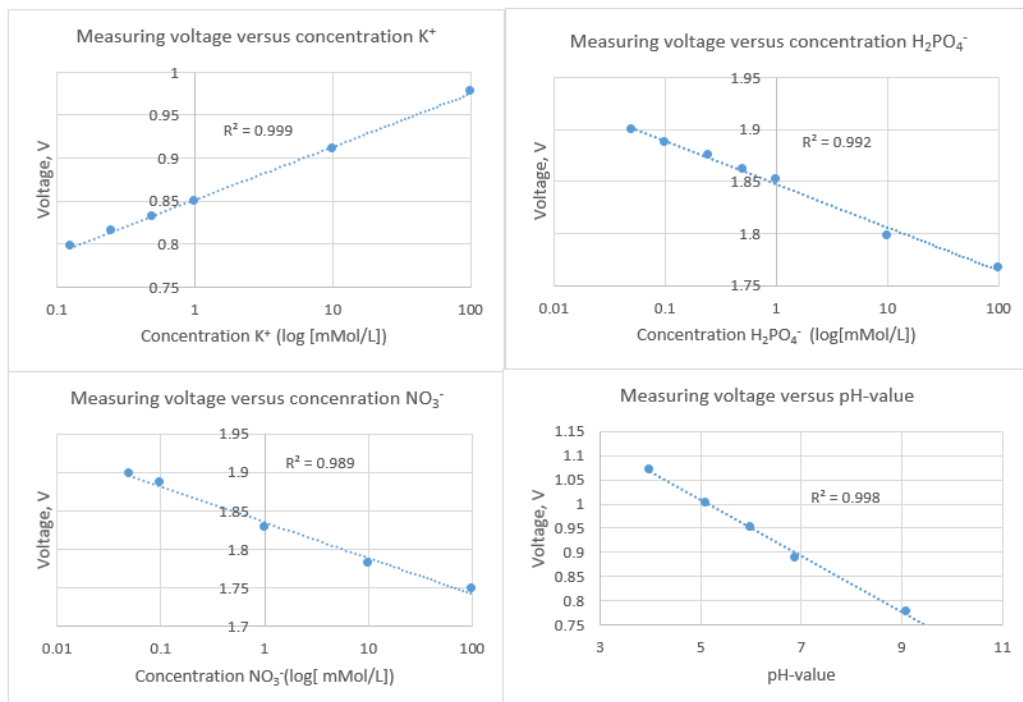


Figure 5: Results from multi-sensor ISFET measurements results of calibration solutions with different concentrations

The time required to stabilize the measurement signal was experimentally determined to 200 seconds.

The “soil2data” soil nutrient extraction procedure was tested in single steps with the use of different extraction agents. The optimum time required for liquidate/getting the nutrient extraction from a soil sample was also experimentally determined. It takes approximately 15 minutes when using a two-stage soil sample preparation procedure.

4 Conclusion

The first functional measurements with the newly developed readout circuit were carried out with the aid of calibration solutions and showed good results. The newly developed two-stage soil sample preparation method allows simultaneous parallel execution of the necessary work steps so that the entire process sequence can be realized in non-stop mode.

The individual work steps for soil sample preparation (such as handover of a soil mix sample for preparation, extraction of the nutrients with different extraction agents, filtering procedure, etc.) were created and tested in individual work steps. The times required for the preparation processes have been determined.

Transfer, adaption and optimization of the laboratory soil sample preparation method for field conditions and also first experiment results show that the determination of the nutrient content of soil is possible by using ISFET sensors.

The next step will be integrating all required components for on-the-go nutrient analysis into a functional application module (App). Subsequently numerous field trials will be made in order to validate the entire mobile field laboratory system and compare nutrient analysis results from mobile soil laboratory to traditional laboratory results.

Acknowledgement

The project is supported by funds of the Federal Ministry of Food and Agriculture (BMEL) based on a decision of the Parliament of the Federal Republic of Germany via the Federal Office for Agriculture and Food (BLE) under the innovation support program.

References

- ADAMCHUK VI, LUND ED, SETHURAMASAMYRAJA B, MORGAN MT, DOBERMANN A, MARX DB (2005):** Direct measurement of soil chemical properties on-the-go using ion-selective electrodes. *Computers and Electronics in Agriculture* 48(3): 272-294.
- HINCK S, MÖLLER A, MENTRUP D, NAJDENKO E, LORENZ F, MOSLER T, TESCH H, NIETFELD W, SCHOLZ C, TSUKOR V, RUCKELSHAUSEN A (2018):** soil2data: Concept for a mobile field laboratory for nutrient analysis. Proceedings of the 14th ICPA, Montreal, Canada.

- KIM HJ, HUMMEL JW, SUDDUTH KA, MOTAVALLI PP (2007):** Simultaneous analysis of soil macronutrients using ion-selective electrodes. *Soil Science Society of America Journal* 71(6): 1867-1877.
- NAJDENKO E, NEUHAUS C, LORENZ F (2018):** Anpassung von Labormethoden für die Online-Bodenuntersuchung im Feld. Paper submitted to VD-LUFA Congress 2018, Muenster, Germany.
- RUCKELSHAUSEN A, BIBER P, DORNA M, GREMMES H, KLOSE R, LINZ A, RAHE R, RESCH R, THIEL M, TRAUTZ D, WEISS U (2009):** BoniRob – an autonomous field robot platform for individual plant phenotyping. Proceedings of JIAC 2009, Wageningen: 841-847.
- SCHOLZ C, GOETTINGER M, HINCK S, MOELLER K, RUCKELSHAUSEN A (2014):** Automatic soil penetrometer measurements and GIS-based documentation with the autonomous field robot platform BoniRob. 12th International Conference on Precision Agriculture, ISPA International Society of Precision Agriculture, Ed., Sacramento, CA, USA.
- SETHURAMASAMYRAJA B, ADAMCHUK VI, DOBERMANN A, MARX DB, JONES DD, MEYER GE (2008):** Agitated soil measurement method for integrated on-the-go mapping of soil pH, potassium and nitrate contents. *Computers and electronics in agriculture* 60(2): 212-225.
- SIBLEY KJ (2008):** Development and use of an automated on-the-go soil nitrate mapping system. PhD thesis, Wageningen University, Wageningen.
- SIBLEY KJ, BREWSTER GR, ADSETT JF, STRUIK PC, ASTATKIE T (2010):** In-field measurement of soil nitrate using an ion-selective electrode. INTECH Open Access Publisher.
- VISCARRA ROSSEL RA, THYLÉN L, MCBRATNEY AB, GILBERTSSON M (2004):** Development of an on-the-go soil sensing system for determinations of soil pH and lime requirement. Proceedings of the 7th International Conference on Precision Agriculture and Other Precision Resources Management, Hyatt Regency, Minneapolis, MN, USA: 25-28.

Leaf area estimation of reconstructed maize plants using a time-of-flight camera

Manuel Vázquez-Arellano¹, David Reiser¹, Dimitris S. Paraforos¹, Miguel Garrido-Izard², Hans W. Griepentrog¹

¹University of Hohenheim, Institute of Agricultural Engineering, Garbenstr. 9, D-70599 Stuttgart, Germany

²Laboratorio de Propiedades Físicas (LPF)-TAGALIA, Technical University of Madrid, Madrid 28040, Spain

E-mail: mvazquez@uni-hohenheim.de

Abstract: The leaf area is an important plant parameter for plant status and crop yield. In this experiment, a low-cost time-of-flight camera, the Kinect v2, was mounted on a robotic platform to acquire 3-D data of maize plants in a greenhouse. The robotic platform drove through the maize rows and acquired 3-D images that were later registered and stitched. Three different maize row reconstruction approaches were compared: reconstruct a crop row by merging point clouds generated from both sides of the row in both directions, merging point clouds scanned just from one side and merging point clouds scanned from opposite directions of the row. The resulted point cloud was subsampled and rasterized, the normals were computed and re-oriented with a Fast Marching algorithm. The Poisson surface reconstruction was applied to the point cloud and new vertices and faces generated by the algorithm were removed. The results showed that the approach of aligning and merging four point clouds per row and two point clouds scanned from the same side generated very similar average mean absolute percentage error of 8.8% and 7.8%, respectively. The worst error resulted from the two point clouds scanned from both sides in opposite direction with 32.3%.

Key words: 3-D sensors; crop characterization; agricultural robotics; precision farming; plant phenotyping

1 Introduction

Information such as stem diameter, plant height, leaf angle, leaf area (LA), number of leaves and biomass are of particular interest for high-end agricultural applications such as precision farming, agricultural robotics and automatic phenotyping for plant breeding purposes. A very important plant parameter is the LA, because it provides important information about the plant status and is closely related with the crop yield. However, LA is one of the most difficult parameters to measure (HOSOI *et al.*, 2011) since manual methods are time consuming and the 2-D image-based ones are not very accurate due to leaf occlusion. A commonly used index describing the LA is the leaf area index (LAI), which is the total one-sided area of leaf tissue per unit ground surface area (BRÉDA, 2003).

3-D imaging could be a good method for a fast and more accurate LA measurement, compared to the 2-D approach, since it does not depend on the position of the leaves (of the plant) in space relative to the image acquisition system. However, 3-D scanning systems are normally very expensive for sensing or monitoring applications. Therefore, economically affordable 3-D sensors are a key factor for the successful implementation of 3-D imaging systems in agriculture. A low-cost time-of-flight (TOF) camera, like the Kinect v2 (Microsoft, Redmond, WA, USA), has proven to have enough technical capabilities for 3-D plant reconstruction (VÁZQUEZ-ARELLANO *et al.*, 2018).

Research has been done using the Kinect v2 for weed volume estimation (ANDÚJAR *et al.*, 2016) as well as high throughput phenotyping of cotton in open field; the former did not rely on a shadowing device while the latter did. HÄMMERLE & HÖFLE (2017) measured the maize crop height in open field under real conditions including wind and sunlight, the measurements were slightly below the results presented in other studies due to the challenging field conditions and the complex architecture of the maize plant at late stage. HU *et al.* (2018) measured the LA and the projected LA, among other parameters, of 63 pots of lettuce by subsampling the generated point cloud and using a triangular mesh to reconstruct the surface. The LA measurement was calculated by adding the area of all triangles in the mesh, and the projected LA was the area projected onto the x-y plane along the z axis. The total LA measurement had a R^2 determination coefficient of 0.94 and the projected LA 0.94. However, while the projected LA followed a linear distribution, the total LA measurements followed a power law distribution due to occlusion when the plant had more leaves. PAULUS *et al.* (2014) measured the LA of sugar beet leaves, relying on the structured light based Kinect v1. They mentioned the importance of acquiring 3-D data of above ground plant organs, such as plant leaves and stems, in order to extract 3-D plant parameters. The R^2 determination coefficient were 0.43 and 0.93 for LA and projected LA measurement, respectively. They mentioned that the high error in the LA estimation was due to strong smoothing effects that produced overestimated measurements. However, the projected LA measurements, defined as ground cover, reduced those effects. They stated that the projected LA can be used as a proxy for agricultural productivity since the photosynthetic activity is linked to the LA directed to sunlight. NAKARMI & TANG (2012) developed an automatic inter-plant spacing sensing system for early stage maize plants. They placed the TOF camera in a side-view position, since the purpose was to measure the distance between maize stems, that camera position was the optimal.

The aim of this research was to estimate the LA of maize plants by merging point clouds obtained from different 3-D perspective views. Three approaches were evaluated: aligning and merging point clouds from two paths and two directions, aligning point clouds scanned from the same side of the crop row and aligning point clouds scanned from opposite directions and different paths. In order to estimate the LA, a methodology was proposed for reconstructing the surface of a rasterized point cloud after the alignment and merge. The main contribution of this research was to reconstruct the surface and the estimate of the LA of entire maize crop rows. Previous researches focused only on

reconstructing single plants. Therefore, this research sets a new milestone for high throughput plant reconstruction.

2 Material and methods

2.1 Experiment setup

The 3-D data acquisition was done in a greenhouse from the University of Hohenheim (see **Fig. 1a**). The seeding was performed in 5 rows with different standard deviations in order to emulate different realistic performances of agricultural seeding implements (see Figure 1b). The row spacing (inter-row) was 0.75 m and the plant spacing (intra-row) was 0.13 m. Every row had 41 plants in a length of 5.2 m, and the plant growth stage was between V1 and V4. The LA was measured by hand using measurement tape. The robotic platform was driven, using a joystick, at a maximum driving speed of $0.8 \text{ m}\cdot\text{s}^{-1}$ through every path in the go and return direction to obtain 2.5-D images that were later transformed to 3-D images. At every headland, the robot was turning 180 degrees, therefore, the 3-D perspective view was different in the go and return directions of every path. A viewpoint was established (camera plot in **Fig. 1b**), to avoid confusion between the left and right side of the crop row. Every single plant was manually measured and parameters such as plant height, number of leaves, stem diameter and LA were registered. The hardware and sensors used during the experiment are explained in detail by VÁZQUEZ-ARELLANO *et al.* (2018).

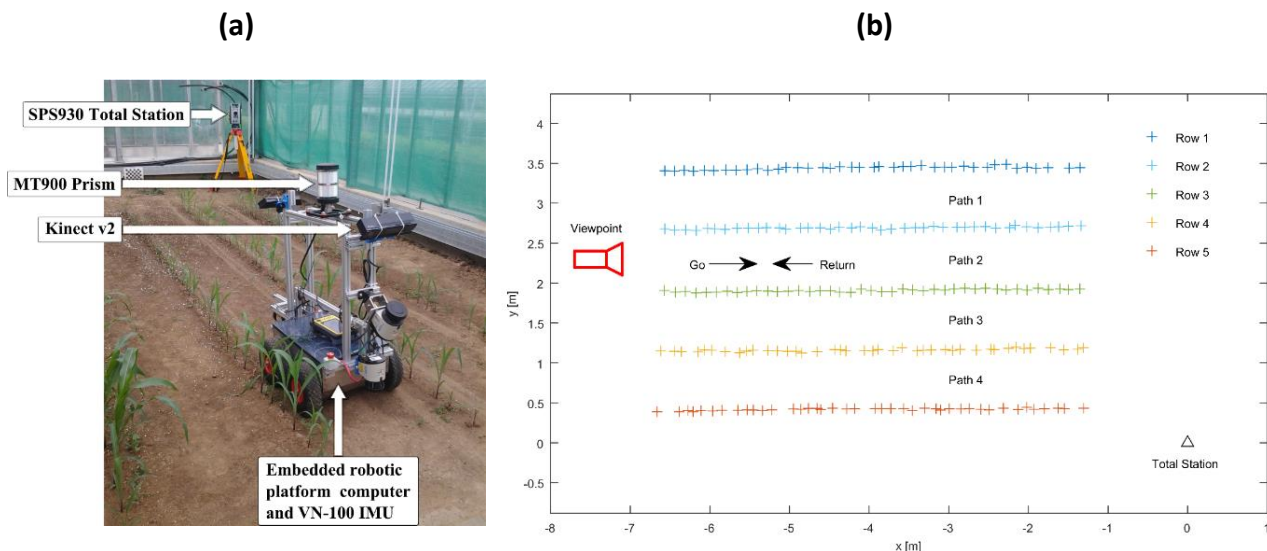


Figure 1: Robotic platform used for 3-D data acquisition (a) and maize seeding positions (+) and viewpoint represented by the camera plot. The left and right side of the crop row, as well as the go and return drive were set up relative to the viewpoint of the camera plot (b).

2.2 Data processing

The point clouds were processed using the Computer Vision System Toolbox™ of MATLAB R2016b (MathWorks, Natick, MA, USA). Additionally, CloudCompare (EDF R&D, 2011) was used for point cloud rasterization and surface reconstruction. In this research three different maize row point clouds alignments were done to investigate the

trade-off of merging all four point clouds (Path 1 go, Path 1 return, Path 2 go and Path 2 return), two point clouds from the same side of the crop row, such as Row 2 from the left side (i.e. Path 1 go and Path 1 return) and from both sides scanned from opposite directions (i.e. Path 1 go and Path 2 return).

2.3 Leaf area estimation

The methodology for LA estimation in this investigation (depicted in **Fig. 2**) was based on the generated maize row point clouds generated in a previous research by VÁZQUEZ-ARELLANO *et al.* (2018). These point clouds were initially imported pairwise, each of the point clouds were filtered using a radius outlier removal (ROR) and statistical outlier (SOR) filter. The ROR filter was set to a radius of 5 cm with a minimum required neighbours of 800. The SOR filter was set to 20 points for the mean distance estimation with a standard deviation multiplier threshold $nSigma$ equal 1. Then, the Random Sample Consensus (RANSAC) algorithm was applied for each point cloud pair in order to segment the plant points from the soil points. The maximum distance from an inlier to the RANSAC based plane fitting was set to half the theoretical intra-row distance between plants of 17 cm, resulting 6.5 cm.

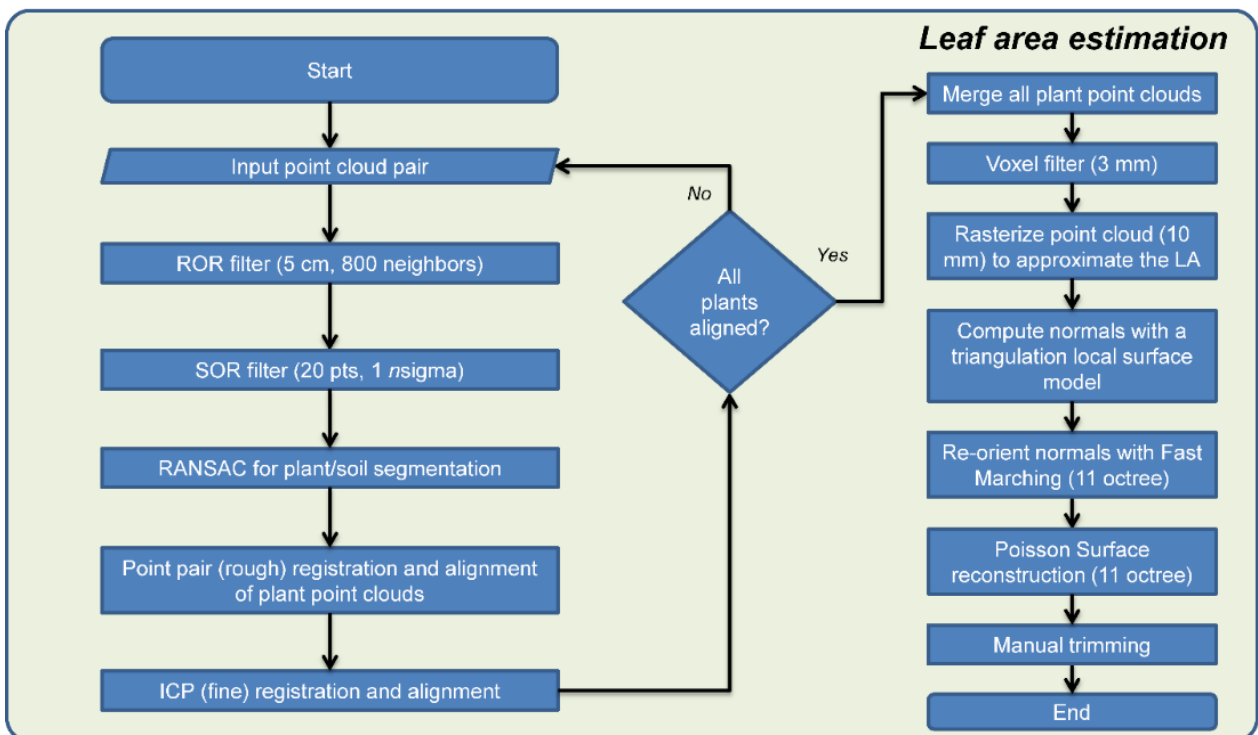


Figure 2: Methodology for plan point cloud alignment and merge for LA estimation.

The point cloud pair was aligned with a manual rough registration process by picking at least three equivalent point pairs in both point clouds. After that, the Iterative Closest Point (ICP) was used for fine registration and alignment. This process was performed one time for two point cloud alignments and three times for four point cloud alignments.

After all the point clouds of every dataset were aligned, the next step was to merge them together. The merging process could produce duplicate points, therefore, a sub-sampling was applied using a voxel grid (3 mm × 3 mm × 3mm) filter. The next step was to rasterize the point cloud in order to obtain a point cloud generated with a projection in the z axis with a grid step (cell) of 1 cm. Every point inside the rasterized point cloud was the one with the maximum height; in the case that more than one point was falling in each cell.

After the rasterized point cloud was generated, the next step was to compute the normals, this computations were done by using a triangulation local surface model for surface approximation with a preferred orientation in the z axis. Then, the normals were re-oriented in a fast and consistent way by using the Fast Marching algorithm (DEWEZ *et al.*, 2016) with 11 octrees. Finally, in order to estimate the LA a mesh was generated by using the Poisson reconstruction method (KAZHDAN *et al.*, 2006).

For the Poisson reconstruction the main input parameter was the octree depth, where the deeper the value the finer the result. In this research, the octree depth value was set to 11. A characteristic of the Poisson reconstruction is that it produces a watertight surface, which is not suitable for our dataset where leaves are separated (LI *et al.*, 2015). In order to trim the reconstructed surface to fit the point cloud, a surface trimming algorithm was applied (KAZHDAN & HOPPE, 2013). The disadvantage of this algorithm is that, for non-watertight surfaces such as the leaves in this dataset, it is difficult to find the right parameters to trim the mesh. This problem was approached by identifying the biggest leaves in this point cloud and manually trimming them until the reconstructed surface fits the silhouette of the biggest leaves of the row point cloud, this parameter value was interactively found by removing the triangles with vertices having the lowest density values, and they corresponded to the triangles that were the farthest from the input point cloud. If the trimming was done beyond the point cloud limits, the reconstructed surface started to shift the leaf border beyond the real one, thus producing overestimated values as reported by PAULUS *et al.* (2014). Also, the density value was reduced if a mesh membrane was generated between close leaves, because this effect would generate an overestimated LA value. The LA reference measurements were obtained by measuring the length and the width of every leaf in the plants, if the leaf was touching the ground it was not considered. In order to correct the LA measurements a factor was used as in MONTGOMERY (1911)

$$LA = 0.75 * L * W \quad (1)$$

Where L and W are the length and width of the maize leaf, respectively. In order to evaluate the error in the estimated measurements, the root mean square error (RMSE) was calculated with the following formula:

$$RMSE = \sqrt{\text{mean}(t - a)^2} \quad (2)$$

Where t represents the target measurement and a the actual measurement. Additionally, the mean absolute percentage error (MAPE) was also considered. The MAPE was calculated using the following formula:

$$MAPE = \text{mean}\left(\left|\frac{t - a}{t} \times 100\right|\right) \quad (3)$$

3 Results and discussion

In **Fig. 3a** it is depicted the result of the Poisson surface reconstruction generated from the rasterized point cloud projected on the z direction. Since the Poisson algorithm generated new meshes, it was required to trim them by adjusting the density value, which removed low-density meshes until they fit inside the boundaries of the point cloud that generated it (see **Fig. 3b**).

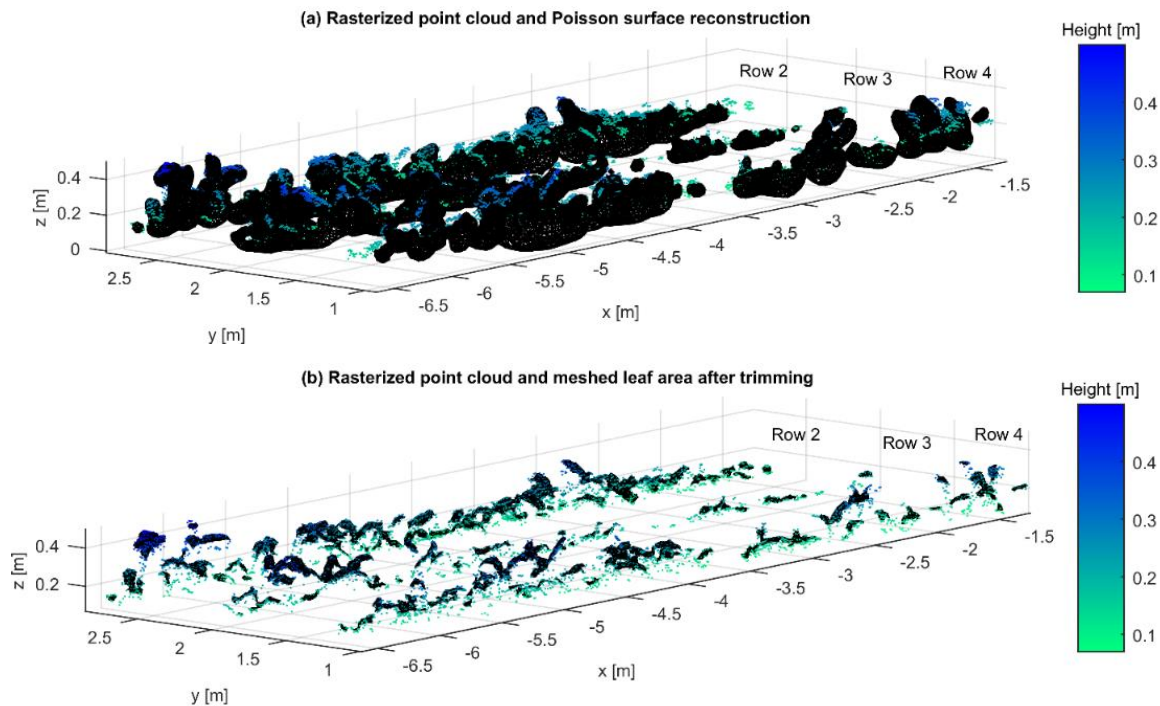
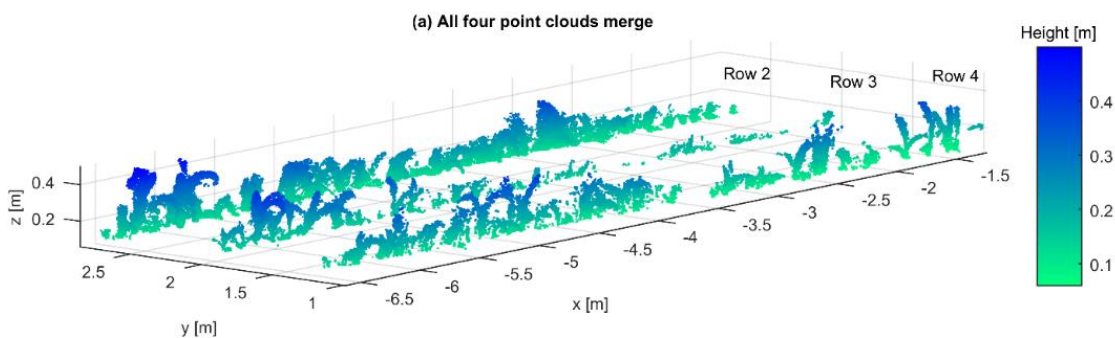


Figure 3: (a) Rasterized point cloud used to generate the Poisson surface reconstruction (black mesh), and (b) the same point cloud with the manually trimmed surface (black mesh).

Table 1 shows that the RMSE and MAPE were 231 cm^2 and 8.8%, respectively for the four point cloud merge approach. This error was relatively small since the rasterized point clouds were well defined and they also had a relative continuity without duplicate points in the z axis. In **Fig. 4** it can be seen that the plants are thicker than they are in reality due to the error accumulated during the reconstruction of the maize row and the alignment and merging of the four point clouds.

Table 1: Align and merge four point clouds scanned from both sides and directions

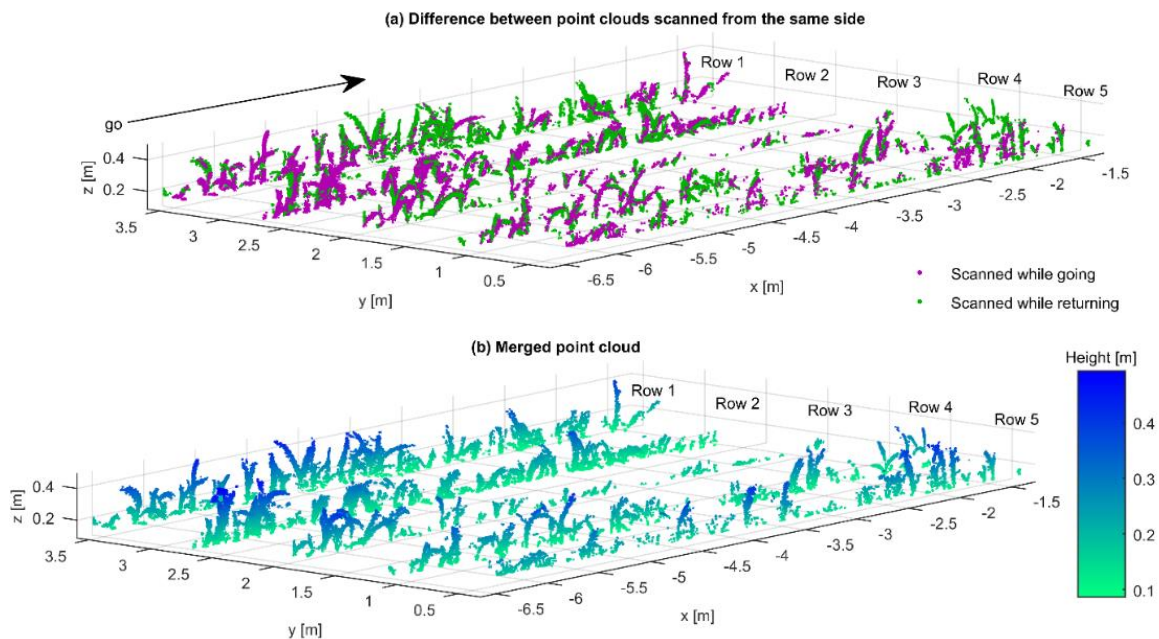
Direction	Crop row	Rasterized crop height (10 mm) [cm ²]	Poisson surface reconstruction [cm ²]	Ground truth LA [cm ²]	RMSE [cm ²]	MAPE
Go left side, return left side, go right side and return right side	2	4,713	4,580	4,191	389	9.2%
Go left side, return left side, go right side and return right side	3	1,781	1,895	1,634	263	16%
Go left side, return left side, go right side and return right side	4	2,179	2,777	2,819	42	1,4%
Average		2,891	3,084	2,881	231	8.8%

**Figure 4:** All four point clouds merge per maize row.

By merging two point clouds reconstructed from scans taken from the same side (see **Fig. 5a**), meaning that the robotic platform drove in the same path going and then returning, the advantage was that the maize plants were well defined in their 3-D morphology, as seen in **Fig. 5b**, but leaves from the other side were theoretically incomplete. However, the results of **Table 2** showed that the RMSE and MAPE were 203 and 7.8%, respectively. These errors in the estimation of the LA were not very different from the ones obtained by merging four point clouds. One explanation could be related with the optimal position of the TOF camera and its inherent light volume technique that acquires dense information in a single shot.

Table 2: Align and merge two point clouds scanned from the same side of the crop row

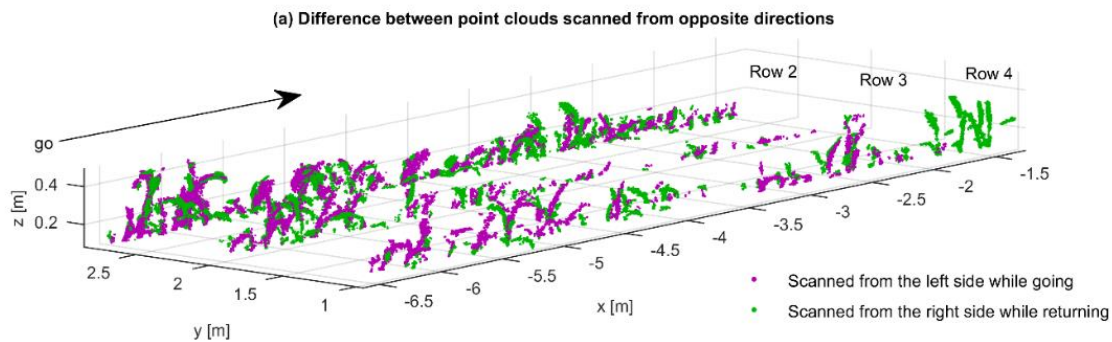
Direction	Crop row	Rasterized crop height (10 mm) [cm ²]	Poisson surface reconstruction [cm ²]	Ground truth LA [cm ²]	RMSE [cm ²]	MAPE
Go right side and return right side	1	2,685	2,611	2,824	213	7.5%
Go left side and return left side	2	2,680	4,091	4,191	100	2.3%
Go left side and return left side	3	1,077	1,733	1,634	99	6%
Go left side and return left side	4	1,611	2,332	2,819	487	17.2%
Go left side and return left side	5	1,433	1,762	1,879	117	6.2%
Average		1,897	2,505	2,669	203	7.8%

**Figure 5:** Same side scanned point cloud (a) while going and returning and (b) after merging.

The other reconstruction was done by merging two maize row point clouds reconstructed when the robotic platform scanned the left side of the row while going, and the right side of the row while returning (see **Fig. 6**). In this case the robotic platform turned to the adjacent path in the headland. The theoretical advantage of this approach is that there are less hidden leaves that are not hit by the active sensing system of the TOF camera, compared to the previous one scanned from the same side. However, the average RMSE and MAPE were 1,059 cm² and 32.3%, respectively. These high errors could be explained by the poor continuity on the leaf point clouds due to the different 3-D perspective views of the opposing scans.

Table 3: Align and merge two point clouds scanned from both sides with opposite directions

Direction	Crop row	Rasterized crop height (10 mm) [cm ²]	Poisson surface reconstruction [cm ²]	Ground truth LA [cm ²]	RMSE [cm ²]	MAPE
Go left side and return right side	2	3,047	3,156	4,750	1594	33.5%
Go left side and return right side	3	1,191	2,479	1,852	627	33.8%
Go left side and return right side	4	1,560	4,150	3,195	955	29.8%
Average		1,932	3,261	3,265	1059	32.3%

**Figure 6:** Opposite direction scanned point clouds depicting the difference between the ones acquired while going from the left side of every maize row, and while returning from the right side.

4 Conclusions

A low-cost 3-D TOF camera was used to acquire 3-D data with the use of sensor fusion that tracked the pose of the camera with high precision. The results demonstrated that it was possible to estimate the LA based on the reconstructed surface (meshes) of maize rows by merging point clouds generated from different perspectives. The difference between generating the point clouds by scanning the crop row from the same side and from opposite sides were very apparent in the resulting average MAPE of 7.8% and 29.8%, respectively. Therefore, even if two point clouds were aligned and merged, the continuity of the point cloud made a considerable difference in the LA estimation. The alignment of four point clouds resulted in an average MAPE of 8.8% which is not very different from the one scanned from one side of the crop row.

References

- ANDÚJAR D, DORADO J, FERNÁNDEZ-QUINTANILLA C, RIBEIRO A (2016):** An approach to the use of depth cameras for weed volume estimation. *Sensors* 16: 1–11. doi:10.3390/s16070972.
- BRÉDA NJJ (2003):** Ground-based measurements of leaf area index: A review of methods, instruments and current controversies. *J. Exp. Bot.* 54: 2403–2417. doi:10.1093/jxb/erg263.
- DEWEZ TJB, GIRARDEAU-MONTAUT D, ALLANIC C, ROHMER J (2016):** Facets : A CloudCompare plugin to extract geological planes from unstructured 3-D point clouds. *Int. Arch. Photogramm. Remote Sens. Spat. Inf. Sci. - ISPRS Arch.* 41: 799–804. doi:10.5194/isprsarchives-XLI-B5-799-2016.
- EDF R&D, T.P. (2011):** CloudCompare (version 2.9.1) [GPL software] [WWW Document].
- HÄMMERLE M, HÖFLE B (2017):** Mobile low-cost 3D camera maize crop height measurements under field conditions. *Precis. Agric.* 1–18. doi:10.1007/s11119-017-9544-3.
- HOSOI F, NAKABAYASHI K, OMASAK (2011):** 3-D modeling of tomato canopies using a high-resolution portable scanning lidar for extracting structural information. *Sensors* 11: 2166–2174. doi:10.3390/s110202166.
- HU Y, WANG L, XIANG L, WU Q, JIANG H (2018):** Automatic non-destructive growth measurement of leafy vegetables based on Kinect. *Sensors* 18. doi:10.3390/s18030806.
- KAZHDAN M, BOLITHO M, HOPPE H (2006):** Poisson Surface Reconstruction. POLTHIER K, SHEFFER A (Eds.): Eurographics Symposium on Geometry Processing.
- KAZHDAN M, HOPPE H (2013):** Screened Poisson Surface Reconstruction. *ACM Transactions on Graphics*: 1–13. doi:http://dx.doi.org/10.1145/2487228.2487237.
- LI X, ZARAGOZA J, KUFFNER P, ANSELL P, NGUYEN C, DAILY H (2015):** Growth Measurement of Arabidopsis in 2.5D from a High Throughput Phenotyping Platform. International Congress on Modelling and Simulation. Gold Coast, Australia, 517–523.
- MONTGOMERY EG (1911):** Correlation studies in corn.
- NAKARMI AD, TANG L (2012):** Automatic inter-plant spacing sensing at early growth stages using a 3D vision sensor. *Comput. Electron. Agric.* 82: 23–31. doi:10.1016/j.compag.2011.12.011.
- PAULUS S, BEHMANN J, MAHLEIN AK, PLÜMER L, KUHLMANN H (2014):** Low-cost 3D systems: Suitable tools for plant phenotyping. *Sensors* 14: 3001–3018. doi:10.3390/s140203001.
- VÁZQUEZ-ARELLANO M, REISER D, PARAFOROS DS, GARRIDO-IZARD M, BURCE MEC, GRIEPENTROG HW (2018):** 3-D reconstruction of maize plants using a time-of-flight camera. *Comput. Electron. Agric.* 145: 235–247. doi:10.1016/j.compag.2018.01.002.

Soil type recognition with artificial intelligence during compaction process

Ulrike Nohlen¹, Robin Popelka¹, Yann Berquin²

¹*MTS Maschinentchnik Schrode AG, Ehrenfelser Weg 13, 72531 Hayingen, Germany*

²*Eberhard Karls University of Tübingen, Wilhelm-Schickard-Institute for Computer Science, Sand 1, 72076 Tübingen, Germany*

E-mail: Ulrike.Nohlen@mts-online.de Popelka@mts-online.de

Abstract: Methods of machine learning are used to recognize the soil type during soil compaction with attachment compactors. Acceleration records are measured on the vibratory plate. They are influenced by the Plate-soil-interaction and show characteristic patterns for different soil types and their humidities. The signal is processed in the frequency domain. 24 Dimensions are used for the feature extraction. Three soil classes with three relative humidities each can be detected. Together with the positioning of an excavator control system (GNSS-Position) a full 3D – protocol of the compacted soil and its density is provided. The novelty is that no calibration of the compaction control value to the proctor density is necessary.

Key words: Machine learning, construction equipment, intelligent compaction control, Attachment compactors

1 Summary

Three constructionally relevant main soil types (gravel, sand, clay) in three water content ranges (too dry, optimal, wet) can be detected. The number of different main soil types to be classified will be determined in the coming practical tests. The fundamental suitability of the chosen method (neural networks connected in series) has been confirmed, so that the further development to an application-ready practical solution is planned. First experiments with untrained data from unusual soils, such as very wet clay and crushed wet marl, showed that more physical properties than just stiffness are characteristic and are used by pattern recognition.

Beyond the application for soil type detection in compaction control, the methods of machine learning provide a toolbox that is well applicable to acceleration signals. The analysis in the frequency domain corresponds to common methods in acoustics: pattern recognition is also used very successfully in speech recognition. Perhaps our work can also provide the impetus to classify and evaluate other types of shocks and vibrations with the methods of artificial intelligence.

2 Introduction

Attachment compactors are compactors mounted on the boom of an excavator. They are widely used for the backfill of trenches and compaction of embankments. Due to the centrifugal force of the imbalance, the freely vibrating plate oscillates in a sinusoidal motion. When in contact with the ground, the sinusoidal shape changes depending on the properties of the soil and the device.



Figure 1: Attachment compactor compacting trench filling, with display screen

A characteristic feature of attachment compactors is the variable static load, which distinguishes them from other compactors such as rollers or vibratory plates. To determine the soil contact force, the static load must be measured. A display (**Fig. 1**) shows the operator of the excavator whether he presses too much or too little, whether the operating frequency is correct and when the compaction process is completed. So far, no information on the quality of the achieved compaction has been provided.

In Continuous Compaction Control (CCC) two main methods for determining soil stiffness are widely used: 1. Using the harmonic content of the acceleration signal: The total Harmonic Distortion (THD) corresponds with soil stiffness. 2. Use of the force equilibrium to calculate soil reaction force, corresponding with soil stiffness. Both methods have severe drawbacks: Especially for cohesive and mixed soils, soil stiffness corresponds rather with water content than with compaction degree. Therefore, both methods need calibration. As attachment compactors are used on small sites with locally widely varying different soil types and the static load is not a constant but a variable, both traditional methods are not sufficient.

To avoid the need of calibration and to eliminate the influence of the water content, we use machine learning methods to determine the soil type and the relative water content (wet, optimum, dry). With known machine parameters as static load, plate width etc... we can then calculate the stress distribution in the soil. The use of soil-type depending material models leads directly to the compaction degree. Together with a satellite excavator control system a full 3D-protocol is possible.

3 Methods

3.1 Prerequisites

Attachment compactors show complex and chaotic motion patterns (NOHLEN & BERQUIN, 2015). The different translatory and rotatory modes are changed spontaneously, e.g. by a slight change in the direction of static load application by the excavator. Thus, the measured acceleration or displacement amplitudes are strongly dependent on the position of the sensor on the plate. The determination of the ground contact force is nevertheless possible and provides good values, as could be shown by a comparison with the force emission spectra measured in the ground (**Fig. 2**) (JAHNKE *et al.*, 2018).

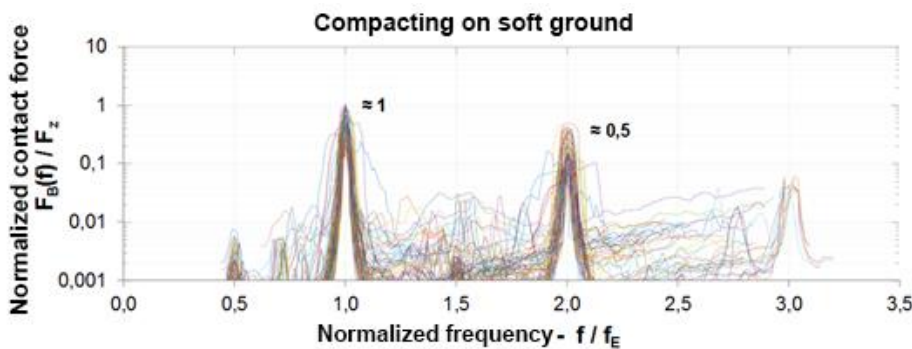


Figure 2: Normalized force emission spectra of various attachment compactors. The excitation frequency and the first harmonic are dominant (JAHNKE *et al.*, 2018).

For pattern recognition in plate-soil interaction a stable vibration without changes in the vibration mode is useful.

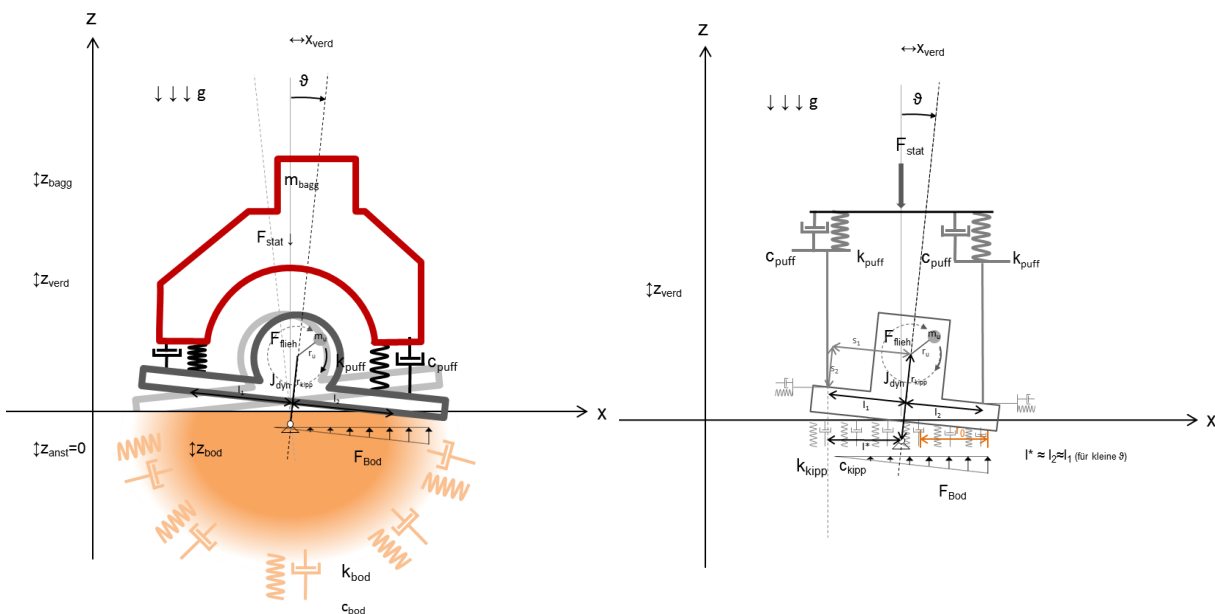


Figure 3: The compactor plate oscillates in various modes, including rocking modes (NOHLEN & BERQUIN, 2015).

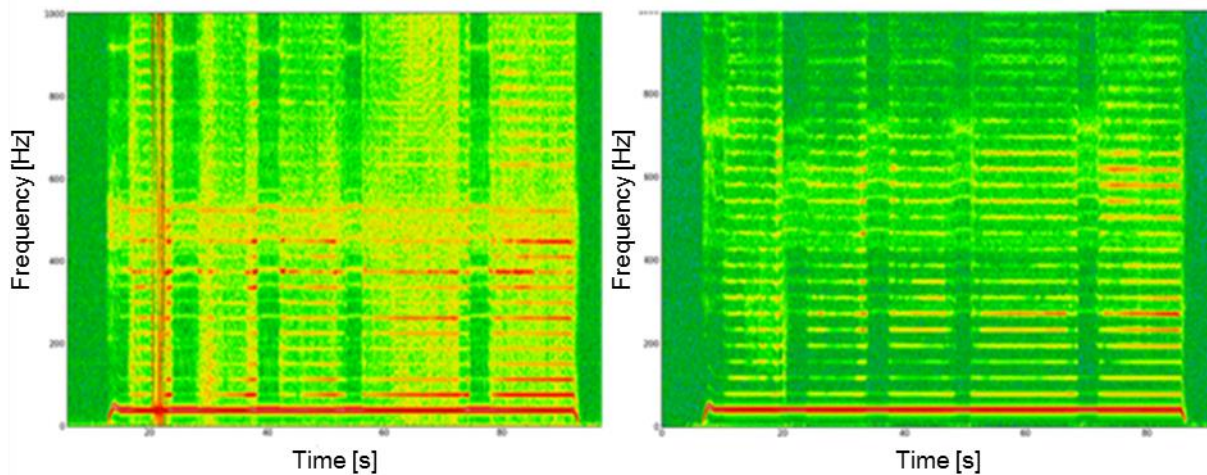


Figure 4: Typical recording of a suite of compaction processes. Recorded with two different sensor types as spectrogram.

Fig. 4 shows the increase of the harmonic content on ground contact in two data sets recorded simultaneously but with different sensors, while the excitation frequency is almost exclusively visible between the individual compactions. The absolute amplitudes and the noise, on the other hand, depend on the sensor.

3.2 Feature extraction

The amount and quality of training data are essential. Because the movement patterns depend on the Compactor type, each type must be trained separately. Changes in the vibrating mass, as they occur with model changes, can disturb the result. Therefore, we used always the same compactor (type MTS V8 WA with load sensor) to record the training data. Considering that a large number of data sets are required for each soil type and water content, and that an excavator is also required for each measurement, it is clear that the collection of training data is the bottleneck when using artificial intelligence for compaction control. The signal processing itself corresponds approximately to the usual methods of CCC (analysis in the time and frequency domain). The characteristics for soil type detection are mainly extracted at the end of the compaction process when purely elastic material behaviour is present. Feature extraction itself requires an understanding of the processes in the soil and the physical conditions of the entire compaction process. Feature extraction is partly deterministic and it is based on human expertise.

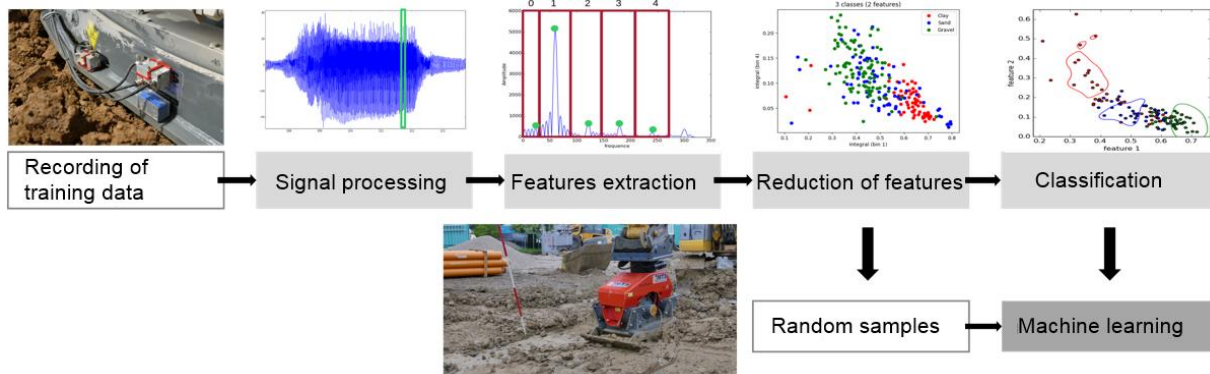


Figure 5: Schematic process of machine learning

The plate acceleration signals are best described in their Fourier domain. The peaks in Fourier domain exhibit high energy about the harmonics and subharmonics of the plate excitation frequency. The features are derived from the Fourier transform coefficients amplitude and combined Fourier transform coefficients real and imaginary part with a cutoff frequency up to 350 Hz. This describes mostly the relevant information in the signal for the classification without noisy information. The recorded data were labeled and divide into the train and test dataset.

3.3 Classifiers

The machine learning methods used in this study are based on supervised learning algorithms which make use of labeled training data. There were applied numerous popular methods such as k-NN, Support Vector Machine with linear kernel, Random Forrest, Bayesian with a Gaussian kernel and last but not least the Neural Network. Accuracy performance of all classifiers is quite similar and depends highly on the dataset. To get relevant classifiers performance there were computed the confusion matrices regarding soil materials. The misclassification occurs often with soils having closest stiffness parameters.

The neural network classifier provides decently classification results with respect to the stiffness parameters. There was experimentally designed feed forward neural network with four hidden layers, ReLu activation function for each of them and Adam optimizer. The Keras library (backend Tensorflow) was chosen for implementation this classifier in Python. There were also designed next three neural networks for the material humidity classification. The output from the first neural network determines the material and these features are used as input for the humidity neural network classifier.

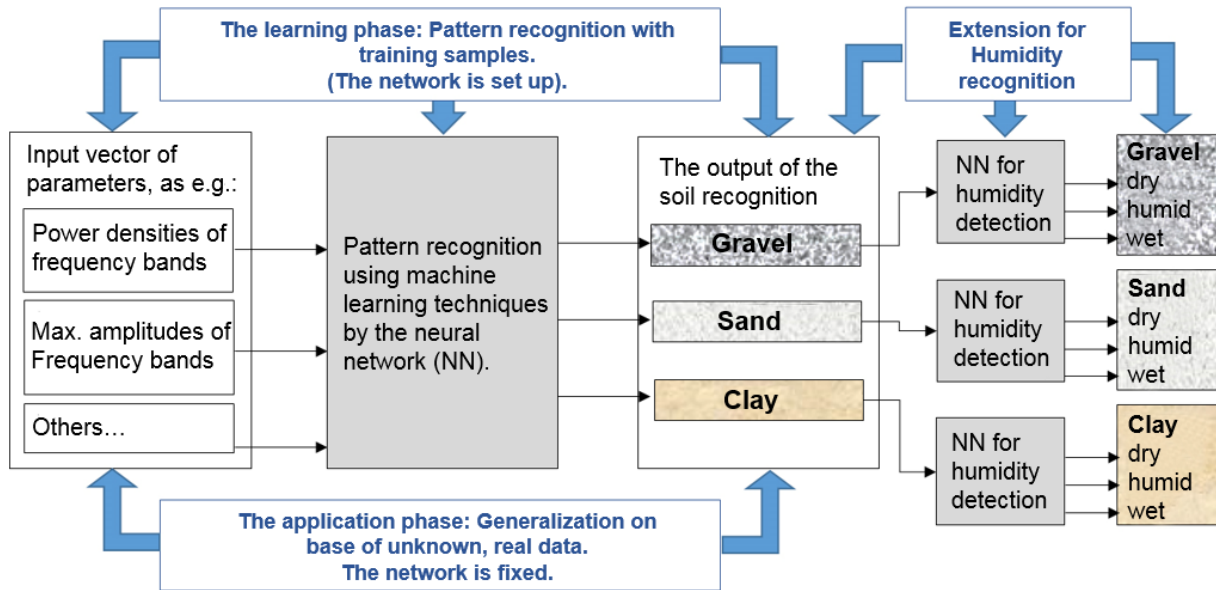


Figure 6: The procedure of machine learning with help of connected neural networks

3.4 Results

Initially, Bayesian probability density functions (Gaussian Process) were used because this approach was expected to best reflect the real conditions of mixed soil types and the continuous change in mechanical behaviour due to changes in water content. In the end, however, the neural networks proved to be the most suitable. In order to take into account the water content relative to the optimum (labelled “humid”), the soil type was first determined using a first neural network. With this result, the relative water content was then determined in a soil type-specific second neural network. This approach has proved to be advantageous, while the attempt to immediately classify the soil type and water content in a neural network, i.e. to use nine classes for three soils in three water contents, has given less good results.

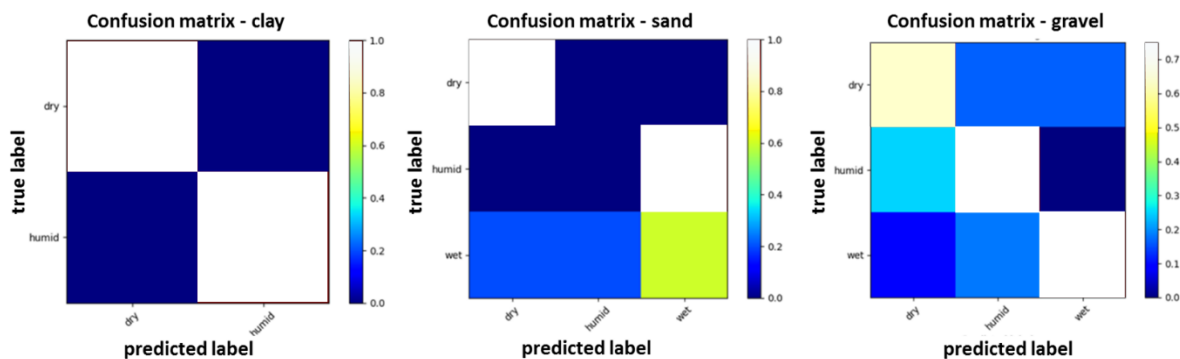


Figure 7: Confusion matrix for soil types which are relevant for construction purposes and their humidity

Fig. 7 shows the results for clay, sand and gravel in a "Confusion Matrix". If the prediction and the actual class always match, the result is a clearly separated diagonal in the matrix. Thus, dry and moist clay could be distinguished to 100 %. However, this (too) good result is due to an insufficient amount of training data for clay. The matrix for gravel, for example, shows realistically achievable good results. When looking at the soil type alone (not shown), gravel is occasionally confused with sand. Because in many cases our "gravel" was actually a "gravel sand" (high proportion of sand), this corresponds perfectly to the soil-mechanical reality.

4 Discussion

What the neural network actually does with the data is completely hidden from the user ("black box") - an unusual situation for engineers. Our concern was that the classification can ultimately only be traced back to the soil stiffness as with CCC (ADAM & KOPF, 2004). A surprising result showed that this is not the case. At first we had no training data for very wet clay. Since AI knows no limits of its own - there is no class "I don't know" - the data collected later were classified as gravel for very wet clay. The analysis of the data suggests that the saturation of the impermeable material could have led to a certain change in the harmonic content of the acceleration signals, independent of the very low stiffness. Other unknown, mixed soils, e.g. broken and slightly softened marl, are allocated to gravel and clay in a physically meaningful way.

The neural network also proved to be robust against poorly adjusted excavator hydraulics and the resulting deviations from the desired operating frequency. Further work has to show that the method is robust with regard to other influences, e.g. different types of compactors. The chosen material models have to be proved with respect to the compaction degree.

Acknowledgement

The MUSKETIER project was funded by the BMBF within the "IKT 2020" programme. The cooperation project of MTS AG, the Universität Tübingen and the Technische Universität Bergakademie Freiberg started in April, 2015 and ended in June, 2018.

References

- ADAM D, KOPF F (2004):** Operational devices for compaction optimization and quality control. GOMES CORREIA, LOIZOS (hrsg.): proceedings of the International Seminar on Geotechnics in Pavement and Railway Design and Construction, 16-17 December 2004 Athens, Greece, Millpress Rotterdam. Paper Nr. 6: 97-106,
- GÉRON A (2018):** Praxiseinstieg Machine Learning mit Scikit-Learn und TensorFlow: Konzepte, Tools und Techniken für intelligente Systeme. O'Reilly, USA.

- JAHNKE R, MISTLER M, NOHLEN U (2018):** Untersuchungen der Erschütterungsemissionen von Anbauverdichtern. VDI Wissensforum GmbH, VDI-Berichte 2321, 6. VDI-Fachtagung Baudynamik, 17-18 April 2018, Würzburg, Germany. Paper Nr. 7: 53-62.
- MOONEY MA, FACAS NW (2013):** Extraction of Layer Properties from Intelligent Compaction Data, Highway IDEA Program report, NCHRP145, Colorado.
- NOHLEN U, BERQUIN Y (2015):** Selbstlernende Verdichtungskontrolle mit Bodenarterkennung. Fachtagung Baumaschinentechnik 2015: Maschinen, Prozesse, Vernetzung. 17-18 September 2015, Dresden. Paper Nr. 24: 315-328.
- NOHLEN U, KONIETZKY H (2014):** Boom-mounted vibratory plates: Machine Parameters and modelling of dynamic compaction of cohesive soils. BRANDL H & ADAM D (Eds.), XV Danube - European Conference on Geotechnical Engineering (DECGE 2014), Vienna. Paper Nr. 125: 249-254. ÖIAV Österreichischer Ingenieur- und Architektenverein Wien.
- NOHLEN U, POPELKA R, BERQUIN Y (IN PRESS):** Raumfüllende Verdichtungskontrolle: Bodenarterkennung mit künstlicher Intelligenz am Anbauverdichter. ADAM D & LARSSON S (eds.), Anniversary Symposium – 40 Years of Roller Integrated Continuous Compaction Control (CCC) 29. November 2018, Vienna, Austria.
- NOHLEN U, POPELKA R, BERQUIN Y (2018):** Bodenarterkennung mit künstlicher Intelligenz am Anbauverdichter. 21. Symposium Bauwerksdynamik und Erschütterungsmessungen 15. Juni 2018, Dübendorf, Switzerland.

UAV-based Growth Rate Determination in Winter Wheat

Diana Becirevic¹, Lasse Klingbeil¹, Andreas Honecker², Henrik Schumann², Jens Léon², Heiner Kuhlmann¹

¹*Institute of Geodesy and Geoinformation, University of Bonn, Germany*

²*INRES Plantbreeding, University of Bonn, Germany*

E-mail: becirevic @igg.uni-bonn.de, tel.: +49 (0)228 73-3571

Abstract: Using Structure from motion technology based on aerial imagery to monitor crop growth has become very popular in recent years. 3D data, captured during a full growing season, can provide useful multi-temporal information to plant breeders. A georeferenced geometrical parameter extraction workflow from eight flight epochs, using RGB camera images is presented. Here we especially consider important steps, like the reference surface generation and representation and different methods for calculating the differences between the crop and the reference surface. The plant heights were calculated based on two different approaches for a winter wheat test field. One goal is to have a better insight into the single step of each method and clarify what is really happening with the data and what are the possible influences and consequences to our final calculation of plant height from UAV based images.

Key words: UAV imagery, structure from motion, georeferencing, 3D crop structure, heights raster data, plant height, growth rate

1 Introduction

Field-based phenotyping has become a very interesting component within the crop production process. It is capable to take into account genetical and environmental related factors, as well as their interaction in real-world cropping system (YANG *et al.*, 2017). So far, most of the field based phenotyping methods have been destructive, subjective and labor intensive. In recent years, the use of semi-automated or fully automated wheeled platforms deploying multiple sensors have become very popular but they still require a lot of time to cover the whole area of interest (ZHANG & KOVACS, 2012). Some of the limitations can be solved using satellite-based remote sensing technologies (GEVAERT *et al.*, 2015), which have become a very useful tool for agricultural applications. However, the possibilities of clouds within the satellites view, and the lack of spatial and temporal resolution are some limitations that require alternatives. Low-altitude, flexible, and affordable Unmanned Aerial Vehicles (UAV) have become a reasonable alternative, which allows collecting data with high spatial, spectral, and temporal resolution. They are frequently used within crop related research activities in order to access the precision and efficiency of field-based crop phenotyping. A real time monitoring of the fields from above and near real time extraction of the parameters which supports decision-making, has become a hot topic for many plant breeders worldwide. Using UAVs for a

simple visual inspection (crop scouting) is not satisfying anymore; breeders want to have more indicators to optimize their agronomic practices. Georeferenced spatial and temporal highly resolved data from the field are able to support these needs. Geometrical traits, such as plant height and growth rate, ground cover, leaf area index, emergence or lodging have the potential to be rapidly and non-destructively obtained using UAV imagery.

In this paper, we focus on plant height as the parameter of interest in the field. Plant height is recognized as a good indicator for biomass, expected yield, lodging, crop stress or water stress (MEDAC *et al.*, 2017). When multi-temporal data are used, crop height time series and growth rate curves can be calculated. Currently, the most common method for measuring plant height is the manual measurement with a ruler, which is time consuming, labor-intensive as well as subjective, regarding the actual measuring procedure. An alternative way of plant height determination is to derive 3D models from overlapping aerial images. In order to extract the plant heights from 3D data (e.g. point clouds), it is necessary to calculate the difference between the crop surface and the reference surface, which is usually the bare soil without any plants. Probably the most common and efficient approach (e.g. BENDIG *et al.*, 2014) is to generate digital surface models (DSM) using structure from motion software (e.g. Agisoft Photoscan or Pix4D) (URL-1, URL-2) and subtract the digital elevation model (DEM) of a field at a time, before the plants have been emerged. However, it is not clear, if this is the best option. In the following, we will compare and discuss several methods for plant height extraction and compare them. A more detailed view at the reconstructed 3D data and a better insight at the single step of each method can clarify what is really happening with the data and what are the possible influences and consequences to our final calculation. In this way, we can define a reliable workflow for future projects. Finally, we will present a plant height time series of a multifactorial experiment with different winter wheat genotypes and different seeding systems.

2 Materials and Methods

2.1 Generating 3D models

Automated aerial and close-range digital photogrammetry has become a powerful and widely used tool for three-dimensional modelling. 'Structure-from-Motion' (SfM) photogrammetry is often described as revolutionary, low-cost, user-friendly photogrammetric technique for obtaining high-resolution data sets (WESTOBY *et al.*, 2012). SfM uses multiple overlapped images of an object or feature to create a three-dimensional set of points corresponding to the surface of the feature. Images are taken from numerous positions focusing on the same object. The overlapping ensures finding matching points in multiple images that belong to the same spot on the ground but from a different perspective. Then these matched features in multiple images are used to estimate relative camera position, which is then extrapolated to create a 3D point cloud of the scene. Fur-

thermore, the points can be processed to represent the 3D structure in the form of a DEM or some sort of surface representation, such as a triangulated mesh.

In order to compare the generated 3D data at different epochs (**Fig. 1**), it is necessary to georeference them. This is usually realized by the usage of ground control points (GCPs). GCPs are previously deployed in the area of interest and measured with GNSS or some other surveying technique. There is also an alternative georeferencing method without GCPs, but using on-board RTK (Real-Time Kinematic) GNSS observations to geotag the images with an accuracy of several centimeters.



Figure 1: Point clouds of eight flights, shown together as a cross section to visualize the different heights

2.2 Generation of the reference surface

For measuring the plant height using 3D crop surface data, it is necessary to know the structure and position of the ground without any plants. The most accurate method to create this reference surface is to generate a 3D model (point cloud, DEM or mesh) of the surface, shortly before the plants emerge, and then assume, that the surface does not significantly change during the growing season. However, it may be the case, that a flight at that point in time is not possible. An alternative option is to use an early season flight with sufficiently visible ground segments between the plants. Then the plant points can be removed from the resulting point cloud, while the remaining ground points are used to create a 3D representation of the reference surface, e.g. by interpolation. We do not go into details here, but **Fig. 2** shows (a) a point cloud of an early season flight of winter wheat, and (b,c) points separated into ground and plant points. The classification into the two classes was realized by applying a threshold to the Excess Green Index (ExG, MEYER & NETO, 2008), which can be calculated from standard RGB images.

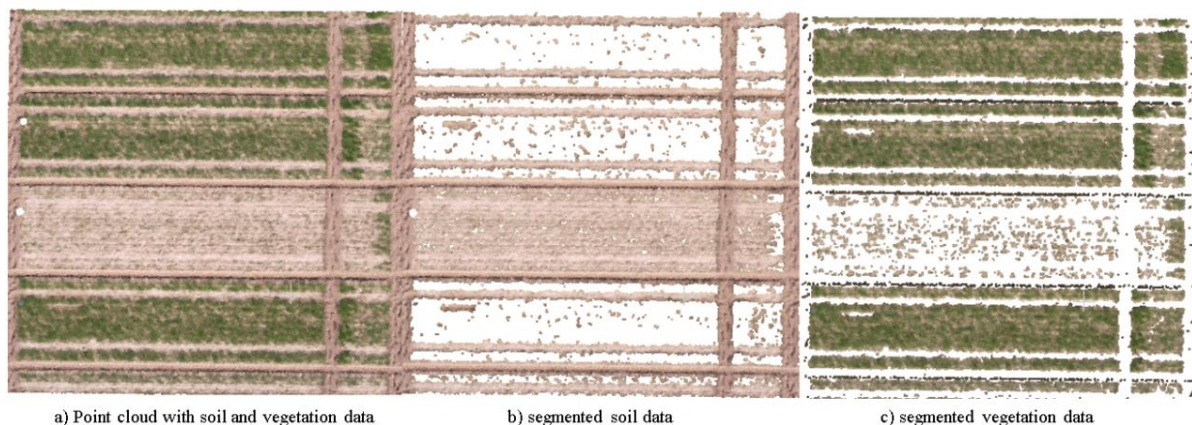


Figure 2: Segmentation between soil and vegetation data

For the sake of completeness, we also want to mention a third option to generate a reference surface, especially if no ground is visible anymore in the aerial images. Then, RTK-GNSS surveying equipment can be used to measure samples of the ground surface with a sufficient density and interpolate these sampled points. Obviously, the accuracy of this method depends on the GNSS accuracy and the structure of the surface.

2.3 Distance calculation using point clouds

The next processing step is the calculation of the distance between the crop surface and the reference surface, in order to get the plant height. In this section, we briefly describe three possibilities of calculating this distance directly using the point clouds. The Cloud to cloud distance (C2C) is based on the distance between two point cloud using a 'nearest neighborhood' approach. For each point of the compared cloud, the algorithm searches the nearest point in the reference cloud and computes their Euclidean distance. If the reference point cloud is dense enough, approximating the distance from the compared cloud to the underlying surface represented by the reference cloud is acceptable. If the reference cloud is not dense enough, the nearest neighbor distance is sometimes not precise enough (**Fig. 3a**, left). Often, a local model is fitted to the reference surface close to the point of interest, in order to reduce this error (**Fig. 3a**, right). The Cloud to mesh distance (C2M) calculates the distance between the point cloud and a reference surface represented as a mesh. If the reference point cloud is triangulated to a mesh, then the C2M algorithm calculated the distance of a point to the closest triangle of the mesh. In Multiscale model to model cloud (M3C2) comparisons, the number of points of one epoch is reduced by building core points that should represent the geometry of their neighborhood of size D . These core points are gained by filtering. The difference to the other point cloud is then calculated along each core point's normal vector regarding its neighborhood d . Hence, two neighborhoods of size D and d need to be specified for this point cloud comparison. For a more detailed explanation, see BARNHART & CROSBY (2013).

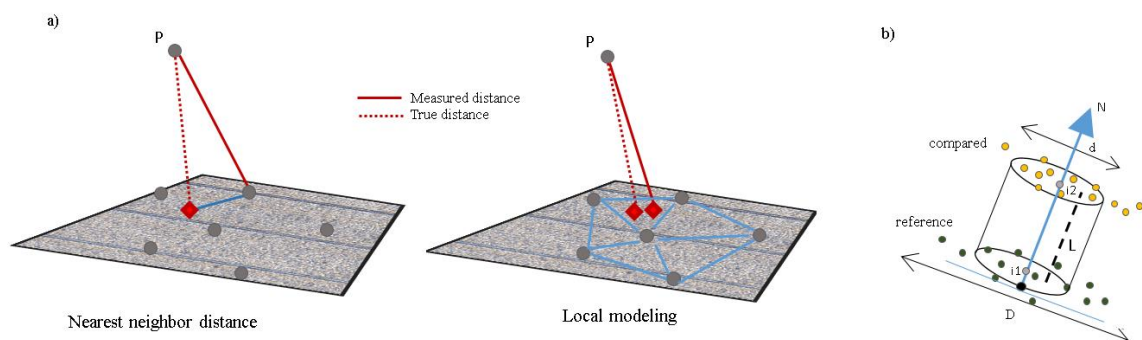


Figure 3: a) Cloud to cloud distance concept and b) M3C2 distance concept

The three algorithms described above are implemented in the software Cloud Compare (URL-3).

2.4 Distance calculation based on rasterized data

Since crop surfaces are mainly horizontal structures, and since the parameter of interest is the vertical distance between these surfaces, the rasterization of the surfaces and a simple distance calculation between the raster data may be the most effective way to calculate plant height values. The processing steps are (1) calculate heights raster from reference surface point cloud, (2) calculate heights raster from crop surface point cloud, (3) subtract the reference surface raster from the crop surface raster. There are several questions, which need to be considered during the process: (a) what is the most suitable cell size, (b) how is the cell height calculated from the point heights within one cell (e.g. max, mean or median), (c) what to do with empty cells? The answers to these questions may be different for the ground and the crop surface raster. Although SfM software packages provide these raster data (in the form of a DEM) very easily, it is unknown, what their answers to the questions are.

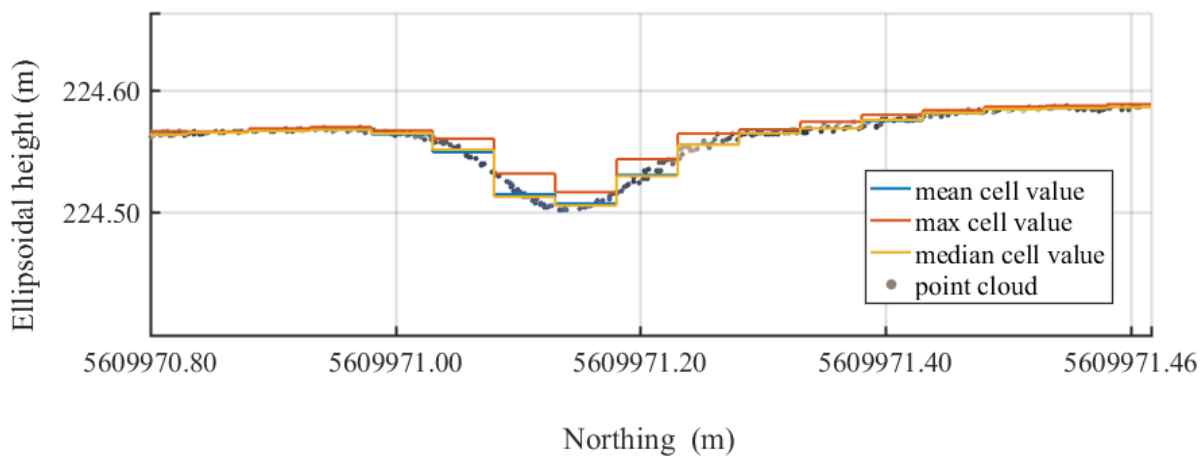


Figure 4: Rasterization of reference surface. Cross section

Fig. 4 shows the effect of rasterization using different methods for cell calculation in the example of the reference surface. The plot shows the cross section of a point cloud, cut along the North-South direction. We see here one line of cells with their points and their rasterization values for the different methods. Here, a 5cm cell size was chosen as it is assumed, that changes with a smaller scale are likely to happen during the season due to rain, erosion and field management. The median appears to be the preferred method as it is more robust to outliers, than the mean or the max value.

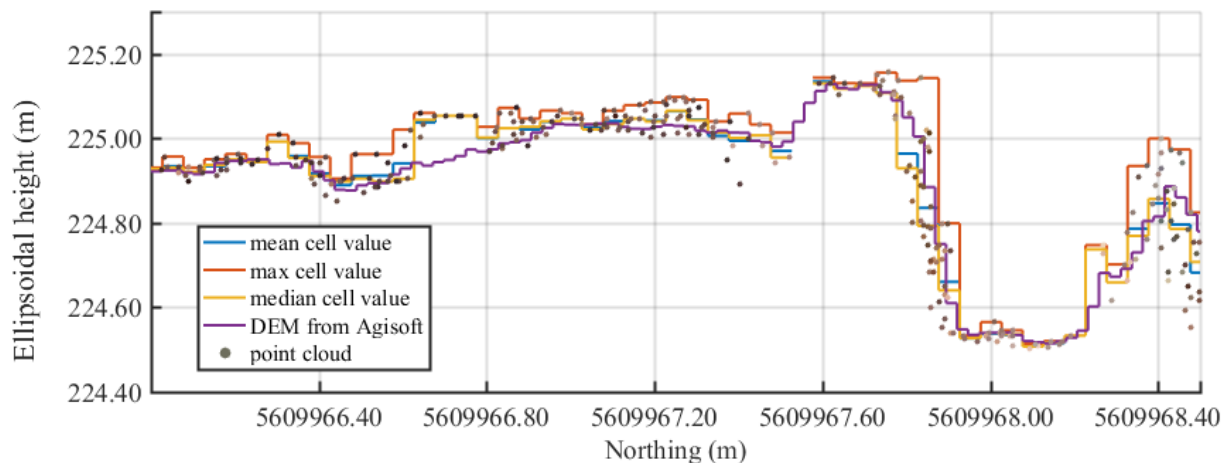


Figure 5: Rasterization of crop surface. Cross section

Fig. 5 shows the same plot, but now based on a crop surface point cloud. It can be assumed, that the maximum values within a cell are the best representation of the actual plant height. The reconstruction algorithms of the SfM software tend to smooth the surface and the building of a mean of heights within one cell would even increase this effect, leading to an underestimation of the plant height. In the plot this can be seen in some places, where the mean and the max cell values differ. Obviously, it is necessary to remove outliers in the point cloud, as they appear directly in the cell, if they show higher height values. The figure also shows the rasterization result (DEM) from Airsoft. We assume, that here a mean or median was used, and that a strong outlier reduction, sacrificing some crop surface points, has been performed. The cell size is chosen to be small, as long as there still enough points within one cell. Here we used a cell size of 2 cm. In order get the plant height, the crop surface raster and the reference raster are simply subtracted.

2.5 Field experiment

Multi-temporal plant height measurements in a winter wheat experimental field are presented. It consisted of 96 plots with 12 different genotypes and two different seeding treatments: an intensive treatment with 330 seeds per square meter and 200 kg/ha N fertilization, and an extensive treatment with 165 seeds per square meter and 100 kg/ha N fertilization. Eight UAV flights have been performed between March and July in 2017 at the Uni Bonn Campus in Klein Altendorf. The reference flight was performed before plant emergence in early December 2016. The UAV was a DJI Matrice 100, equipped with and DJI Zenmuse X5 camera with 3-Axis Gimbal and 15mm f/1.7 lens. Each mission was programmed as a cross flight pattern at two heights (25m and 30m, side and forward overlap ~70%), to achieve a better 3D data quality. For data georeferencing, nine GCPs have been previously deployed and measured with a Leica GNSS receiver.

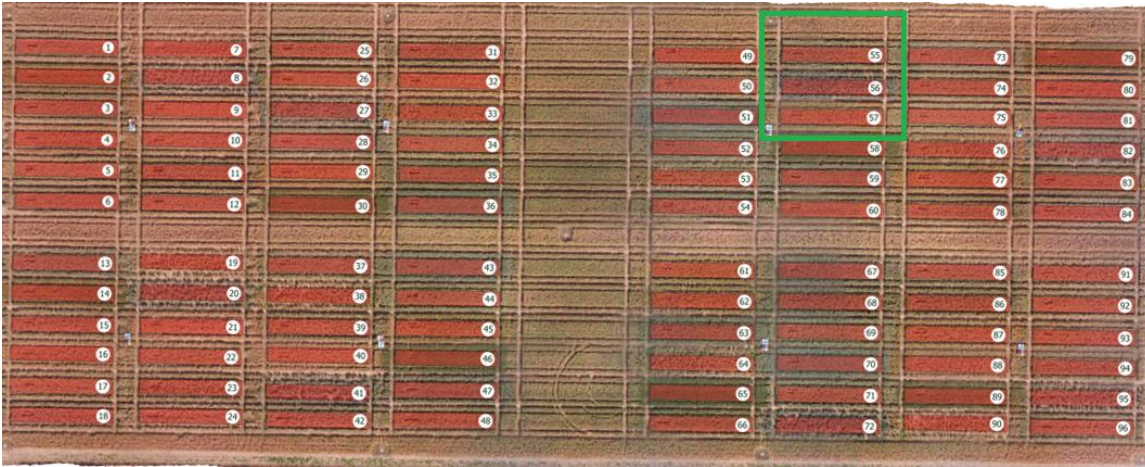


Figure 6: Field experiment. Test area in green

3 Results and Discussion

3.1 Height calculation methods

From each UAV mission a point cloud has been calculated using Agisoft Photoscan (medium resolution, moderate filtering). Based on these point clouds we calculated the crop heights using the methods described in 2.3 and 2.4. In order to compare the results, we show the histogram of heights (Fig. 7) for each of the methods, but limited to the test area shown at Fig. 6 as a green square. It can be seen, that all methods have almost the same behavior and crop heights have same distribution with three peaks. The Agisoft DEM based results seem to have a tendency towards lower values, which confirms our conclusion about smoothing the surface and building of a mean of heights sacrificing some crop surface points. However, it can be concluded, that the distribution of measured heights using the different methods do not differ more than a few centimeters.

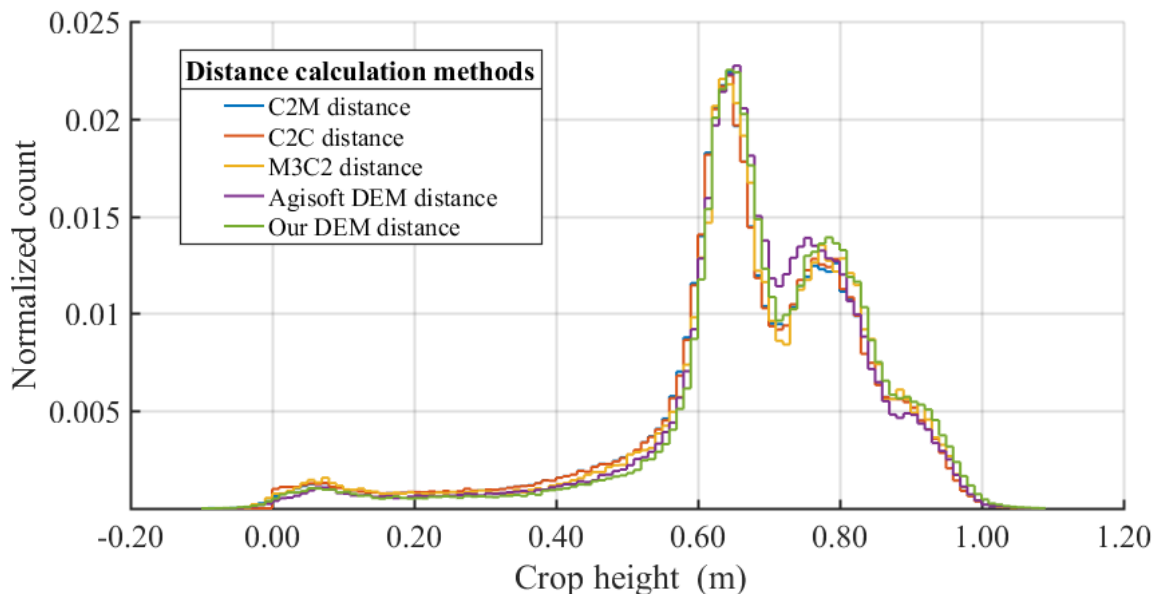


Figure 7: Crop height of test area calculated from different methods

3.2 Field experiment

Fig. 8 shows the height (left) and growth rate (right) time series for the different genotypes in the extensive seeding system. The heights have been calculated using the raster method, described in 2.3 using median cell value for reference raster and maximum cell value for crop surface. The values in the curves show the mean value of all raster cells of a particular genotype. The plot dimensions were 10 m by 1.50 m and four plots have the same genotype and management system. A buffer zone of 24 cm around each plot was excluded from the calculation to avoid border effects. Although we do not discuss these results from an agricultural perspective, it is obvious, that this information is potentially useful for breeders.

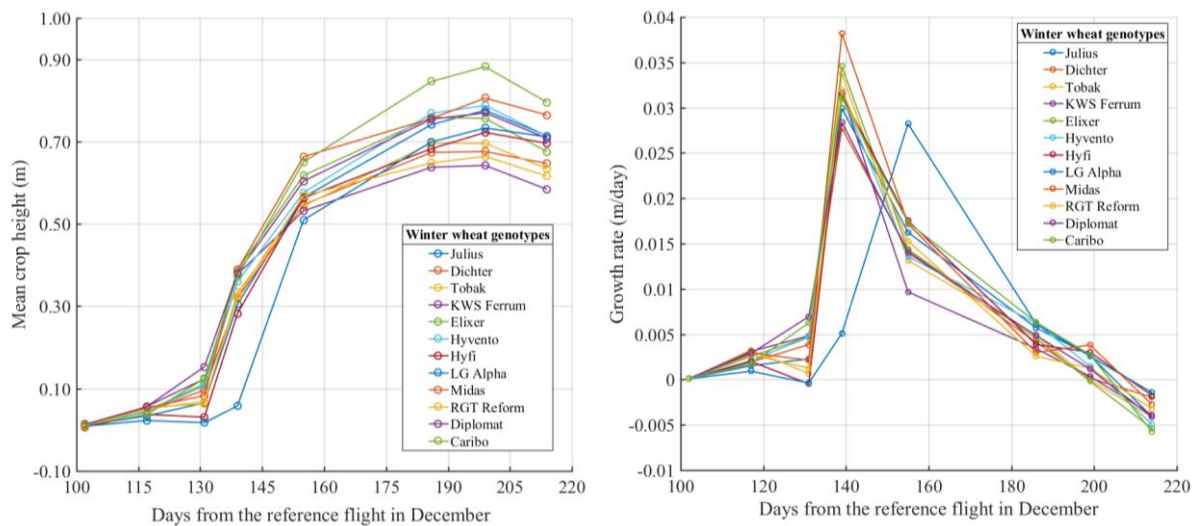


Figure 8: Mean crop height (left) and growth rate (right) for the extensive seeding system

4 Summary

We presented a workflow for generating growth rate curves and crop height time series from aerial images, which have been recorded using a UAV equipped with a RGB camera. The images were processed to derive 3D information about the crop surface, which is then compared to a 3D model of the bare soil in order to derive the crop height. We discussed and compared different methods for representing the measured surfaces and for calculating differences between them. The height distributions of a sample area differ only in the range of a few cm for the different differencing methods. Therefore, the most efficient method, which is based on a rasterization of the point cloud is suggest to be used in the future. However, we also suggest to use the maximum height value within the rasterization routine, as it represents a more realistic estimation of the plant height than the standard mean operation.

Acknowledgment

This work was funded by the German Federal Office for Agriculture and Food (BLE).

References

- BARNHART TB, CROSBY BT (2013):** Comparing two methods of surface change detection on an evolving thermoskarst using high-temporal-frequency terrestrial laser scanning, Selawik River, Alaska. *Remote Sensing* 5(6), 2813-2837.
- BENDIG J, BOLTEN A, BENNERTZ S, BROSCHEIT J, EICHFUSS S, BARETH G (2014):** Estimating Biomass of Barley Using Crop Surface Models (CSMs) Derived from UAV-Based RGB Imaging. *Remote Sens.* 6: 10395-10412, DOI:10.3390/rs61110395.
- GEVAERT CM, SUOMALAINEN J, TANG J, KOOISTRA L (2015):** Generation of Spectral–Temporal Response Surfaces by Combining Multispectral Satellite and Hyperspectral UAV Imagery for Precision Agriculture Applications. *IEEE Journal of Selected Topics in Applied Earth Observations and Remote Sensing* 8(6, June 2015), DOI: 10.1109/JSTARS.2015.2406339.
- GRENZDÖRFFER GJ (2014):** Crop height determination with UAV point clouds. *The International Archives of the Photogrammetry, Remote Sensing and Spatial Information Sciences XL-1*, 2014, ISPRS Technical Commission I Symposium, 17 – 20 November 2014, Denver, Colorado, USA.
- MADEC S, BARET F, DE SOLAN B, THOMAS S, DUTARTRE D, JEZEQUEL S, HEMMERLÉ M, COLOMBEAU G, COMAR A (2017):** High-Throughput Phenotyping of Plant Height: Comparing Unmanned Aerial Vehicles and Ground LiDAR Estimates. *Front. Plant Sci.* 27, DOI:10.3389/fpls.2017.02002.
- MEYER GE, NETO JC (2008):** Verification of color vegetation indices for automated crop imaging applications. *computers and electronics in agriculture* 63: 282–293, DOI: 10.1016/j.compag.2008.03.009.
- WESTOBYA MJ, BRASINGTON J, GLASSERA NF, HAMBREY MJ, REYNOLD JM (2012):** Structure-from-Motion' photogrammetry: A low-cost, effective tool for geoscience applications. *Geomorphology* 179, 15 December 2012: 300-314, DOI: 10.1016/j.geomorph.2012.08.021.
- YANG G, LIU J, ZHAO C, LI Z, HUANG Y, YU H, XU B, YANG X, ZHU D, ZHANG X, ZHANG R, FENG H, ZHAO X, LI Z, LI H, YANG H (2017):** Unmanned Aerial Vehicle Remote Sensing for Field-Based Crop Phenotyping: Current Status and Perspectives. *Front Plant Sci.* DOI: 10.3389/fpls.2017.01111.

URL- 1: Agisoft PhotoScan: <http://www.agisoft.com/>

URL-2: Pix4D - Professional drone mapping and photogrammetry software: <https://pix4d.com/>

URL-3: CloudCompare: <http://www.cloudcompare.org>

Paper Index

UAV-based Growth Rate Determination in Winter Wheat <i>Diana Becirevic, Lasse Klingbeil, Andreas Honecker, Henrik Schumann, Jens Léon, Heiner Kuhlmann</i>	128
Some challenges to address in order to target the second generation of agricultural robots <i>Michel Berducat</i>	5
Development of a learning tractor implements coupling application <i>Tobias Blume, Ilja Stasewitsch, Jan Schattenberg, Ludger Frerichs</i>	12
Autonomous phenotyping using a mobile manipulator <i>Camille Dubos, Roland Lenain, Michel Berducat, Frédéric Cointault</i>	27
Kinematic Positioning in a Real Time Robotic Total Station Network System <i>Gabriel Kerekes, Volker Schwieger</i>	35
Adaptive Control for Guidance of Tracked Vehicles <i>Otto Lerke, Volker Schwieger</i>	83
Soil type recognition with artificial intelligence during compaction process <i>Ulrike Nohlen, Robin Popelka, Yann Berquin</i>	120
In-field position accuracy at the millimetre level using a total station: Validation using an industrial robotic arm <i>Dimitris S. Paraforos, Marcus Reutemann, Galibjon Sharipov, Roland Werner, Hans W. Griepentrog</i>	44
Cooperative localization based on range-only measurements from robots and infrastructure <i>Cyrille Pierre, Roland Chapuis, Romuald Aufrère, Jean Laneurit, Christophe Debain</i>	62
Towards motor control adjustment with inertial sensor measurements for small differential drive robots <i>David Reiser, Marvin Hubl, Hans W. Griepentrog</i>	95
Representation Learning for Segment Matching for Future Applications in Relative Positioning of Machinery <i>Julian Schmiemann, Jan Schattenberg, Ludger Frerichs</i>	52
Comparison of controls for a stereo camera based reversing assistance system for vehicle trailer combinations <i>Ilja Stasewitsch, Tobias Blume, Jan Schattenberg, Ludger Frerichs</i>	74
Automatic machine and implement identification of an agricultural process using machine learning to optimize farm management information systems <i>Thoralf Stein, Henning J. Meyer</i>	19
Concept and first results of a field-robot-based on-the-go assessment of soil nutrients with ion-sensitive field effect transistors <i>Vadim Tsukor, Stefan Hinck, Walter Nietfeld, Frank Lorenz, Elena Nadjenko, Andreas Möller, Daniel Mentrup, Tino Mosler, Arno Ruckelshausen</i>	102
Leaf area estimation of reconstructed maize plants using a time-of-flight camera <i>Manuel Vázquez-Arellano, David Reiser, Dimitris S. Paraforos, Miguel Garrido-Izard, Hans W. Griepentrog</i>	110

Volumes published in the series**“Bornimer Agrartechnische Berichte”:**

Heft 1	Technik und Verfahren der Landschaftspflege	1992
Heft 2	Beiträge zur Lagerung und Verarbeitung pflanzenbaulicher Produkte	1993
Heft 3	Technik und Verfahren in der Tierhaltung	1993
Heft 4	Technik und Verfahren der Landschaftspflege und für die Verwendung der anfallenden Materialien	1994
Heft 5	Verfahrenstechnik der Aufbereitung, Lagerung und Qualitätserhaltung pflanzlicher Produkte	1994
Heft 6	Biokonversion nachwachsender Rohstoffe und Verfahren für Reststoffbehandlung	1994
Heft 7	Preußische Versuchs- und Forschungsanstalt für Landarbeit und Schlepperprüffeld in Bornim 1927 bis 1945	1995
Heft 8	Qualitätssicherung und Direktvermarktung	1996
Heft 9	Konservierende Bodenbearbeitung auf Sandböden	1996
Heft 10	Anwendung wärme- und strömungstechnischer Grundlagen in der Landwirtschaft	1996
Heft 11	Computer-Bildanalyse in der Landwirtschaft Workshop 1996	1996
Heft 12	Aufbereitung und Verwertung organischer Reststoffe im ländlichen Raum	1996
Heft 13	Wege zur Verbesserung der Kartoffelqualität durch Verminderung der mechanischen Beanspruchung	1997
Heft 14	Computer-Bildanalyse in der Landwirtschaft Workshop 1997	1997
Heft 15	Technische und ökonomische Aspekte der Nutztierhaltung in großen Beständen	1997
Heft 16	11. Arbeitswissenschaftliches Seminar	1997
Heft 17	Nachwachsende Rohstoffe im Land Brandenburg Stand Aktivitäten und Perspektiven einer zukunftsfähigen und umweltgerechten Entwicklung	1998
Heft 18	Qualität von Agrarprodukten	1998
Heft 19	Computer-Bildanalyse in der Landwirtschaft Workshop 1998	1998
Heft 20	Beiträge zur teilflächenspezifischen Bewirtschaftung	1998
Heft 21	Landnutzung im Spiegel der Technikbewertung – Methoden Indikatoren, Fallbeispiele	1998

Heft 22	Kriterien der Nachhaltigkeit in der Verfahrensentwicklung für die Nutztierhaltung	1999
Heft 23	Situation und Trends in der Landtechnik / Erneuerbare Energien in der Landwirtschaft	1999
Heft 24	Institut für Landtechnik der Deutschen Akademie der Landwirtschaftswissenschaften zu Berlin 1951 bis 1965	1999
Heft 25	Computer-Bildanalyse in der Landwirtschaft Workshop 1999 / 2000	2000
Heft 26	Computer-Bildanalyse in der Landwirtschaft Workshop 2001	2001
Heft 27	Approaching Agricultural technology and Economic Development of Central and Eastern Europe	2001
Heft 28	6 th International Symposium on Fruit, Nut, and Vegetable Production Engineering	2001
Heft 29	Measurement Systems for Animal Data and their Importance for Herd Management on Dairy Cow Farms	2002
Heft 30	Produktion, Verarbeitung und Anwendung von Naturfasern	2002
Heft 31	Computer-Bildanalyse in der Landwirtschaft Workshop 2002	2002
Heft 32	Biogas und Energielandwirtschaft - Potenzial, Nutzung, Grünes Gas TM , Ökologie und Ökonomie	2003
Heft 33	Sozioökonomische Aspekte zu Perspektiven des Offenlandmanagements	2003
Heft 34	Computer-Bildanalyse in der Landwirtschaft Workshop 2003	2003
Heft 35	Energieholzproduktion in der Landwirtschaft Potenzial, Anbau, Technologie, Ökologie und Ökonomie	2004
Heft 36	High-Tech Innovationen für Verfahrensketten der Agrarproduktion. Statusseminar 2003	2004
Heft 37	Computer-Bildanalyse in der Landwirtschaft Workshop 2004	2004
Heft 38	Die Landmaschinenprüfung in der DDR 1951-1991 und ihre Vorgeschichte	2004
Heft 39	Energieverlust und Schimmelpilzentwicklung bei der Lagerung von Feldholz-Hackgut	2005
Heft 40	Computer-Bildanalyse in der Landwirtschaft Workshop 2005	2005
Heft 41	Demonstration der Langzeitwirkung bedarfsorientierter Fungizidbehandlung mit dem CROP-Meter	2005
Heft 42	Biochemicals and Energy from Sustainable Utilization of herbaceous Biomass (BESUB)	2005

Heft 43	Ozontes Waschwasser zur Qualitätssicherung leichtverderblicher Produkte - Entwicklung einer <i>Fuzzy-Logic</i> -Steuerung des Waschprozesses	2005
Heft 44	Messsystem zur Bewertung des Unkrautvorkommens	2005
Heft 45	Anwendung der Thermographie zur Optimierung der Belüftungssteuerung bei der Lagerhaltung landwirtschaftlicher Produkte	2005
Heft 46	Membranbioreaktor zur Aufbereitung von Schlachthofabwässern Prozesssteuerung von Biogasanlagen mit Kofermentation	2005
Heft 47	Verschleißeinfluss auf das Förderverhalten von Drehkolbenpumpen	2005
Heft 48	Qualitätserhaltung und Qualitätssicherung von Bioobst und Biogemüse in der Nachernte	2005
Heft 49	Miniaturisiertes Datenerfassungs-System zum Implantieren in Früchte und zur Messung ihrer mechanischen Belastung durch Ernte- und Nachernteverfahren	2005
Heft 50	Prozesskontrolle der Qualität von frischem Obst und Gemüse mit Hilfe eines Multigas-Sensors	2005
Heft 51	Entwicklung eines Echtzeitsensors für die Stärkebestimmung bei Kartoffeln als funktionaler Bestandteil eines optoelektronischen Verleseautomaten	2005
Heft 52	Optimierte Steuerung von Getreide-Schachttrocknern	2005
Heft 53	Möglichkeiten und Grenzen der energetischen Nutzung von Rizinusöl	2005
Heft 54	Non-Destructive Methods for Detecting Health-Promoting Compounds COST Action 924 Working Group Meeting	2005
Heft 55	4 th IFAC / CIGR Workshop Control Applications in Post - Harvest and Processing Technology (CAPPT 2006) 26th - 29th March 2006, Potsdam, GERMANY	2006
Heft 56	Computer-Bildanalyse in der Landwirtschaft Workshop 2006	2006
Heft 57	Kontrolle der Frische in der Nacherntekette von Ökogemüse	2006
Heft 58	Entwicklung eines innovativen Dekontaminationsverfahrens als Technologieantwort auf zukünftiges Qualitätsmanagement im Nacherntebereich	2006
Heft 59	Experimental Studies and Mathematical Modelling of Solar Drying System for Production of High Quality Dried Tomato	2007
Heft 60	13. Workshop Computer-Bildanalyse in der Landwirtschaft & 4. Workshop Precision Farming	2007

Heft 61	Energiepflanzen im Aufwind Wissenschaftliche Ergebnisse und praktische Erfahrungen zur Produktion von Biogaspflanzen und Feldholz	2007
Heft 62	14. Workshop Computer-Bildanalyse in der Landwirtschaft	2008
Heft 63	Experten-Workshop Lagerung von Holzhackschnitzeln	2008
Heft 64	Postharvest unlimited 2008	2008
Heft 65	Vom Agrarrohstoff zu neuen Produkten – Verfahrens- technische Forschung im Nacherntebereich	2009
Heft 66	16. Arbeitswissenschaftliches Kolloquium des VDI-MEG Arbeitskreises Arbeitswissenschaften im Landbau	2009
Heft 67	Monitoring der methanbildenden Mikroflora in Praxis- Biogasanlagen im ländlichen Raum: Analyse des Ist- Zustandes und Entwicklung eines quantitativen Nachweissys- tems	2009
Heft 68	Wieviel Biogas steckt in Pflanzen? Abschluss- Symposium des "Biogas-Crops-Network" (BCN) 7. Mai 2009 Potsdam	2009
Heft 69	Image Analysis for Agricultural Products and Processes 27 to 28. Aug. 2009 Potsdam	2009
Heft 70	5th International Technical Symposium on Food Processing, Monitoring Technology in Bioprocesses and Food Quality Management 31. Aug. to 02. Sept. 2009 Potsdam	2009
Heft 71	Einsatz von Biogas in PEM-Brennstoffzellen	2009
Heft 72	Teilflächenspezifische Grunddüngung	2009
Heft 73	16. Workshop Computer-Bildanalyse in der Landwirtschaft 04. Mai 2010 Braunschweig	2010
Heft 74	Erschließung von Nachhaltigkeitspotenzialen durch Nutzung innovativer Sensortechnologien <i>-Prozesskette Getreide-</i>	2010
Heft 75	Erschließung von Nachhaltigkeitspotenzialen durch Nutzung innovativer Sensortechnologien <i>-Prozesskette pflanzliche Frischeprodukte-</i>	2010
Heft 76	International Workshop The future of the quarter individual milking 14. – 15. September 2010 Potsdam	2010
Heft 77	A flow cytometric approach to monitor the effects of gentle preservation techniques in the postharvest chain	2011
Heft 78	17. und 18. Workshop Computer-Bildanalyse in der Landwirt- schaft 05. Mai 2011 Stuttgart und 09. Mai 2012 Osnabrück	2012

Heft 79	2. Öffentliches Symposium des „BCN“ BiogasPOTENZIALE Erkennen, Erforschen, Erwirtschaften	2012
Heft 80	Mechanisms of Bacillus spore germination and inactivation during high pressure processing	2013
Heft 81	19. Workshop Computer-Bildanalyse in der Landwirtschaft 2. Workshop Unbemannte autonom fliegende Systeme in der Landwirtschaft 06. – 07. Mai 2013 Berlin	2013
Heft 82	3rd Global Workshop on Proximal Soil Sensing	2013
Heft 83	19. Arbeitswissenschaftliches Kolloquium des VDI-MEG Arbeitskreises Arbeitswissenschaften im Landbau 11. – 12. März 2014 Dresden	2014
Heft 84	Prozessmikrobiologie in landwirtschaftlichen Biogasanlagen Schlussbericht zum Forschungsverbund BIOGAS-BIOCOENOSIS	2014
Heft 85	Sensoren.Modelle.Erntetechnik Kolloquium zur Verabschiedung von Dr. Ehlert 27. Mai 2014, Potsdam-Bornim	2014
Heft 86	Phosphor für die Landwirtschaft – Strategien für eine endliche Ressource 11. Juni 2014, Potsdam-Bornim	2014
Heft 87	Biofilme in Biogasanlagen - Struktur, Einfluss auf die Bio- gasausbeute und Optimierung technischer Systeme zur Rück- haltung der mikrobiellen Biomasse BIOGAS-BIOFILM	2015
Heft 88	20. und 21. Workshop Computer-Bildanalyse in der Landwirt- schaft 3. Workshop Unbemannte autonom fliegende Systeme (UAS) in der Landwirtschaft 26. Mai 2014, Osnabrück und 06. und 07. Mai 2015, Braun- schweig	2015
Heft 89	International Biochar Symposium: Biochar Contribution to Sus- tainable Agriculture 28 th – 29 th May 2015, Potsdam	2015
Heft 90	ISHS Symposium 2016 “Sensing Plant Water Status” Methods and Applications in Horticultural Science 05 th – 07 th October 2016 Potsdam	2016
Heft 91	10 Th International FRUTIC Symposium Quality and Safety of Fresh Horticultural Commodities February 07, 2017	2017
Heft 92	Etablierung eines <i>core</i> -Mikrobioms für Biogasanlagen Genom-Sequenzierung von Isolaten aus Biogasanlagen und Mapping von Metagenom-Datensätzen BIOGAS-CORE	2017

Heft 93	22. Workshop Computer-Bildanalyse und Unbemannte autonom fliegende Systeme in der Landwirtschaft 23. Workshop Computer-Bildanalyse in der Landwirtschaft 21. April 2016, Wernigerode und 27. April 2017, Potsdam-Marquardt	2017
Heft 94	Leitfaden für die Trocknung von Arznei- und Gewürzpflanzen	2017
Heft 95	Entwicklung von molekularen Markern und Nachweisverfahren auf Basis der quantitativen (realtime) PCR zum Monitoring von prozessrelevanten Mikroorganismen als Frühwarnsysteme für Prozessstörungen	2017
Heft 96	Cold atmospheric pressure plasma treatment of food matrices: Tailored modification of product properties along value-added chains of plant and animal related products	2017
Heft 97	INSECTA Conference 2017 07 th – 08 th September 2017, Berlin, Germany	2017
Heft 98	Storability of broccoli – investigations of optical monitoring, chlorophyll degradation and predetermination in the field	2018
Heft 99	24. Workshop Computerbildanalyse in der Landwirtschaft 25. April 2018, Zürich	2018
Heft 100	INSECTAS 2018 05 th – 07 th September 2018, Giessen, Germany	2018
Heft 101	6th International Conference on Machine Control and Guidance 1 st – 2 nd October 2018, Berlin, Germany	2018

If you are interested please contact:

Leibniz-Institut für Agrartechnik und Bioökonomie e.V.
Max-Eyth-Allee 100
14469 Potsdam
Germany

Tel.: +49 (0) 331 5699-820
Fax.: +49 (0) 331 5699-849
E-Mail: atb@atb-potsdam.de

Paper edition: 20,00 Euro

Internet (open access): <http://www.atb-potsdam.de/bab>